



Calhoun: The NPS Institutional Archive
DSpace Repository

Theses and Dissertations

1. Thesis and Dissertation Collection, all items

2007-06

A two-phase spherical electric machine for generating rotating uniform magnetic fields

Lawler, Clinton T.

Monterey, California. Naval Postgraduate School

<http://hdl.handle.net/10945/2995>

Downloaded from NPS Archive: Calhoun



Calhoun is the Naval Postgraduate School's public access digital repository for research materials and institutional publications created by the NPS community. Calhoun is named for Professor of Mathematics Guy K. Calhoun, NPS's first appointed -- and published -- scholarly author.

Dudley Knox Library / Naval Postgraduate School
411 Dyer Road / 1 University Circle
Monterey, California USA 93943

<http://www.nps.edu/library>

A Two-Phase Spherical Electric Machine for Generating Rotating Uniform Magnetic Fields

by

Clinton T. Lawler

B.S., United States Naval Academy (2001)

Submitted to the Department of Mechanical Engineering and the
Department of Electrical Engineering and Computer Science
in partial fulfillment of the requirements for the degrees of

Naval Engineer

and


Master of Science in Electrical Engineering and Computer Science

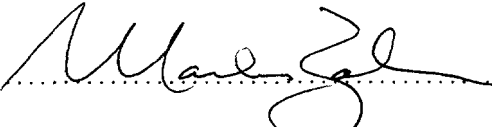
at the

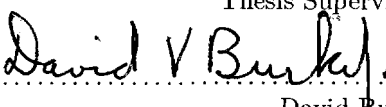
MASSACHUSETTS INSTITUTE OF TECHNOLOGY

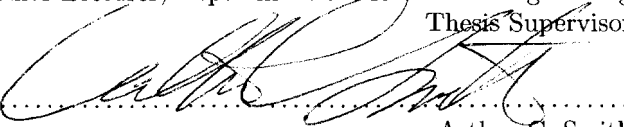
June 2007

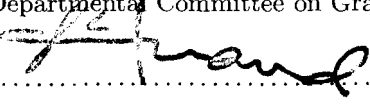
© Massachusetts Institute of Technology 2007. All rights reserved.

Author 
Department of Mechanical Engineering and
Department of Electrical Engineering and Computer Science
May 11, 2007

Certified by 
Markus Zahn
Thomas and Gerd Perkins Professor of Electrical Engineering
Thesis Supervisor

Certified by 
David Burke
Senior Lecturer, Department of Mechanical Engineering
Thesis Supervisor

Accepted by 
Arthur C. Smith
Professor of Electrical Engineering and Computer Science
Chairman, Departmental Committee on Graduate Students

Accepted by 
Lallit Anand
Professor of Mechanical Engineering
Chairman, Departmental Committee on Graduate Students

A Two-Phase Spherical Electric Machine for Generating Rotating Uniform Magnetic Fields

by

Clinton T. Lawler

Submitted to the Department of Mechanical Engineering and the
Department of Electrical Engineering and Computer Science
on May 11, 2007, in partial fulfillment of the
requirements for the degrees of
Naval Engineer
and
Master of Science in Electrical Engineering and Computer Science

Abstract

This thesis describes the design and construction of a novel two-phase spherical electric machine that generates rotating uniform magnetic fields, known as a fluxball machine. Alternative methods for producing uniform magnetic fields with air-cored solenoidal magnets are discussed and evaluated. Analytical and numerical models of these alternatives are described and compared. The design details of material selection, slot geometry, and mechanical connections are described for the fluxball machine.

The electrical properties of the machine are predicted and measured. Based on these properties, two modes of operation for the fluxball machine, normal and resonant, are described, and reference tables of important operating parameters are given. The drive and measurement circuitry for the fluxball machine are described.

The magnetic properties of the fluxball machine are measured using Hall effect sensors. The calibration of two different Hall effect sensors is performed, providing the ability to measure the magnetic fields accurately to $\pm 1\%$. Measurements of the magnetic field in the uniform field region are taken and compared with predicted values. The attenuation and distortion of the magnetic fields due to diffusion through the inner fluxball winding is measured as a function of operating frequency.

Finally, future uses of this machine for various applications are discussed. The fluxball machine provides uniform fields in the inner volume and point magnetic dipole fields in the exterior volume. Both regions are extremely useful for conducting controlled magnetic fields experiments. The fact that the machine can produce rotating fields of these types makes it particularly useful for applications in ferrofluid research and in experimental research related to large rotating machinery.

Thesis Supervisor: Markus Zahn

Title: Thomas and Gerd Perkins Professor of Electrical Engineering

Thesis Supervisor: David Burke

Title: Senior Lecturer, Department of Mechanical Engineering



My Other Thesis Supervisor

Acknowledgments

I would like to thank Professor Markus Zahn for all of the time, guidance, and encouragement that he has given me. His approach to teaching and research made working on this project a fun and educational experience. I hope that I have made a contribution to his on-going efforts to understand and to use ferrofluids.

I have truly enjoyed working with Dr. David Burke on this project and as his teaching assistant for Ship Structural Design. His intellectual curiosity always made working together easy and educational.

Ken Stone and Hayami Arakawa, from the MIT Hobby Shop, spent countless hours teaching me nearly everything I know about machining. Without their guidance and advice the fluxball machine would never have been built.

Wayne Ryan was always there to help me with whatever I was trying to do: order parts, bond plastic, wire sensors, etc. . . . His savvy saved me days of work, and it was always great to have someone to work with in the “early” hours of the day before the rest of MIT was awake.

In the sometimes extreme climate of Building N10, Zach Thomas and Uzoma Orji provided the necessary coffee, technical support, and friendship that was required to transform *this project* into *this document*.

I would like to thank the U.S. Navy for giving me three great years to work and learn at MIT. In particular, I am grateful to the Engineering Duty Officer community for the high value that they place on education.

Finally, my love and thanks goes to my family. My parents, my wife, and my children are the greatest blessing in my life.

Contents

1	Introduction	17
1.1	Motivation	17
1.2	Fluxball	18
1.3	Fluxball Machine	18
1.4	Measuring Magnetic Fields	21
1.5	Ferrofluid Background and Applications	22
1.6	Units	24
2	Uniform Magnetic Field	25
2.1	Overview	25
2.2	Calculating Magnetic Fields	26
2.3	Helmholtz Coils	28
2.4	Higher Order Coils	28
2.5	Fluxball	31
2.6	Conclusions	32
3	Machine Design	35
3.1	Overview	35
3.2	Test Chamber	37
3.3	Winding Design	38
3.4	Structural Design	41
3.5	Final Design	43

4	Machine Operation	45
4.1	Lumped Parameter Model of Windings	45
4.1.1	Resistance	46
4.1.2	Inductance	47
4.1.3	Capacitance	47
4.1.4	Complex Impedance	49
4.2	Additional Circuitry	50
4.3	Operation of the Fluxball Machine	53
4.3.1	Normal Operation	53
4.3.2	Operation at Resonance	55
5	Sensor Calibration	59
5.1	Sensors	59
5.1.1	Hall Effect	59
5.1.2	F.W. Bell Three Axis Probe and Teslameter	59
5.1.3	GMW Three Axis Sensor	61
5.2	Calibration Equipment	62
5.2.1	Reference Magnetic Field	62
5.2.2	LabVIEW Interface	64
5.2.3	Data Processing in Matlab	64
5.3	Procedure	66
5.4	Results	70
6	Magnetic Field Measurements	73
6.1	Predicted Magnetic Field	73
6.2	Measured Magnetic Field	73
6.3	Magnetic Field Uniformity	77
6.4	Magnetic Field Diffusion	83
6.5	Magnetic Field with a Sphere of Ferrofluid	83

<i>CONTENTS</i>	9
7 Conclusions	87
7.1 Fluxball Machine	87
7.1.1 Error	87
7.1.2 Mathematical Model	88
7.2 Future Ferrofluid Experiments	89
7.3 Future Machinery Experiments	90
A Fluxball — A Design History	95
A.1 John W. Clark's Fluxball	95
A.2 John A. Hipple Jr.'s Fluxball	97
A.3 William F. Brown and John H. Sweers' Fluxball	98
A.4 J.E. Everett and J.E. Osemeikhians' Fluxball	99
A.5 F. Primdahl and P Jensens' Fluxball	100
B Computer Design Tools	101
B.1 MATLAB [®]	101
B.1.1 Magnetic Fields Generated by a Loop of Current	101
B.1.2 Magnetic Fields by the Superposition of Current Loops	102
B.2 RHINOCEROS [®] 3.0 CAD/CAM	103
B.3 OMAX [®] Layout and Make	103
C Fluxball Construction	107
C.1 Fabrication of Parts	107
C.2 Assembly and Bonding	109
C.3 Winding the Coils	112
C.4 Electrical Connections	114
C.5 Final Configuration	114
D Specifications	117
D.1 Fluxball Materials	117
D.2 Series Resistor	119
D.3 National Instruments BNC 2120	123

D.4 AE Techron Inc LVC 5050 Amplifier	124
D.5 F.W. Bell Three Probe and 7030 Teslameter	126
D.6 GMW Three Axis Magnetic Field Sensor	128

List of Figures

1-1	Fluxball machine	19
1-2	Rotating magnetic field example	20
1-3	Methods for sensing and imaging magnetic fields	21
1-4	Hexagonal peaking patterns produced by ferrofluids that are exposed to perpendicular magnetic fields	22
1-5	Labyrinth instability produced by ferrofluids that are exposed to tangential magnetic fields	23
2-1	The righthand rule associated with the Biot-Savart Law	27
2-2	Direction and uniformity of magnetic fields produced by Helmholtz coil of different ratios of coil radius and coil separation	29
2-3	Direction and uniformity of magnetic fields produced by three and four coil axially symmetric magnets	30
2-4	Mathematical description of a fluxball	31
2-5	Magnetic field lines produced by a fluxball	33
3-1	Test chamber sizing for the inner fluxball	38
3-2	Prototype of winding design.	40
3-3	Design for fluxball winding support structure	42
3-4	Final design for the fluxball machine	44
4-1	The lumped parameter model of the fluxball.	46
4-2	Complex impedance of the fluxball windings	48

4-3	A screen shot of the user interface of the LabVIEW program that was used to excite, control, and measure the fluxball machine during operation	51
4-4	An annotated screen shot of the back panel of the LabVIEW program that was used to excite, control, and measure the fluxball machine during operation	52
4-5	The model of one winding of the fluxball machine being operated with a $1\ \Omega$ resistor, for measuring the current, and a capacitor, for generating resonance in the circuit	55
4-6	Real and imaginary components of the impedance of the fluxball windings .	56
5-1	A description of the Hall effect	60
5-2	F.W. Bell three axis probe and 7030 Teslameter System	61
5-3	GMW three axis sensor	62
5-4	The geometry and magnetic field lines for the inner fluxball as set-up for calibration procedures	63
5-5	Raw voltage waveform data prior to processing in Matlab	65
5-6	Probe and sensor alignment apparatus with GMW sensor removed. The circular tip of the F.W. Bell probe can be seen; it is flush with the bottom of the milled slot for the GMW sensor.	67
5-7	Probe and sensor alignment apparatus with GMW sensor installed.	67
5-8	Calibration set-up for x and y axis Hall effect elements	68
5-9	A close-up view of the calibration set-up for x and y axis Hall effect elements	68
5-10	Calibration set-up for z axis Hall effect element	69
5-11	A close-up view of the calibration set-up for z axis Hall effect element . . .	69
5-12	Initial and calibrated error for each element of the F.W. Bell three axis Hall effect probe and Teslameter system	71
5-13	Initial and calibrated error for each element of the GMW three axis Hall effect sensor	72
6-1	The predicted magnetic fields lines and percent of non-uniformity of the magnetic field produced by the fluxball machine as built	74
6-2	Sensor locations inside the fluxball machine for magnetic field measurements	75

LIST OF FIGURES

13

6-3	Side view of the sensor platform apparatus	76
6-4	Top view of the sensor platform shimmed to the top of the inner fluxball structure	76
6-5	Magnetic field measurements with only the inner winding energized	78
6-6	Magnetic field measurements with only the outer winding energized	79
6-7	Magnetic field measurements with both windings energized	80
6-8	One period of the predicted and measured magnetic field strength at each sensor inside the test chamber of the fluxball machine	81
6-9	The distortion and attenuation of the x -directed magnetic field inside the test chamber produced by the outer winding at six different operating frequencies between 1–1000 Hz	84
7-1	Top view of the inner fluxball winding with the sphere of ferrofluid positioned at the center of the fluxball machine	90
7-2	Side view of the inner fluxball winding with the sphere of ferrofluid positioned at the center of the fluxball machine	91
7-3	Artist’s rendering of the next generation destroyer	92
7-4	Podded propulsors installed on the Queen Mary 2	92
A-1	Spherical magnet designed by John W. Clark in 1938 for producing uniform magnetic fields used for nuclear research	95
A-2	Fluxball of Clark’s design in operation at the the MIT Physics Department	96
A-3	Spherical winding drawing by John A. Hipple Jr. from his 1941 United States Patent for a <i>magnetic field generator</i>	97
A-4	1945 fluxball test coil for point magnetic field measurements, as constructed	98
A-5	1945 fluxball test coil for point magnetic field measurements, in cross section	98
A-6	1966 three axis fluxball arrangement used to build a proton magnetometer	99
A-7	1981 three axis fluxball arrangement for fluxgate magnetometer vector feedback	100
B-1	2-D RHINO rendering of an intermediate fluxball machine design	104
B-2	Example of the layout patterns done in RHINO for machining	105

C-1	MIT Hobby Shop's Omax 2626 Waterjet cutting machine	108
C-2	Two parts that were created for alignment and connection of the fluxball structures	108
C-3	Fixture that was made and used for alignment of the discs and flanges . . .	109
C-4	Alignment fixtures stacked with discs and flanges	110
C-5	Inner fluxball structure after both bonding procedures were completed . . .	111
C-6	Fluxball structures just prior to winding of coils	111
C-7	Fluxball structure on the lathe as positioned for winding the coil around the structure	113
C-8	Close-up view of the fluxball structure on the lathe as positioned for winding the coil around the structure	113
C-9	Electrical connections on the support structure of the fluxball machine . . .	114
C-10	Interior view of the four winding hemispheres	115
C-11	Exploded front view of the fluxball machine	115
C-12	Fluxball machine with the outer winding canted outwards	116

List of Tables

3.1	Skin depth for copper	36
3.2	Magnetic, geometric, and electrical specifications for the fluxball machine	43
4.1	Predicted and measured values of resistance, inductance, and capacitance for each fluxball winding	46
4.2	Impedance magnitude and phase calculated at particular operating frequencies for both the inner and outer fluxball windings	49
4.3	Measured values of the $1\ \Omega$ current measurement resistors	51
4.4	The operating voltages required for each winding to produce a magnetic field density of 1 mT in the interior region of the fluxball machine	54
4.5	Capacitor values required for operation of fluxball machine in resonant mode	58
6.1	Predicted and measured values of x -directed magnetic field density at each of the sensor locations	82
6.2	Predicted and measured values of z -directed magnetic field density at each of the sensor locations	82
6.3	Predicted and measured values of inductance for each fluxball winding with a 4 cm radius sphere of MSG W11 ferrofluid at the center of the fluxball machine	85
7.1	Parameters for the mathematical model of the fluxball machine	89

Chapter 1

Introduction

1.1 Motivation

The research for this master's thesis was motivated by the desire to gain a deeper understanding of two particular subject areas: rotating electric machinery and ferrofluids. Each of these subjects straddle the gap between mechanical and electrical engineering, presenting bountiful opportunities to learn, problem solve, and build.

Rotating magnetic fields are used to turn everything from screwdrivers and coffee grinders to locomotive engines and ship propellers. These machines function on principles that are well understood and well documented. However, the design and construction of these machines is a constantly evolving field. Engineers and scientists are continually seeking ways to increase the power density, efficiency, and utility of these machines. While this thesis does not discuss the design of industrial motors or generators, it does probe the basic physics and engineering of these machines. In fact, the machine that has been designed and built as part of this thesis was conceived in order to correct the deficiencies of and to replace the conventional motor armatures that have been used to excite ferrofluids in early experiments.

Ferrofluids are stable colloidal suspensions of permanently magnetized nanoparticles in liquid volumes. These unique fluids exhibit superparamagnetic susceptibilities and offer new and interesting ways to interact with fluids. The governing equations for these fluids are being actively debated in the academic literature, allowing for interesting research at the first

principles level. Ferrofluids have found applications in consumer products, like cooling for loudspeakers and rotary exclusion seals for computer disk drives, in advanced technologies, such as nano-electromechanical systems and sensors, as well as in biomedical applications, such as directed drug delivery, therapeutic hyperthermia, and enhanced magnetic resonant imaging. New applications are currently being conceived and implemented in a wide variety of industries.

1.2 Fluxball

The term *fluxball* is used throughout this thesis to describe any combination of spherical windings. This type of current system has been described and analyzed in various forms dating back to 1883 [1, 2]. The name has been applied broadly to any device created by winding a coil around a sphere. The simplicity of this arrangement has led to a variety of applications in the fields of magnetic sensing and uniform magnetic field generation [3–7]. Depending on the application, fluxballs have been designed and built with single or multiple windings and in sizes ranging from a few inches to a few feet in diameter. These fluxballs have been capable of generating magnetic fields of intensities between a few nano-Tesla (nT) and a few milli-Tesla (mT). Appendix A describes some of the past implementations of fluxballs.

Theoretically the fluxball provides a perfectly uniform magnetic field in the interior volume of the winding. The design of a fluxball was considered for this thesis because a machine was needed that could produce a volume with easily controlled uniform magnetic fields. There were numerous other coil arrangements that could have been used to produce uniform magnetic fields. A number of alternative arrangements are described in Chapter 2.

1.3 Fluxball Machine

The term *fluxball machine* refers specifically to the machine, shown in Fig. 1-1, built during this thesis work. To the best of the author’s knowledge, this fluxball machine is one of the largest and most powerful designs yet attempted. This fluxball machine features two concentric, orthogonally oriented windings, each capable of producing a highly uniform

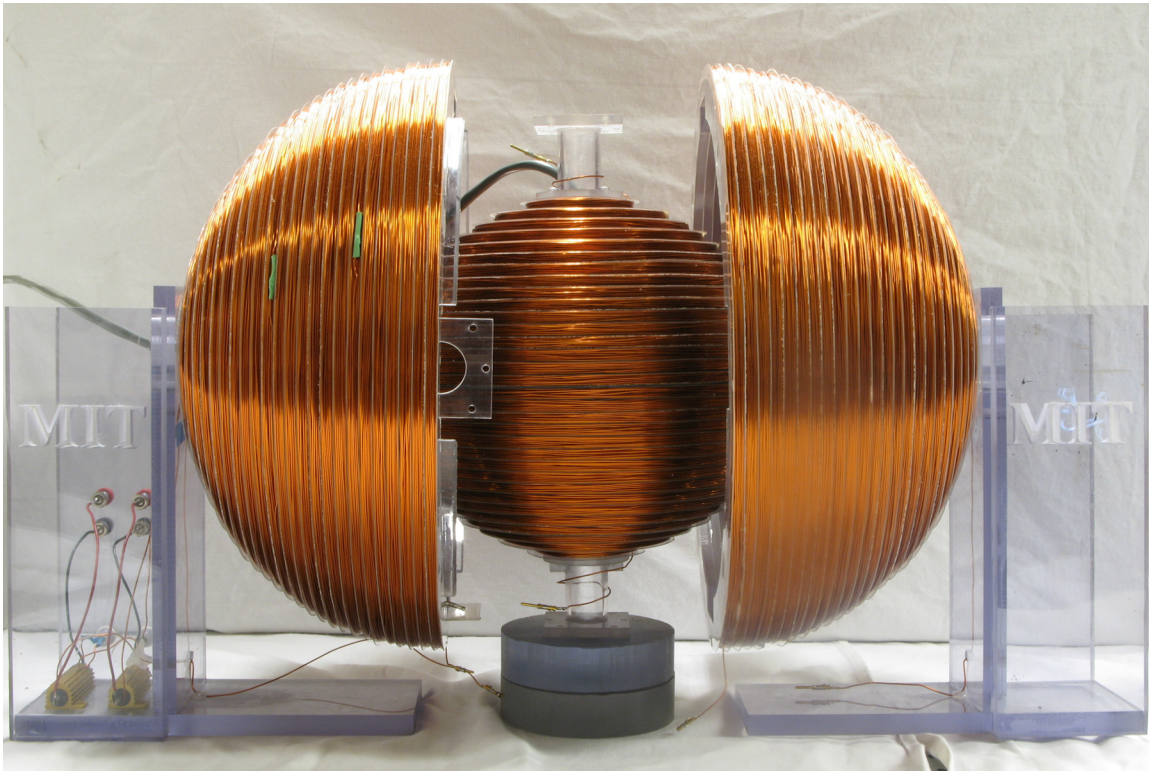


Figure 1-1: The fluxball machine. This two concentric winding spherical electric machine was built during the course of this thesis work in order to produce a 15cm diameter spherical volume of highly uniform rotating magnetic fields. The inner winding has a radius of 11 cm, while the outer winding has a radius of 16 cm.

magnetic field of 25 mT in the interior region of the inner sphere. When excited with alternating currents that are out of phase by 90° a rotating magnetic field is generated. Fig. 1-2 demonstrates this mechanism graphically.

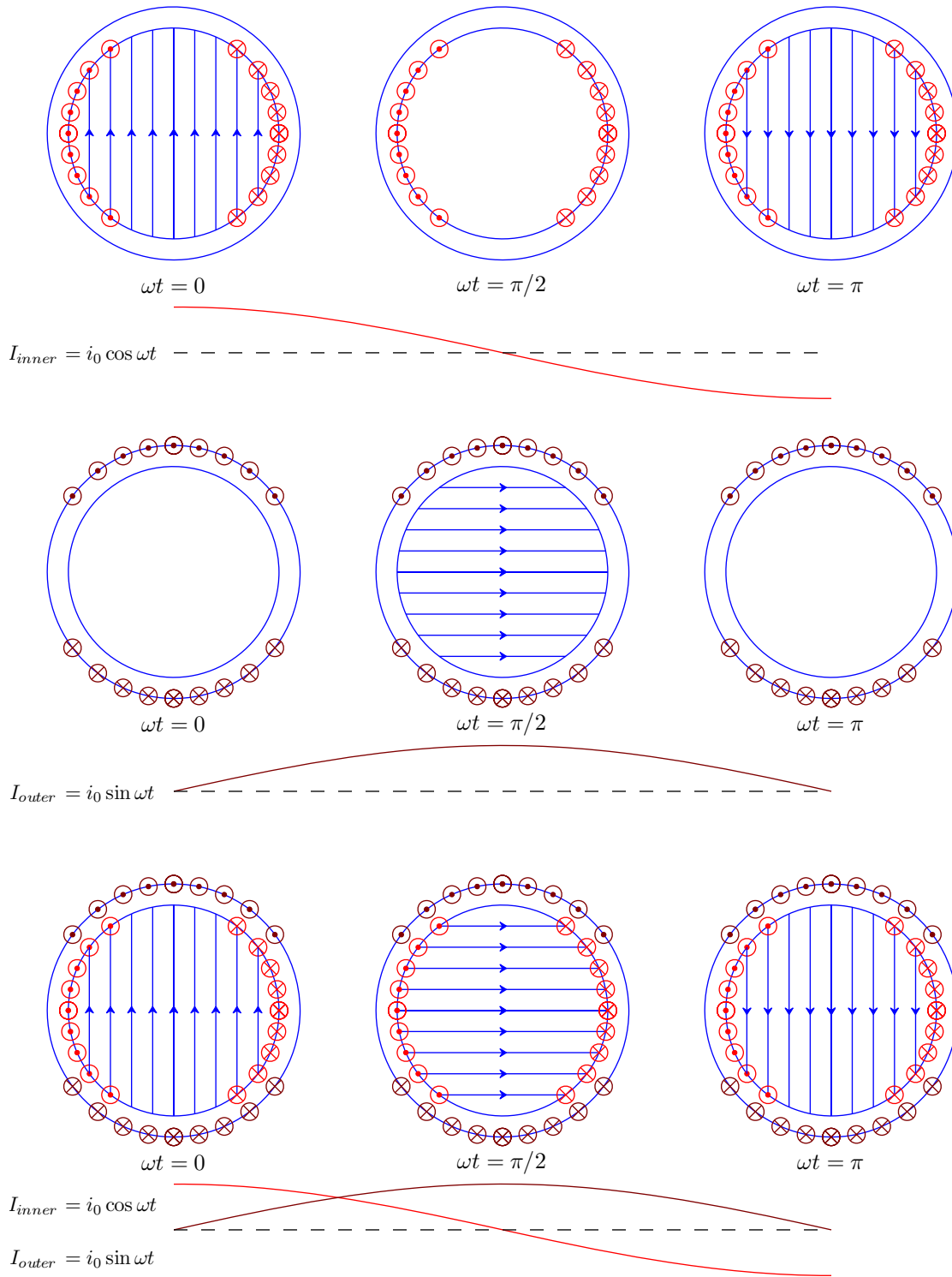


Figure 1-2: A rotating magnetic field is produced by driving two orthogonal coils with sinusoidal currents with 90° phase shifts. The top row of images shows the magnetic fields produced by the inner winding, while the second row shows the magnetic fields produced by the outer winding. The bottom row shows the *rotating* magnetic field produced by the combination of the inner and outer windings.

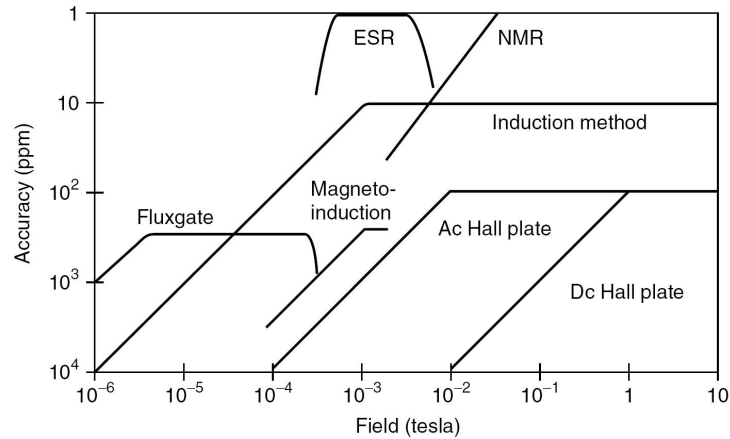


Figure 1-3: A graphical overview of magnetic field imaging methods. [8]

1.4 Measuring Magnetic Fields

Operation and validation of the fluxball machine required some research into the area of magnetic sensing. Depending on the particular magnetic sensing application, there are generally two or three different methods that can be used to measure the magnetic fields. Fig. 1-3 show some of these options and the applications for which they are suitable.

For this thesis, alternating current (AC) and direct current (DC) produced magnetic fields of strengths between 0 and 25 mT were measured. The sensors that could be used were nuclear magnetic resonant (NMR), induction method, or Hall effect sensors. Detailed descriptions of these methods, as well as many other methods, can be found in J. L. Symonds' article "Methods of Measuring Strong Magnetic Fields" [9]. NMR sensors, which use radio-frequency signals to measure the resonant frequency of specific protons in an applied magnetic field, are the most accurate, but they are prohibitively expensive. Induction coils, which measure the applied magnetic fields by linking a small amount of the flux with coils of wire, can have greater accuracy than Hall effect sensors, but these sensors are generally built to each particular application. Great care must be taken in the construction of induction sensors in order to realize their theoretical accuracy. Hall effect sensors are readily available, inexpensive, integrated circuit packages that can be carefully calibrated to give very good accuracy. For these reasons, Hall effect sensors were used to measure the magnetic fields generated by the fluxball machine.



Figure 1-4: The hexagonal peaking patterns produced by ferrofluids that are exposed to perpendicular magnetic fields, 33 mT in this case [11].

Two different Hall effect sensors were used to make measurements for this thesis. The first was a relatively expensive three axis probe and Teslameter combination manufactured by F.W. Bell, a Sypris Test and Measurement Company (\approx \$8,000). The second sensor is a relatively inexpensive (\approx \$35) three axis sensor containing three integrated circuit chips positioned with their axis of sensitivity mutually orthogonal. This sensor was purchased from GMW Associates and bore an Ametes logo on the chip package. Chapter 5 details the evaluation and calibration of each of these sensors.

1.5 Ferrofluid Background and Applications

The research and development of ferrofluids has been an active interdisciplinary field since their *discovery* more than thirty years ago. The primary starting point for understanding the behavior of ferrofluids is R.E. Rosensweig's text *Ferrohydrodynamics* [10]. Figs. 1-4 through 1-5 shows a few interesting ferrofluid patterns.

The academic literature and research concerning spin-up flows of ferrofluids lacks consensus on the issue of ferrofluid rotation. The disagreement focuses on the role of spin

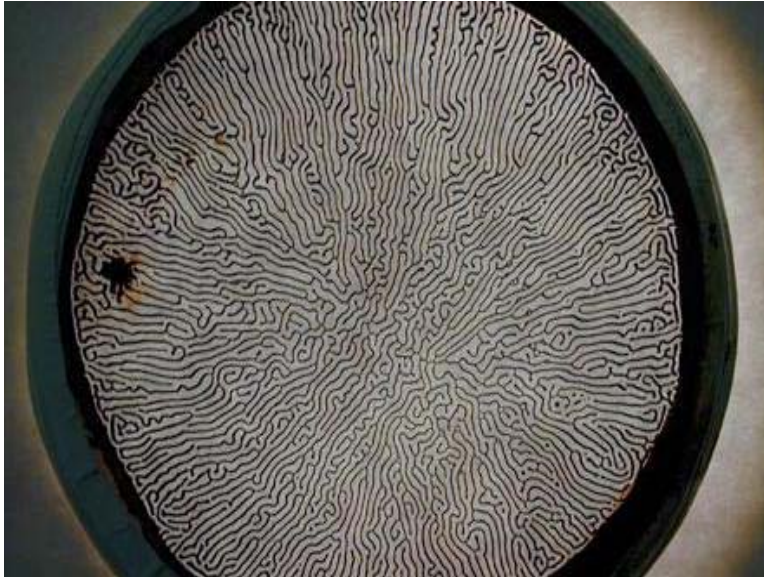


Figure 1-5: The labyrinth instability produced by ferrofluids that are exposed to tangential magnetic fields, 25 mT in this case. The fluid is constrained to a 1 mm layer by placing it between two 10 cm diameter glass plates [11].

diffusion in the rotation of ferrofluids that are exposed to uniform rotating magnetic fields. One side decouples the fluid mechanical and magnetic dynamics by taking the spin viscosity term to be negligibly small and then argues that non-uniformities in the magnetic field alone cause the rotation observed in ferrofluids. The other side points to fundamental properties of the ferrofluids, contesting that the linear and spin velocity terms in the magnetization relaxation equation account for the rotation, with velocity profiles determined by the large values of spin viscosity. Careful experiments have been conducted that seem to prove the latter theory correct [12,13]. In these experiments values for the magnetization relaxation time and spin viscosity were fit from measurements of ferrofluid velocity profiles using ultrasound velocimetry. These values showed good agreement with numerical simulations conducted using the finite element software COMSOL Multiphysics [14].

The definitive experiment for resolving this disagreement would involve driving a volume of ferrofluid with highly uniform magnetic fields and then measuring some quantity, either magnetic or fluid dynamic, that reflects motion, or lack of motion, of the fluid volume. The uniform magnetic field of the fluxball machine could be used to conduct this experiment,

leading to a better understanding of the mechanics of ferrofluids.

Ferrofluids are currently being applied in a variety of different industries. They are being used in loudspeakers and in electric power generation and transmission components because of their enhanced heat transfer capabilities. Also, a number of industries have begun using ferrofluids as liquid o-rings in rotary and exclusion seals. All of these applications take advantage of ferrofluid response to DC magnetic fields.

The applications of ferrofluids that are excited by AC and rotating magnetic fields are still being developed. Many applications are expected in the fields of micro and nano electrical mechanical systems (mems/nems). Other expected application are in the biomedical field where AC excited ferrofluids may be used for drug delivery, for biological material separation, and to improve magnetic resonance imaging [15,16].

1.6 Units

This thesis and the majority of the technical details are published in SI units. However, because many of the supplies were ordered in English units, the design work was done in a combination of English and SI units. In this thesis the English units are included, where helpful, in parenthesis.

Chapter 2

Uniform Magnetic Field

2.1 Overview

There are many different combinations of geometric arrangements and current distributions that can be used to produce *uniform* magnetic fields. Each of these arrangements has its own benefits and drawbacks. The typical trade-offs are between the degree of uniformity of the field, measured by deviation from the center of uniformity, the strength of the field, the volume of uniform field region, and the accessibility of the uniform field region.

Air-cored, axially symmetric electromagnets are the most common type of magnets used to generate uniform fields. When low density (< 10 mT) fields are required these magnets are usually cooled by circulating air or cooling water through the magnets. When much stronger fields are required, these magnets are cooled with cryogenes. For magnets requiring cooling systems the mechanical design must be done simultaneously with the electro-magnetic design. D.B. Montgomery's text *Solenoidal Magnet Design* gives insight into the design process for these larger electro-magnets [17].

Information on the design of square, polygon, saddle, and a variety of other geometries can be found in the academic literature [18–21]. The analysis of these coils is very similar to the approach described in Section 2.2, but the simplifications and calculations are done in cartesian geometry rather than cylindrical.

One final method for producing a uniform field is with permanent magnets. J.H. Jensen and M.G. Abele describe in “Generation of Highly Uniform Magnetic Fields with Magne-

tized Wedges” a method for producing a uniform field using wedges of permanent magnets [22]. Using a mechanical systems to rotate the system of wedges, a highly uniform rotating magnetic field could be produced. This type of apparatus was not considered for the design of this machine because it would limit the type and variety of experiments that could be performed (e.g. experiments involving an oscillating magnetic field).

The electromagnets discussed below are all air-cored, axially symmetric magnets that do not require dedicated cooling systems. The design of these systems is well document because of their broad applications in nuclear resonance experimentation, geomagnetic sensing, magnetic resonance imaging, etc. . . . The magnet designs described below were all considered for the design of the test apparatus built during this thesis. The coil distributions presented here are idealized. The practical design of a spherical coil system is described in Chapter 3 and is analyzed in Chapter 6.

2.2 Calculating Magnetic Fields

All of the magnetic fields that are calculated in this section depend completely on the winding geometry and current distribution. The Biot-Savart Law is the only mathematical tool required to solve for the magnetic field density, \mathbf{B} , at a distance, r , from a moving charge, q . The \mathbf{B} -field is given by:

$$\mathbf{B} = \frac{\mu_0 q \mathbf{v} \times \mathbf{i}_{QP}}{4\pi r^2} \quad \text{T}, \quad (2.1)$$

where μ_0 is the permeability of free space given in SI units. The signs of vectors \mathbf{B} , \mathbf{v} , and \mathbf{i}_{QP} are given using the right-hand rule as shown in Fig. 2-1.

For the particular case of axially symmetric coils it is often easiest to use coil loops as the basic unit of current and then calculate the total field by the superposition of each current loop, again using the Biot-Savart Law. The field, \mathbf{B} , at a point, P , given in cylindrical geometry by the coordinates (r, ϕ, z) , due to a circular loop of current that is centered at the origin with magnitude I and radius a , has field components B_r , B_ϕ , and B_z and is given

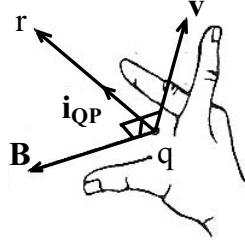


Figure 2-1: The magnetic field, \mathbf{B} , generated by a moving charge, q , at a point, r measured from q , is perpendicular to both the direction of motion, \mathbf{v} , and the unit vector joining the charge to the field point, \mathbf{i}_{QP} [23].

by eqs. 2.2 - 2.7 [24].

$$B_r = \frac{\mu I k z}{4\pi r(ar)^{1/2}} \left[-J_1 + \frac{a^2 + r^2 + z^2}{(a-r)^2 + z^2} J_2 \right] \quad (2.2)$$

$$B_\phi = 0 \quad (2.3)$$

$$B_z = \frac{\mu I k}{4\pi(ar)^{1/2}} \left[J_1 + \frac{a^2 - r^2 - z^2}{(a-r)^2 + z^2} J_2 \right] \quad (2.4)$$

$$\text{where } k = \left(\frac{4ar}{(a+r)^2 + z^2} \right)^{1/2}, \text{ and} \quad (2.5)$$

J_1 and J_2 are the elliptical integrals of Legendre given by [24]:

$$J_1 = K(k) = \int_0^{2\pi} \frac{d\phi}{(1 - k^2 \sin^2 \phi)^{1/2}} \quad (2.6)$$

$$J_2 = E(k) = \int_0^{2\pi} (1 - k^2 \sin^2 \phi)^{1/2} d\phi \quad (2.7)$$

Milan Garrett, in a series of articles, details how other useful properties of the coil system, such as the magnetic vector potential, mixed gradients, and mutual inductance between coaxial loops, can be calculated [25–27].

Finally, some useful pieces of the computer code, written to analyze these magnets, are included in Appendix B.

2.3 Helmholtz Coils

A common method used to produce a uniform magnetic field, is a two coil system known as a *Helmholtz* Coil. The Helmholtz coil consists of two windings of equal radius, a , placed a distance, d , apart and energized with a current, I . The magnetic field at a point z along the axis of the windings is given by eq. 2.8.

$$B_z(r = 0) = \frac{\mu_0 I a^2}{2} \left(\frac{1}{(z^2 + a^2)^{3/2}} + \frac{1}{((z - d)^2 + a^2)^{3/2}} \right) \quad (2.8)$$

When $a/d = 1$ the first two spatial derivatives of B_z , $\partial B_z/\partial z$ and $\partial^2 B_z/\partial z^2$, equal zero at $r = z = 0$ and produce a volume of nearly uniform \mathbf{B} near the center of the coils. Plots of the magnetic field lines and uniform volumes produced by four Helmholtz coils with different ratios of a/d can be seen in Fig. 2-2. Although properly spaced Helmholtz coils do produce a nearly uniform field, the volume of the uniform region is limited and the number of turns necessary to produce a field of the strength required for this machine make it an impractical option.

2.4 Higher Order Coils

In the same manner that properly spacing two coils can eliminate second order gradients in the magnetic fields, higher order gradients can be eliminated by the use of a larger set of compensating coils. The literature is full of different combinations of geometry and current distribution that can be used to create uniform magnetic fields compensated to almost any order desired [28–34]. Fig. 2-3 shows four coil systems that can be found in the literature. These coils systems have been sized to produce a spherical region, 15 cm in diameter, of 25 mT uniform magnetic field with non-uniformity less than 0.1%. The turns per coil and power consumption of the coil systems are listed in the figure. The dissipated power is calculated by assuming that American Wire Gauge (AWG) 20 wire with a current rating of 5 A is used to wind each coil.

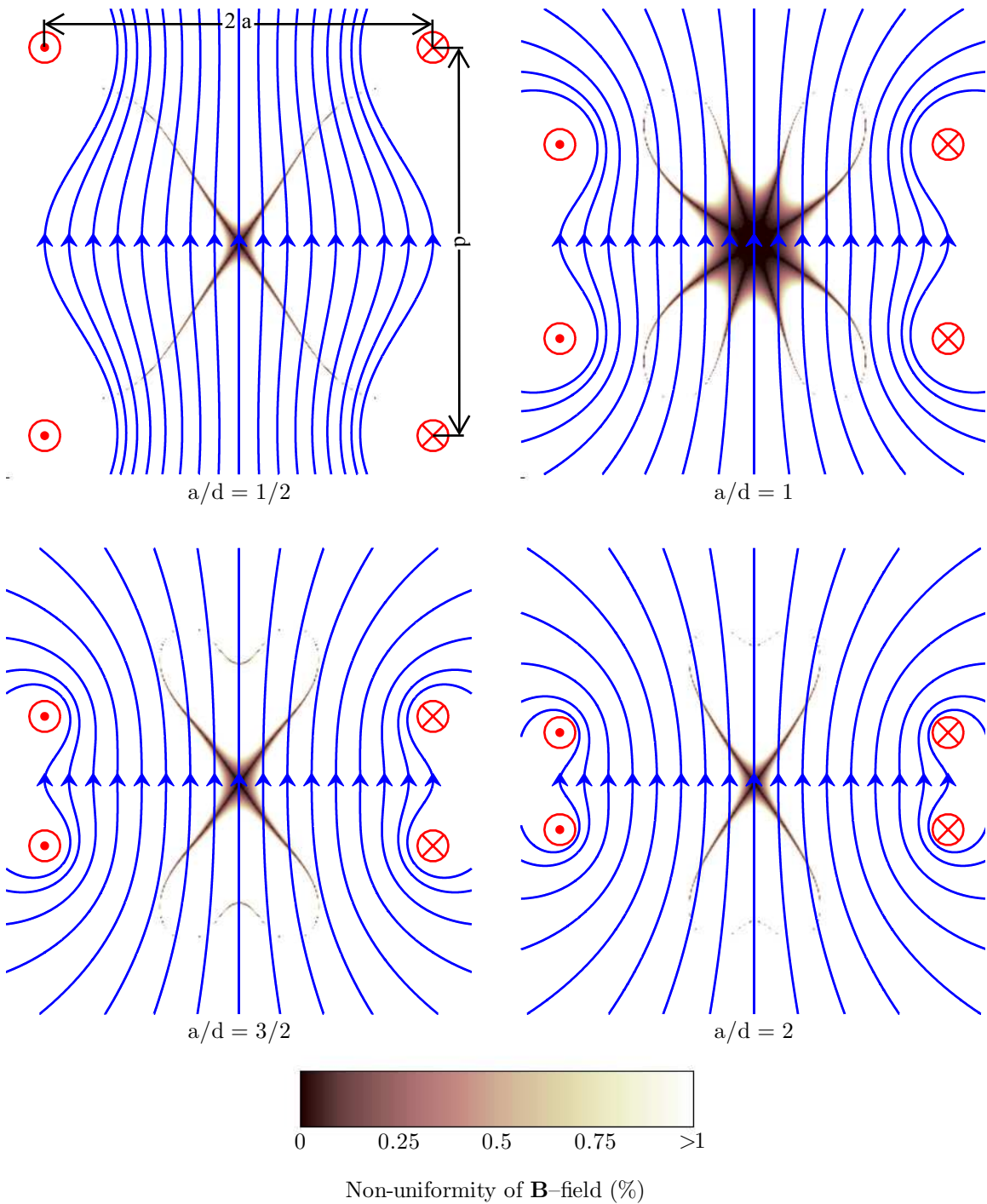


Figure 2-2: The magnetic field lines produced by Helmholtz coils of different ratios of coil radius, a , and coil separation, d . The shading on the plots shows the regions in which the magnitude of the magnetic field is uniform to within 1%.

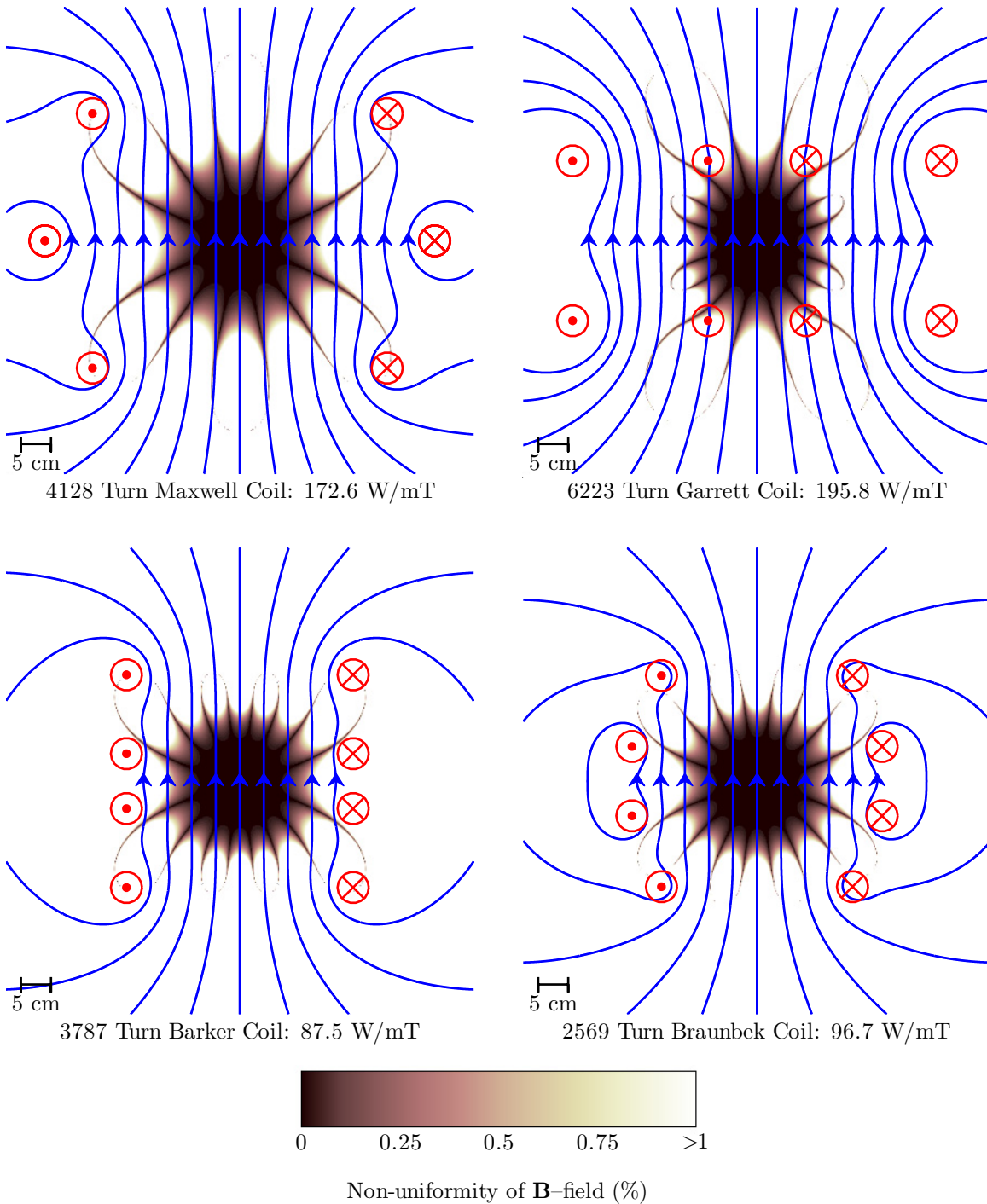
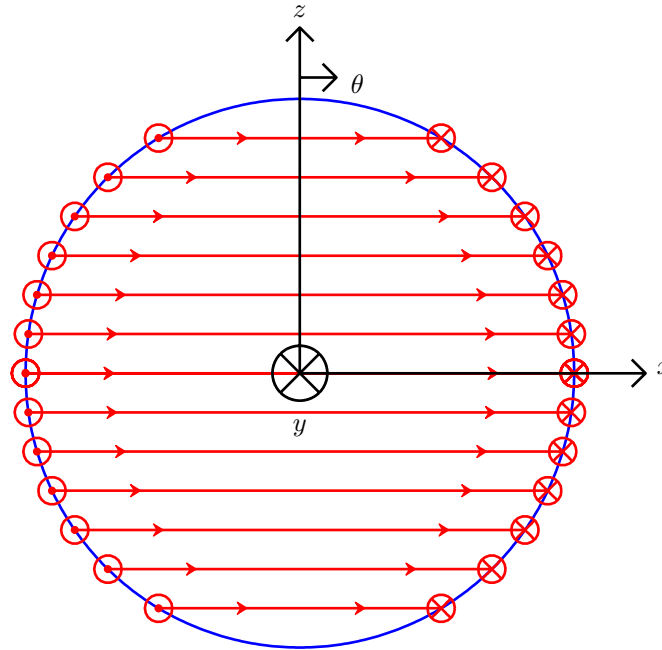


Figure 2-3: The magnetic field lines produced by three and four coil axially symmetric magnets. Each magnet produces a 15 cm diameter spherical 25 mT uniform magnetic field region with non-uniformity less than 0.1%. The total number of turns for the coil system and the power consumed per mT of field density produced are listed along with the name for each coil system. The shading on the plots shows the regions in which the magnitude of the magnetic field is uniform to within 1% [35].



$$\text{Surface Current: } \mathbf{K} = \mathbf{i}_\phi \frac{N}{2R} i \sin \theta$$

Figure 2-4: Mathematical description of a fluxball of radius R with a uniformly distributed winding in z with N total turns each carrying a current i as a sheet of surface current flowing azimuthally, in the ϕ direction, and varying sinusoidally with the zenith angle, θ .

2.5 Fluxball

A perfectly uniform field can be produced by using a sinusoidal winding distribution. The first description of this type of coil was presented by Éleuthère Mascart and J. Joubert in their 1883 text, *A Treatise on Electricity and Magnetism* [1]. In their description, the spherical coil was generated by the superposition of small, solenoidal currents of varying radius. In subsequent models, the *fluxball* has been described mathematically as a current sheet imposed on the surface of a sphere, as shown in Figure 2-4 [2]. For all of these models, the scalar magnetic potential can be used to solve analytically for the magnetic field in the regions inside and outside of the sphere. The field in the inner region is uniform and the field in the region outside of the fluxball is that of a point magnetic dipole. The magnetic

fields are given by eqs. 2.9 and 2.10.

$$\mathbf{B} = \frac{\mu_0 N i}{3R} (\mathbf{i}_r \cos \theta - \mathbf{i}_\theta \sin \theta) = \frac{\mu_0 N i}{3R} \mathbf{i}_z \quad r < R \quad (2.9)$$

$$\mathbf{B} = \frac{\mu_0 N i}{6R} (R/r)^3 (\mathbf{i}_r 2 \cos \theta + \mathbf{i}_\theta \sin \theta) \quad r > R \quad (2.10)$$

Again an approximate design of the machine was done, this time using the fluxball geometry. The magnetic field lines and basic design information for this geometry are shown in Fig. 2-5. Theoretically, the magnetic field is perfectly uniform inside the entire volume of the spherical coil. However, to allow for the perturbation due to discretization of the coil, even in this ideal case, the spherical coil in Fig. 2-5 has a radius of 8 cm in order to produce a 15 cm diameter uniform region.

2.6 Conclusions

The fluxball is clearly a more effective magnet for producing a uniform magnetic field than any of the previous coils examined. The total number of coils required, the power consumption, and the required radius of the winding are significantly lower than the other magnets considered. The disadvantages of the spherical magnet are the complexity of construction and the limited access that is available to the uniform field region.

There is another family of coil systems that can be found in the academic literature that bridge the gap between the three and four coils systems discussed in Section 2.4 and the fluxball [24, 35–40]. These systems are *optimal* coil systems that have been designed for various applications and usually use larger numbers of compensating coils. For this application the selection of the appropriate optimal solution would have provided a design that was slightly less uniform and possibly consumed slightly less power. Based on the overall size of this machine, power consumption was not a major concern, therefore, optimal coils systems were not considered.

One final advantage of the fluxball, particularly for the theoretical research with ferrofluids, is the mathematical model itself. This model is relatively easy to work with in spherical or cylindrical coordinates and allows for the analytical solution of many problems

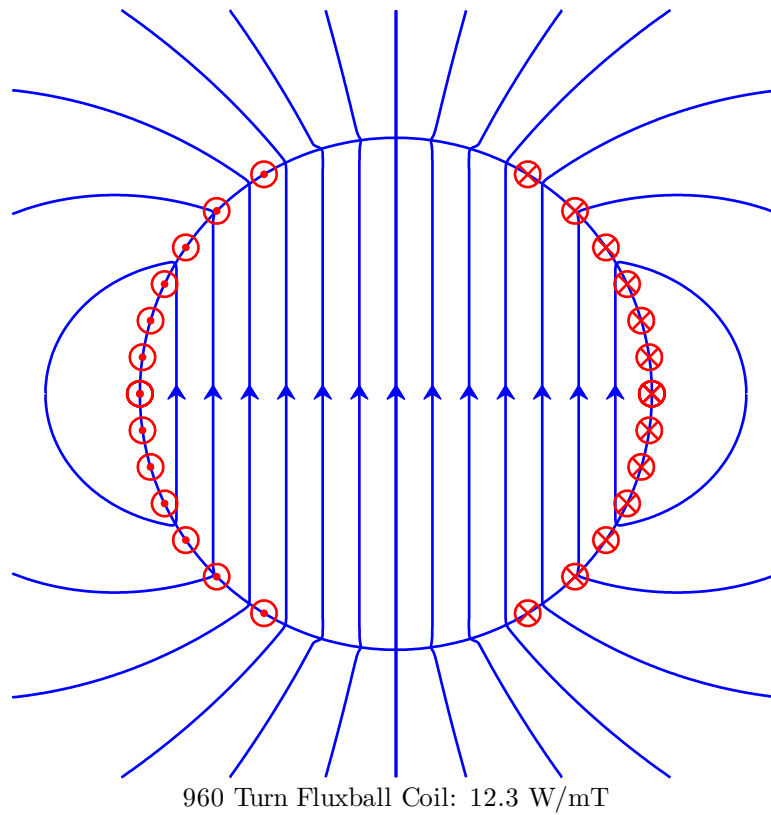


Figure 2-5: The magnetic field lines produced by a fluxball. The fluxball produces a 8 cm diameter spherical 25 mT magnetic field region with theoretically perfect uniformity. The total number of turns and the power consumed per mT of field density produced are listed.

concerning the interactions between the fluids and fields. The coil systems of Section 2.4 require greater mathematical manipulation to account for the specific geometry of the coil. While analytical work of this type can be done, it lends itself more to numerical analysis.

Chapter 3

Machine Design

3.1 Overview

Although the theory behind the fluxball is relatively simple, and there exist numerous similar designs, the design of this particular machine was not simple. Two main design goals drove the complexity of the design. First, a design goal was to generate a magnetic field of 25 mT. This meant that multiple layers would need to be used to create the windings and that thermal affects would be much greater. Technical specifications have been written that specify the current carrying capacity of wire of standard sizes, however, these specification become much less accurate when the wire is bundled together into a coil. Therefore a prototype had to be built in order to test the winding design. The winding design is discussed in greater detail in Section 3.3.

The second goal was to generate a rotating magnetic field. This meant that at least two windings would need to be created and that their connections and interfaces would need to be carefully designed. Because the decision was made to use concentric fluxballs for each of the windings, the attenuation of the magnetic fields due to the diffusion of the magnetic fields through the copper wire also needed to be addressed. This attenuation was most easily characterized by the skin depth, δ , of the material, given by:

$$\delta = \sqrt{2/(\omega\mu\sigma)}, \quad (3.1)$$

Frequency (Hz)	δ (mm)
1	65.2
10	20.6
50	9.2
60	8.4
100	6.5
500	2.9
1000	2.1

Table 3.1: The skin depth of copper calculated with $\mu = \mu_0 = 4\pi \times 10^{-7}$ H/m and $\sigma = 5.8 \times 10^7$ S/m.

where ω is the angular frequency, μ is the magnetic permeability, and σ is the electrical conductivity [23]. Table 3.1 lists the skin depth of copper, with $\mu = \mu_0 = 4\pi \times 10^{-7}$ Henries/meter and $\sigma = 5.8 \times 10^7$ Siemens/meter, for frequencies between one and 1000 Hz.

The maximum thickness of the winding was ≈ 6 mm, meaning that at frequencies above 30 Hz the magnetic field might be attenuated by the inner winding by more than 15%. Furthermore, because the thickness was not uniform with respect to the incident magnetic field, the attenuation would be non-uniform. In order to better understand the effects of the winding on the magnetic fields, the mathematical model of the fluxball was used to analyze the diffusion of the fields through the conducting sphere. Additionally, after the machine was constructed the fields were measured at different excitation frequencies. The measured attenuation was significantly smaller than predicted by simple skin depth approximations. These measurements are discussed in Chapter 6.

Because of these complexities, a computer model was generated in Matlab and rendered in Rhinoceros 3.0 [41, 42]. These tools allowed for rapid model generation and validation in the early stages of the design. These tools proved very useful for developing the basic parameters of the design and for improving the construction of the fluxball. Appendix B describes the modeling tools in greater depth.

While the main specifications for the construction of the machine were known from the computer models before construction began, most of the details of assembly and interconnec-

tion, both mechanical and electrical, were designed as the machine was being constructed. Two facilities were used to build the fluxball machine — the MIT Hobby Shop and the Laboratory for Electromagnetic and Electronic Systems (LEES) shop. The knowledge and experience of the shop staffs were the key enablers to production of the fluxball machine. Detailed drawings, descriptions, and images of the constructions process are included in Appendix C.

3.2 Test Chamber

This machine was designed and built in order to have a test chamber with highly controllable, highly uniform magnetic fields. Therefore the size and shape of the test chamber was the first detail to be designed. The test chamber needed to be able to contain a sphere of ferrofluid that was large enough to be studied with the ultrasound velocimetry sensors that are operated by the laboratory. These sensors have a diameter of 8.5 mm. Therefore the test sphere should be approximately ten times larger, having a diameter in excess of ≈ 80 mm. Allowing for cable runs and for other devices, such as a torque transducer, that may be desirable in the future, the inner chamber diameter was designed to be 15 cm in diameter. Fig. 3-1 shows the initial concept drawing for the inner fluxball.

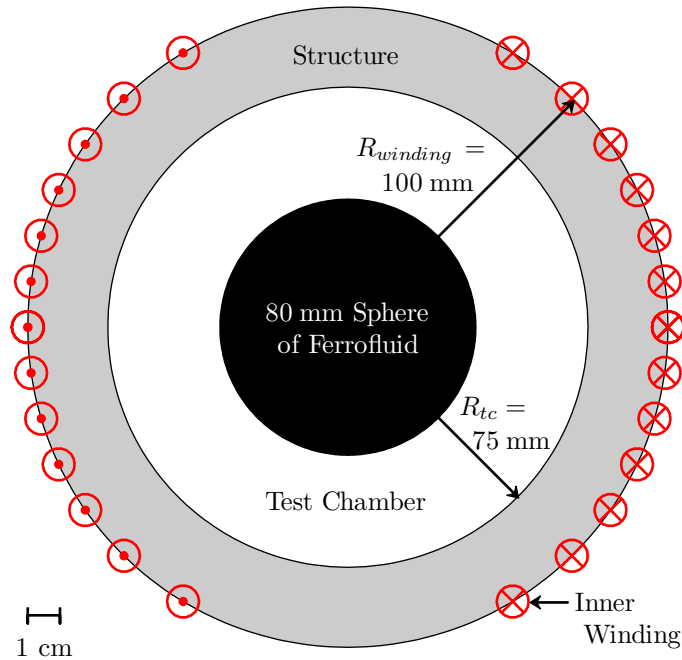


Figure 3-1: Test chamber sizing for the inner fluxball. The ferrofluid test sphere needed to be at least 80 mm in diameter to allow for ultrasound velocimetry equipment. Allowing for additional sensors and equipment inside the chamber, the test chamber needed to have a radius, R_{tc} , of approximately 75 mm. Then leaving room for support structure, the initial inner winding radius, $R_{winding}$, was sized at 100 mm.

3.3 Winding Design

In order to generate a uniform field in the interior region of the sphere, the number of turns per length along the axis of the winding needed to be uniform and the radius of the winding needed to vary with the sin of the zenith angle, θ . This exact coil geometry was not practically achievable for a fluxball with a large magnetic field. In this situation the winding must be created by laying down multiple layers of wire at each height along the axis of the winding. Therefore some wires would lay directly on the surface of the sphere, but other wires would lay above the surface of the sphere by a few millimeters. Also laying down the wires in such a way that the turns density remained constant while the radius changed quickly would be very difficult to have done in practice. Finally, the operation of

the spheres required that there be a mechanism for accessing the inner chamber in order to change the ferrofluid test sphere or to route instrumentation. In order to solve these problems, a number of different geometries were explored and the effect on the magnetic fields were numerically predicted using the Biot-Savart Law.

Due to the necessity of laying down multiple layers of wire at each location along the axis of the winding, the winding was bundled into slots so that the turns could lay with the proper density along the axis of the winding. Additionally, a flange was required to separate these slots so that turns could not slide from one slot to the next. These two features were purely for construction reasons, and therefore it was desirable to reduce their impact on magnetic field properties. The impact was reduced by using small slots and very thin flanges.

In order to minimize the effect of skin depth, as well as to increase the turns density, the smallest diameter wire that was capable of carrying the required current was used. The required current was 5 A for a short interval (≈ 1 min) and 2 A for continuous operations. From wire property tables, including some deduction for bundling, it was hypothesized that AWG 20 wire, with a diameter of 0.81 mm, would be smallest wire capable of carrying these currents. The data sheet for this wire can be found in Appendix D. A prototype of two winding slots was built in order to verify the capability of the bundled wire. Fig. 3-2 shows the winding prototype.

The strength of the magnetic field in the interior of a spherical winding is given by eq. 3.2:

$$B_z = \frac{\mu_0 N i}{3R} \text{ T}, \quad (3.2)$$

where $\mu_0 = 4\pi \times 10^{-7}$ H/m is the permeability of free space, N is the total number of turns on the sphere, i is the current in the winding, and R is the radius of the sphere taken at the midpoint of the winding bundle. Based on the design of the test chamber and on estimates for the required support structure, R was taken to be 10 cm for the inner winding and 15 cm for the outer winding. The 20 AWG wire size had been selected, and its current carrying capacity verified with the prototype. This left only the number of turns to be calculated for the desired field strength of 25 mT. The number of turns was a function of the slot

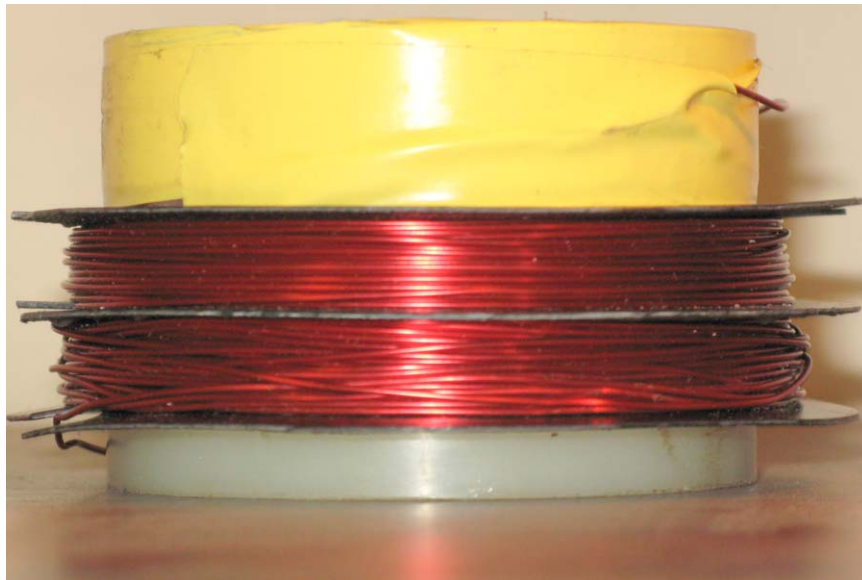


Figure 3-2: A prototype of the fluxball winding that was built to verify the current carrying capacity of the 20 AWG wire bundle. Two 1 cm high bundles of 56 turns were wrapped in series on a 7.5 cm diameter white delrin cylinder and separated by a 0.8 mm black plastic flange. The first turn was secured to the cylinder by the turns that were wrapped on top of it, while the final turn had to be secured with the yellow electrical tape shown at the top of the picture. This made the terminals of the coil available, while not allowing the coil to unwind.

geometry and the numbers of layers per bundles, as given by eqs. 3.3–3.5.

$$N = \text{slots} * \text{turns/slot} \quad (3.3)$$

$$\text{slots} = \frac{2R}{\text{slot height} - \text{flange height}} \quad (3.4)$$

$$\text{turns/slot} = \text{layers} * \frac{\text{slot height}}{\text{wire diameter}} \quad (3.5)$$

The slot and flange heights were selected from a catalog of standard material thicknesses, and then it was calculated that 6 layers of wire would need to be wrapped in each slot to produce the required magnetic field density. Each winding then had an Amp-turns density of 308 A-turns/cm along the winding axis.

3.4 Structural Design

Once the test chamber dimensions were roughly known and the winding distribution was designed, then the structure for supporting the winding could be designed. The ideal structure for this machine would be perfectly spherical, have very thin, strong flanges for keeping the winding distribution correct, and have very little radial thickness so that the winding radii could be located very close together. There were not any commercially available structures that met this description, so something had to be specially fabricated. Material selection, design for fabrication, and design for future growth all had to be considered.

The material selected for the fluxball was polycarbonate. This is a very strong plastic that is nonmagnetic, nonconducting, and relatively easy to machine. A wide variety of sheets, shapes, and parts can be purchased in polycarbonate. As with all plastic, certain liquid environments can be very destructive. For this device, ferrofluids made with oil or water will be encountered, as well as some alcohol products. Polycarbonate is relatively tolerant of these environments and is, therefore, a good choice for this application. Finally, polycarbonate has a melting point of $\approx 115^\circ \text{C}$ (240°F), which is below the expected operating temperature of the winding. All of these properties made polycarbonate an excellent choice for the fluxball structure.

A number of geometries were investigated for creating the spheres, but in the end discs

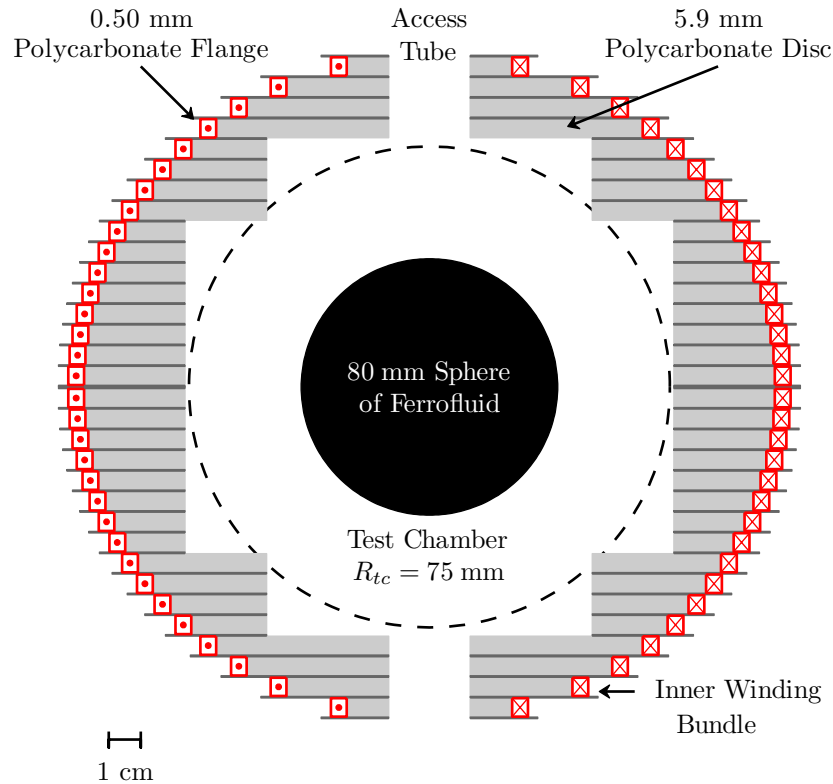


Figure 3-3: The design for fluxball winding support structures. Discs of different radii were stacked and bonded in place to support the winding and test chamber apparatus.

were chosen as the basic building blocks. Thick discs were used to create the slots, and thin discs were interleaved to serve as flanges. The inner radii of the spheres were cut in steps so that assembly and later installations could be managed more easily. Dealing with doubly curved surfaces can be quite challenging in terms of construction, so these were eliminated altogether. A computer controlled OMAX waterjet cutter was used to precisely cut the disc from large sheets of polycarbonate. Grooves were cut into all of the discs so that they could be precisely aligned. The discs were then aligned and bonded in place with an acrylic cement. The data sheets for the two thicknesses of polycarbonate sheet that were used to construct the structure can be found in Appendix D. Fig. 3-3 shows the design for the inner sphere. The outer sphere was built in precisely the same way.

Characteristic	Inner Fluxball	Outer Fluxball
Interior B -field	5.4 mT/A	5.4 mT/A
Winding Axis Radius, $r(\theta = 0^\circ)$	10.36 cm	15.04 cm
Quadrature Axis Radius, $r(\theta = 90^\circ)$	11.02 cm	16.75 cm
Peak Current	5 A	5 A
Continuous Current	2 A	2 A
Total Turns	1280	1920
Length of Winding	700 m	1568 m
Total Slots	32	48
Slot Height	5.9 mm	5.9 mm
Flange Height	0.50 mm	0.50 mm

Table 3.2: Magnetic, geometric, and electrical specifications for the fluxball machine.

3.5 Final Design

Fig. 3-4 shows how the two fluxball windings fit together to form a single machine. In order to assemble all of the pieces together into a single machine a number of connections needed to be designed and constructed. These details were generally designed and built in the shop with the advice of the shop staff. See Appendix C for more details and more pictures.

Table 3.2 lists the characteristics of the fluxball machine. There was a difference in radius between the winding axis and quadrature axis because the disc radii were calculated and cut based on ordered rather than measured material thicknesses. The small differences between ordered and actual values were multiplied by the number of slots and flanges, leading to final fluxball windings that were slightly oblate.

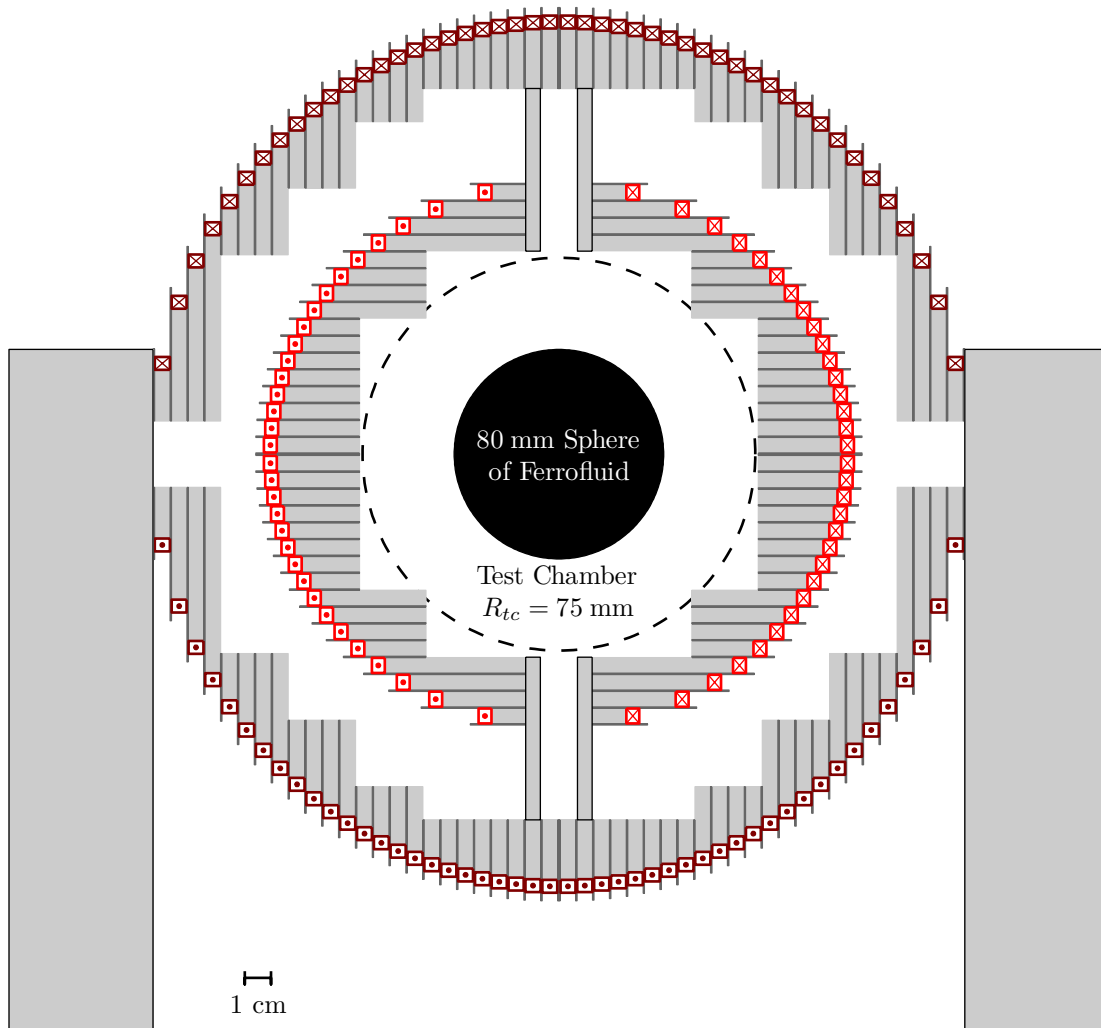


Figure 3-4: The design for the fluxball machine including support legs and inner fluxball support tubing.

Chapter 4

Machine Operation

4.1 Lumped Parameter Model of Windings

Lumped parameter models are used in order to build the intuition and understanding required for operating complicated machinery. By the winding design this machine has high inductance. Driving a highly inductive machine with alternating current requires detailed knowledge of the frequency response of the circuit because the impedance of the circuit changes significantly with excitation frequency. Operating parameters can then be tabulated that enable the machine to be quickly reconfigured during experimentation. This information is particularly important for this machine because it will be operated at a range of frequencies while conducting experiments with ferrofluids.

The lumped parameter model seeks to characterize the machine by its response to single frequency sinusoidal excitations across the frequency spectrum. The characterization is in terms of the circuit's inductance, capacitance, and resistance. These distinct circuit characteristics are in reality all properties of the single circuit component - a single, continuous, wire. The *telegrapher's equations* would be a valid way to model this circuit, however the periods of interest are long enough relative to the transit time of the signal down the wire that a single set of circuit elements can be used to model the wire. Therefore, each of the windings is characterized by the RLC circuit shown in Fig. 4-1.

The values for each of the components were predicted based on the wire properties and then the actual component values were measured using the Hewlett-Packard 4192A

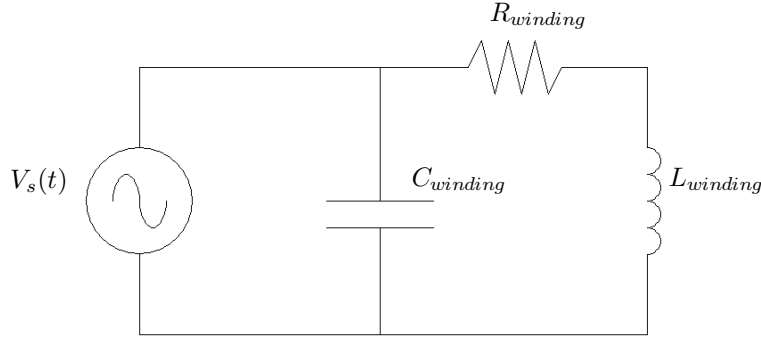


Figure 4-1: The lumped parameter model of the fluxball being driven by a time domain voltage signal, $V_s(t)$. Each fluxball winding is characterized by its capacitance, $C_{winding}$, inductance, $L_{winding}$, and resistance, $R_{winding}$.

Component	Predicted Value	Measured Value	%Error
R_{inner}	23.3 Ω	24.0 Ω	3.1
L_{inner}	153.8 mH	172.8 mH	11.0
C_{inner}	N/A	140 pF	N/A
R_{outer}	52.1 Ω	53.0 Ω	1.7
L_{outer}	517.5 mH	570.0 mH	9.2
C_{outer}	N/A	140 pF	N/A

Table 4.1: The predicted and measured values of resistance, inductance, and capacitance for each fluxball winding. Resistance values were measured at 5 Hz. Inductance and capacitance measurements were taken in the frequency mid-range ($\approx 100 - 5000$ Hz for inductances and $\approx 100 - 5000$ kHz for capacitances).

LF Impedance Analyzer. The complex impedance of each circuit was measured across the entire range of the impedance analyzer, 5 Hz to 13 mHz. The measured and predicted values for the circuit components are listed in Table 4.1

4.1.1 Resistance

The resistance of the windings were accurately predicted from properties of the wire. The resistance of a length of wire is given by eq. 4.1:

$$R = \frac{L_w \rho}{a} \quad \Omega \quad (4.1)$$

where L_w is the length of the wire in meters, ρ is the resistivity of the conductor in $\Omega\text{-m}$, and a is the cross sectional area of the conductor in m^2 . AWG 20 copper wire at 20°C has $\rho = 1.724 \times 10^{-8} \Omega\text{-m}$ and $a = \pi r_{\text{wire}}^2 = \pi(0.4064 \times 10^{-3})^2 = 0.5189 \times 10^{-6} \text{m}^2$.

4.1.2 Inductance

Hermann Haus and James Melcher, in their text *Electromagnetic Fields and Energy*, give an expression for the external inductance of a spherical winding based on the model of the fluxball as a ϕ directed current sheet [2]. Using eq. 4.2 and the fluxball properties given in Table 3.2 the external component of the self inductance of each winding was predicted.

$$L_{\text{external}} = \frac{2}{9} \pi N^2 \mu_0 R \quad \text{Henries} \quad (4.2)$$

The internal inductance of the coil accounts for the energy that is stored inside the winding. This inductance is only a function of the length of the wire, l_w , and the permeability of the wire, μ_0 [23]. The internal inductance of wire is given by eq. 4.3.

$$L_{\text{internal}} = \frac{\mu_0 l_w}{8\pi} \quad \text{Henries} \quad (4.3)$$

Despite the length of each fluxball winding, the internal inductance contribution is only a fraction of a percent of the total self-inductance.

The mutual inductance of the winding was predicted to be negligible due to the orthogonal orientation of the fluxball to one another. Measurements of the winding currents were taken that verified this prediction.

4.1.3 Capacitance

Capacitance between the wires in the winding occurs at high frequencies when the current in the wire does not have time to diffuse evenly into the wire; instead the charge resides on the perimeter of the wire. The charge on the outside of the wire and the small separation between the wires generates some capacitance. This effect was not of importance at the operating frequencies of this machine, so the values were measured experimentally and noted in Table 4.1 for completeness.

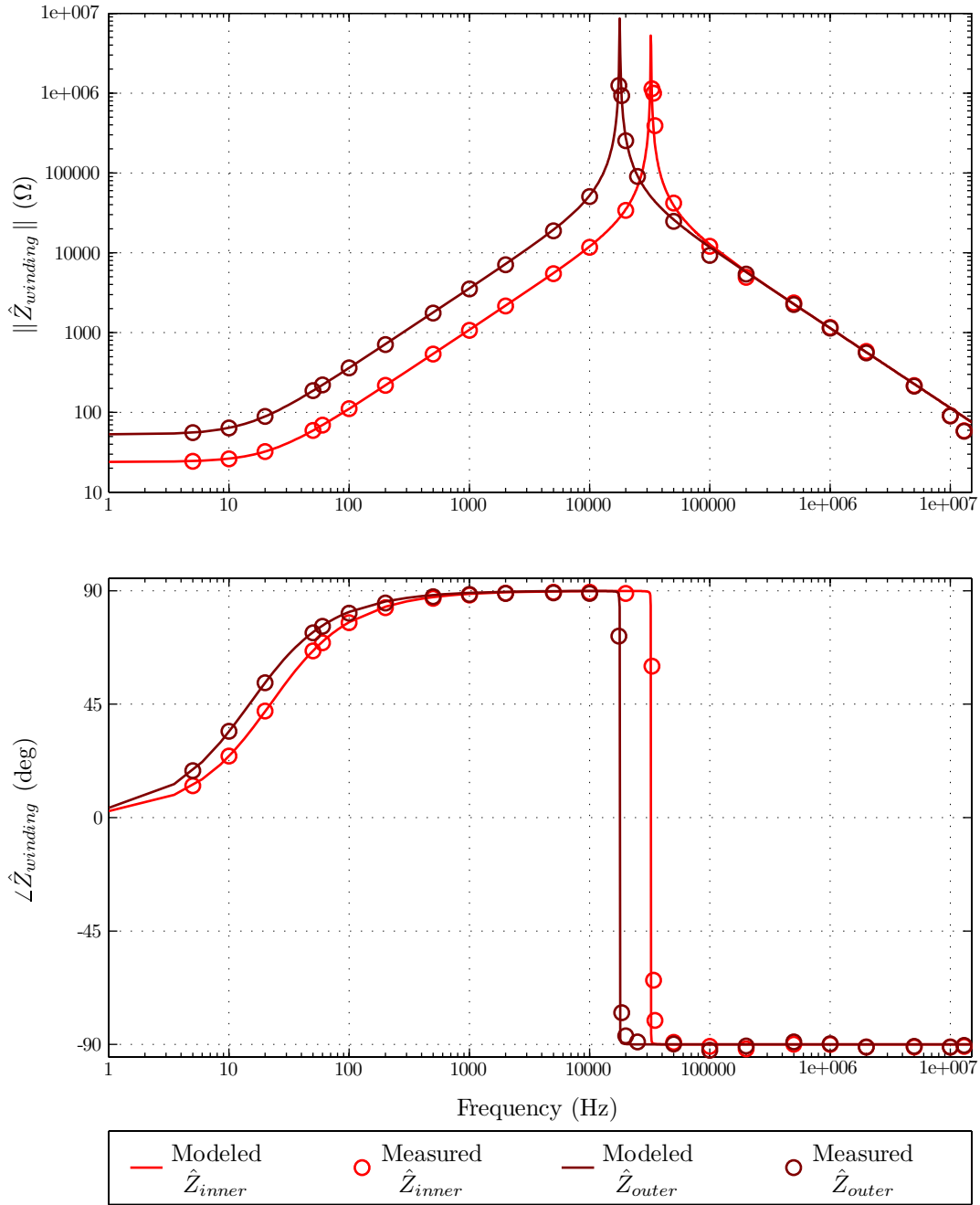


Figure 4-2: The complex impedance of the fluxball windings as a function of frequency. The impedance magnitude and phase were measured using a Hewlett-Packard 4192A LF Impedance Analyzer. The modeled values were calculated using the *measured* values given in Table 4.1 and the impedance model given by eq. 4.4 and shown in Fig. 4-1.

Frequency (Hz)	$\ \hat{Z}_{inner}\ $ (Ω)	$\angle\hat{Z}_{inner}$ (Deg)	$\ \hat{Z}_{outer}\ $ (Ω)	$\angle\hat{Z}_{outer}$ (Deg)
1	24.0	2.6	53.1	3.9
5	24.6	12.7	55.9	18.7
10	26.3	24.3	64.0	34.0
20	32.4	42.1	89.1	53.5
30	40.5	53.6	119.8	63.7
40	49.6	61.1	152.7	69.7
50	59.4	66.1	186.8	73.5
60	69.4	69.8	221.3	76.1
70	79.7	72.5	256.2	78.1
80	90.1	74.6	291.4	79.5
90	100.6	76.2	326.7	80.7
100	111.2	77.5	362.1	81.6
200	218.5	83.7	718.3	85.8
300	326.6	85.8	1076.0	87.2
400	435.0	86.8	1434.3	87.9
500	543.5	87.5	1792.9	88.3
1000	1087.0	88.7	3593.1	89.1

Table 4.2: Impedance magnitude and phase calculated at particular operating frequencies for both the inner and outer fluxball windings.

4.1.4 Complex Impedance

Once the values of all of the circuit components are known, then it is convenient to model the circuit by its complex impedance. Eq. 4.4 gives the expression for input impedance, \hat{Z} , of the circuit shown in Fig. 4-1 as a function of angular frequency, ω .

$$\hat{Z} = -\frac{\frac{j\omega}{C} + \frac{R}{LC}}{\omega^2 - \frac{j\omega R}{L} - \frac{1}{LC}} \quad \Omega \quad (4.4)$$

Fig. 4-2 graphically describes the circuit's measured and modeled complex impedance using the component values given in Table 4.1. Table 4.2 lists the values for the impedance of the windings at particular frequencies that may be used to operate the machine.

4.2 Additional Circuitry

The fluxball windings could be driven in a variety of a ways. The difficulty, as always, was how to drive them so that the important electrical and magnetic properties could be easily controlled and measured. A number of different options were tested before the final method described here was chosen. The following parts were used for evaluation, testing, and operation of the fluxball machine: a personal computer with LabVIEW installed, the National Instrument's accessory BNC 2120, one dual channel LVC 5050 power amplifier, two $1\ \Omega$, $50\ \text{W}$ resistors, a $5\ \text{V}$ DC power supply, magnetic sensors that will be described in Chapter 5, and numerous BNC cable connectors.

The LabVIEW PC interface provided a robust platform for performing numerous tasks from generating waveforms to measuring currents and voltages from magnetic sensors to writing and saving files of data. Using software generators, two drive signals were created and routed to analog output BNC connections on the BNC 2120. From here the signals were sent to the amplifier. Figs. 4-3 and 4-4 show the front and back panels from the LabVIEW user interface that was built to operate the fluxball machine.

LEES operates two AE Techron Inc. LVC 5050, high voltage, general purpose, linear power amplifiers. The data sheet for these amplifiers is included in Appendix D. For the most part a single amplifier was used in the 20 gain mode. Since the BNC 2120 was able to provide up to 10 volts and the amplifier began clipping and distorting the signal at $\approx 120\ \text{V}$ this gain mode was sufficient. However, both amplifiers, operated in the parallel channel mode, would be needed to operate the fluxball machine at it highest rated current of $5\ \text{A}$ at high frequencies.

In series with the fluxball windings were two $1\ \Omega$ resistors. The resistors, arranged in this way, changed the circuit characteristics only minimally while ensuring that changes to the drive circuitry or connections would not affect the winding current measurements. The currents through the measurement resistors were equal to the currents through the fluxball windings and proportional to the voltage across the resistors with a small correction for the actual resistor values, listed in Table 4.3.

The voltages from the current measurement resistors, as well as voltages from the mag-

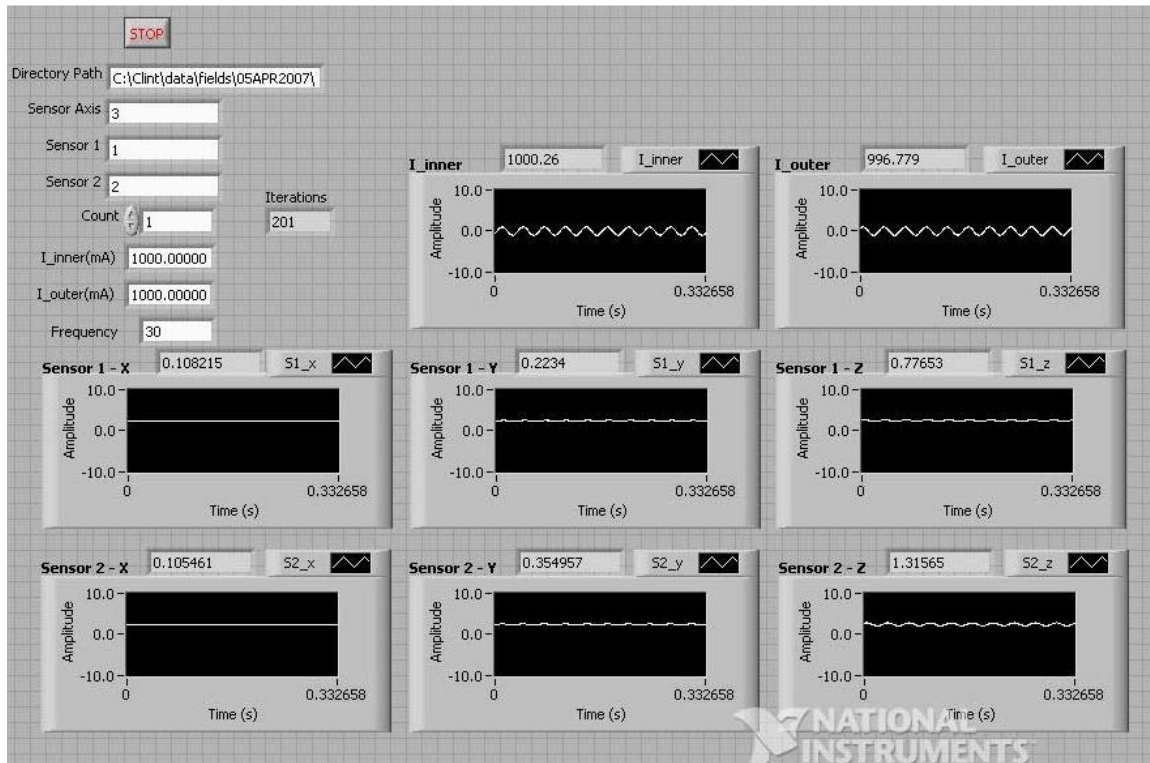


Figure 4-3: A screen shot of the user interface of the LabVIEW program that was used to excite, control, and measure the fluxball machine during operation.

Component	Measured Value
$R_{m_{inner}}$	1.028 Ω
$R_{m_{outer}}$	1.037 Ω

Table 4.3: The measured values of the 1 Ω current measurement resistors.

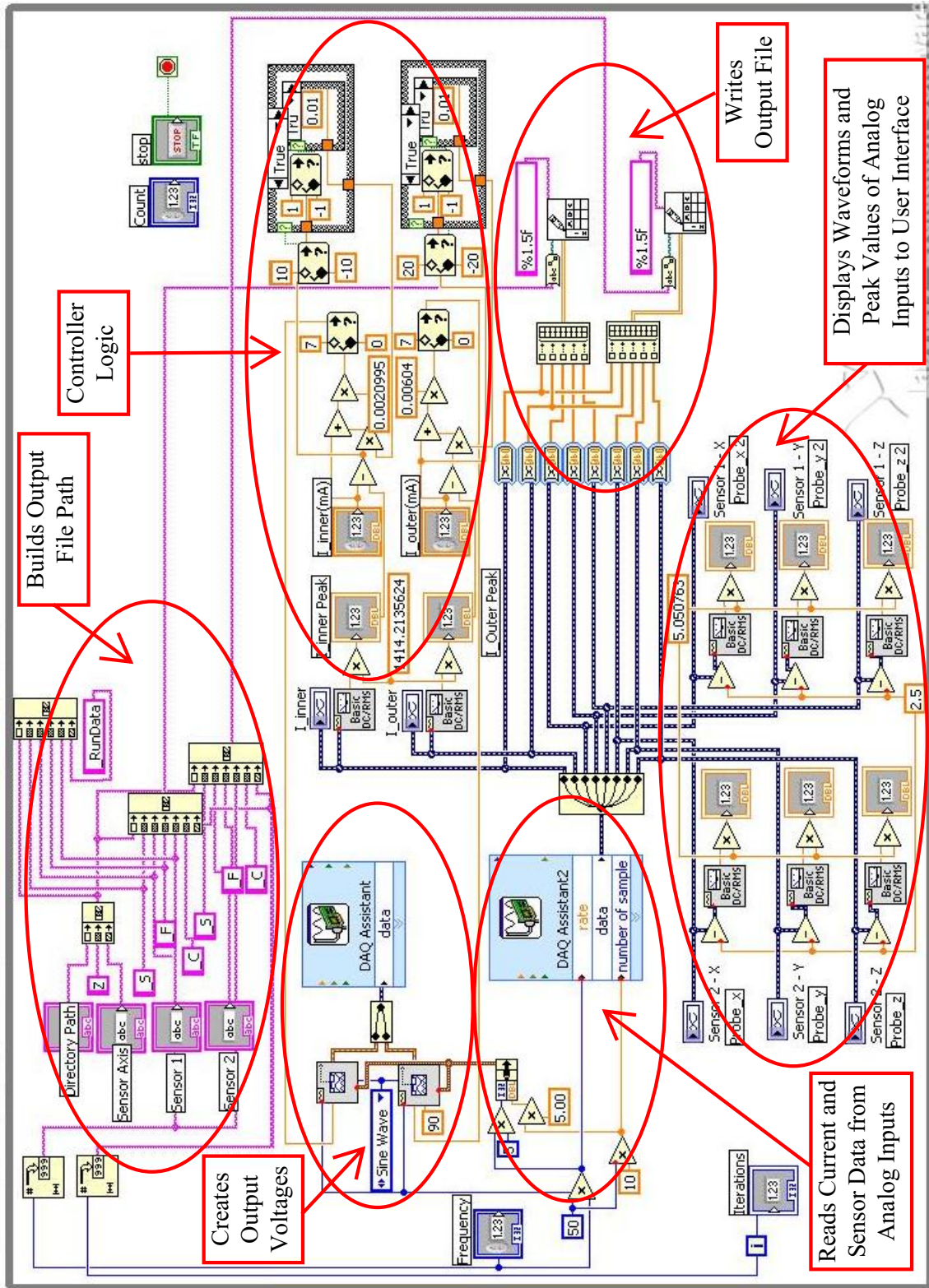


Figure 4-4: An annotated screen shot of the back panel of the LabVIEW program that was used to excite, control, and measure the fluxball machine during operation.

netic field sensor, were then acquired by the eight analog input pins on the BNC 2120. These waveforms were displayed to the screen and written to files for further processing in Matlab. Labview also performed a calculation of the peak current in each winding and used this value to adjust the amplitude of the output voltage in order to maintain a constant current in the winding. The voltage controller was a proportional feedback controller with some saturation logic.

4.3 Operation of the Fluxball Machine

4.3.1 Normal Operation

When operating the fluxball machine at any frequency above a few Hertz, the impedance characteristics are dominated by the inductance of the windings. As the impedance increases the voltage required to provide the same amount of current increases at the same rate. The voltages, \hat{V}_{op} , required for operation at a given frequency and magnetic field density, \hat{B} , can be quickly calculated from the impedance, \hat{Z} , and current, \hat{I}_{op} , of the circuit using eqs. 4.5 and 4.6 and Table 4.2.

$$\hat{V}_{op} = \hat{I}_{op} (\hat{Z}_{winding} + R_m) \quad \text{V} \quad (4.5)$$

$$\hat{B} = 5.4 \hat{I}_{op} \quad \text{mT} \quad (4.6)$$

For convenience, Table 4.4 lists the \hat{V}_{op} required for each winding to produce a magnetic field density of 1 mT in the interior region of the fluxball machine for some particular frequencies.

Table 4.4 demonstrates that it quickly becomes impractical to operate the fluxball machine at *high frequencies* to produce 1 mT, let alone the 25 mT that it was designed to produce. Clearly another mode of operation needed to be devised.

Frequency (Hz)	$\ \hat{V}_{op_{inner}}\ $ (V/mT)	$\angle\hat{V}_{op_{inner}}$ (Deg)	$\ \hat{V}_{op_{outer}}\ $ (V/mT)	$\angle\hat{V}_{op_{outer}}$ (Deg)
1	4.6	2.5	10.8	3.8
5	4.7	12.2	11.4	18.3
10	5.1	23.5	13.0	33.5
20	6.1	40.9	17.9	53.0
30	7.6	52.5	24.1	63.3
40	9.3	60.0	30.6	69.3
50	11.1	65.2	37.4	73.2
60	12.9	69.0	44.3	75.9
70	14.8	71.8	51.3	77.8
80	16.7	73.9	58.3	79.3
90	18.7	75.6	65.4	80.5
100	20.6	77.0	72.4	81.4
200	40.5	83.4	143.7	85.7
300	60.5	85.6	215.2	87.1
400	80.6	86.7	286.9	87.8
500	100.7	87.4	358.6	88.3
1000	201.3	88.7	718.6	89.1

Table 4.4: The operating voltages, \hat{V}_{op} , required for each winding to produce a magnetic field density of 1 mT in the interior region of the fluxball machine.

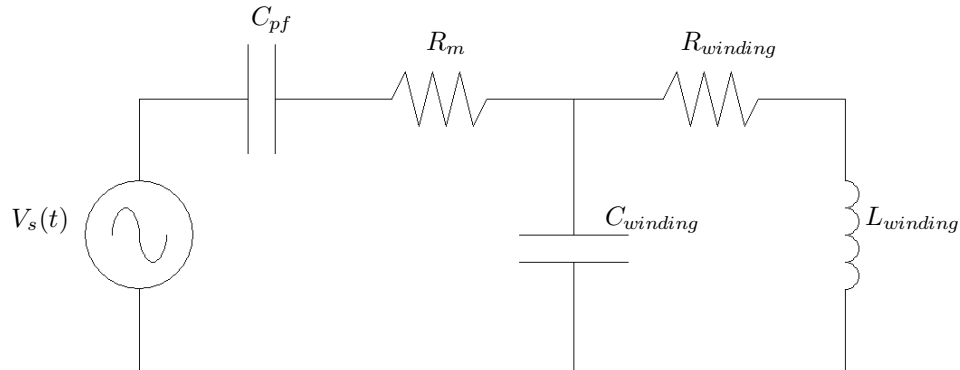


Figure 4-5: The model of one winding of the fluxball machine being operated with a resistor, R_m , for measuring the current, and a capacitor, C_{pf} , for generating resonance in the circuit.

4.3.2 Operation at Resonance

As mentioned above, the problem with the circuit is the large amount of inductance. This problem can be eliminated by adding capacitance into the circuit. When the inductance and capacitance in the circuit is perfectly matched, the impedance seen by the source is purely resistive, and the circuit is said to be in resonance. Sometimes this type of change to the circuit is also called power factor correction because it corrects the angle between the voltage and current waveforms as delivered by the source. Fig. 4-5 shows the model of a fluxball winding with the measurement resistor, R_m , and power factor correcting capacitor, C_{pf} , added to the circuit.

The value of C_{pf} depends on the operating frequency and can be calculated by finding the imaginary part of the winding impedance, $\hat{Z}_{winding}$, setting it equal to the negative of the reactance of the capacitor, and then solving for C_{pf} , as shown in eq. 4.7:

$$C_{pf} = \frac{1}{\omega \operatorname{Im}(\hat{Z}_{winding})} \text{ Farads.} \quad (4.7)$$

When the correct value of C_{pf} is used in the resonant circuit, the imaginary components of the impedance cancel, and the magnitude of the voltage required only depends on the real

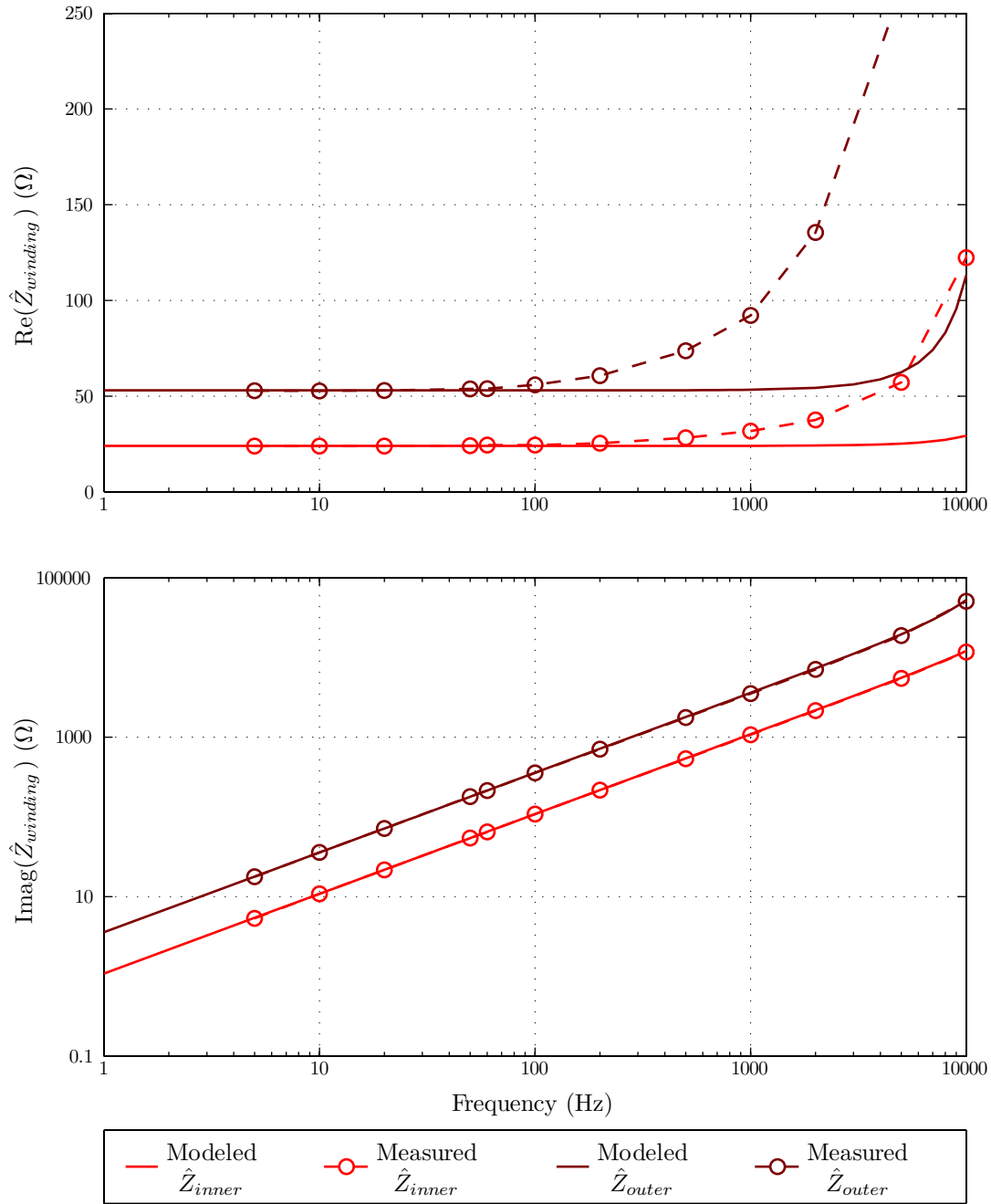


Figure 4-6: The real and imaginary components of the fluxball windings as a function of frequency. The impedance magnitude and phase were measured using a Hewlett-Packard 4192A LF Impedance Analyzer. The modeled values were calculated using the *measured* values given in Table 4.1 and the impedance model given by eq. 4.4 and shown in Fig. 4-1.

part of $Z_{winding}$, given by eq. 4.8:

$$\text{Re}(\hat{Z}_{winding}) = \frac{R_w}{\omega^4(L_w C_w)^2 + \omega^2((R_w C_w)^2 - 2L_w C_w) + 1} \quad \Omega, \quad (4.8)$$

where the subscript, w , refers to the parameter of the given winding.

Fig. 4-6 shows the real and imaginary components of the winding impedance for both windings for the range of frequencies where the fluxball machine would be operated. There is a substantial difference in the measured and modeled values of the impedance at the higher frequencies that is due to measurement error. This error occurs when the angle of $Z_{winding}$ is very close to 90° . Because the angle is so steep, small errors in measurements create very large errors in the calculated values. For this region it is more accurate to use the model than the measurements.

Throughout the frequency range where the fluxball machine will be operated, $\text{Re}(Z_{winding})$ changes its value only slightly. Therefore, a single value for the voltage, \hat{V}_{op} , required to produce a magnetic field density of 1 mT in the interior region can be calculated. The approximate values for \hat{V}_{op} are 5 V and 10.8 V for the inner and outer windings, respectively. This is only true when a perfectly matched C_{pf} is used. Table 4.5 lists resonant capacitor values for particular frequencies.

Looking at the voltage ratings required for the capacitors listed in Table 4.5 it is clear that operation in the resonance mode is not as easy a solution as it first appears. Capacitors rated for alternating current operation in the kilo-Volt range quickly become very large and very expensive.

Frequency (Hz)	$C_{pfinner}$ (μF)	$V_{C_{pfinner}}$ (V)	$C_{pfouter}$ (μF)	$V_{C_{pfouter}}$ (V)
1	147,000	5	44,400	20
5	5,860	30	1,780	90
10	1,460	60	444	180
20	366	120	111	360
30	163	170	49.4	540
40	91.6	220	27.8	720
50	58.6	280	17.8	900
60	40.7	330	12.3	1,080
70	29.9	380	9.07	1,260
80	22.9	440	6.94	1,440
90	18.1	490	5.47	1,620
100	14.7	550	4.44	1,800
200	3.67	1,090	1.11	3,590
300	1.63	1,630	0.494	5,370
400	0.916	2,180	0.278	7,200
500	0.586	2,720	0.178	8,960
1000	0.146	5,440	0.044	18,000

Table 4.5: Capacitors, C_{pf} , required to create resonance in the fluxball windings at particular operating frequencies. $V_{C_{pf}}$ is the required voltage rating for C_{pf} operation at maximum rated current of 5 A.

Chapter 5

Sensor Calibration

5.1 Sensors

5.1.1 Hall Effect

The Hall Effect was discovered by Edwin Hall in 1879. Hall observed that current flowing perpendicular to a magnetic field was deflected by the Lorentz force on the charge carriers. The deflection of the charge carriers created an accumulation of charge on the faces of the conductor. This accumulation of charge gave rise to a potential difference across the volume of the conductor that could be measured across the faces of the conductor. Fig. 5-1 describes this phenomenon in greater detail.

Modern Hall effect sensors, like the ones described in this chapter, are fabricated from semiconductors and incorporated into integrated circuit chips that condition the voltage signal in a variety of ways. Often this conditioning includes amplification and temperature compensation.

5.1.2 F.W. Bell Three Axis Probe and Teslameter

Fig. 5-2 shows the F.W. Bell Hall effect three axis magnetic probe and 7030 advanced triple channel digital Teslameter. The specifications for this system are included in Appendix D. The Tesla-meter was acquired by the laboratory in August of 2002, and the three axis probe was purchased in March of 2007. The Tesla-meter has not been calibrated since arriving at

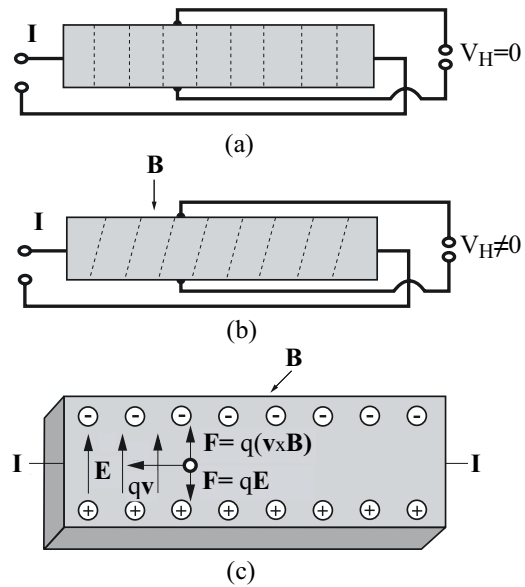


Figure 5-1: The Hall voltage, V_H , generated in a conductor carrying current I by the magnetic field B (a) when $B = 0$, (b) when $B \neq 0$, and (c) in the cross section of the conductor when $B \neq 0$. Diagrams (a) and (b) show the lines of equipotential inside the conductor. Diagram (c) describes the force mechanisms on the charge carriers [43].

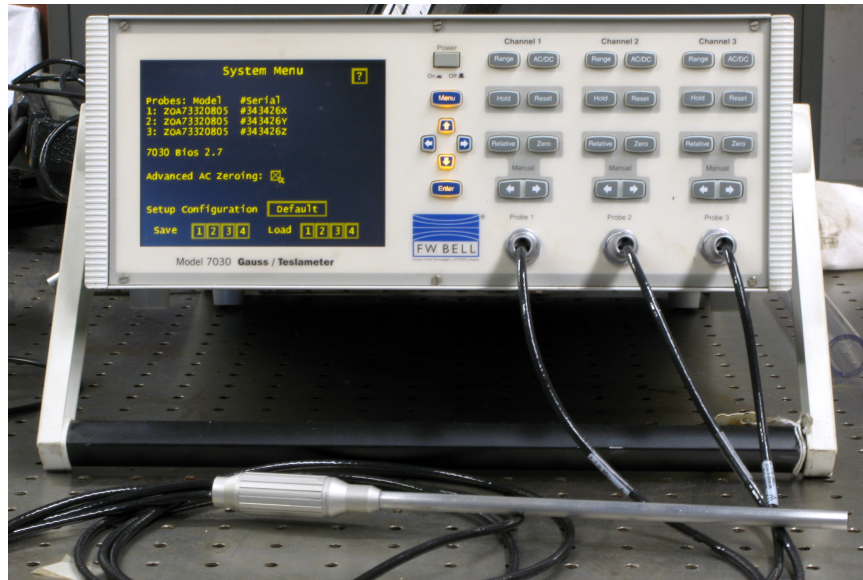


Figure 5-2: The F.W. Bell three axis probe and 7030 Teslameter System.

the laboratory. The total cost of this system was \approx \$8,000.

Before any data was taken, all channels were zeroed using *Advanced AC Zeroing* option. All calibration data was collected from the probe using the corrected analog output terminals. Each channel was kept in the 3.0 mT setting, and the analog outputs were in the 3.0 V setting.

5.1.3 GMW Three Axis Sensor

Fig. 5-2 shows the GMW Hall effect three axis magnetic sensor. The specifications for these sensors are included in Appendix D. Six of the GMW sensors were purchased in March of 2007. The cost of each sensor was \approx \$35. Small sensors of this type were desired because they could be placed in the interior region of the fluxball machine in order to verify the strength and uniformity of the magnetic field.

The GMW sensors were supplied a constant 5.0 V DC supply voltage. Voltage signals were read from the pins of the sensors using a shielded 18 conductor data cable.

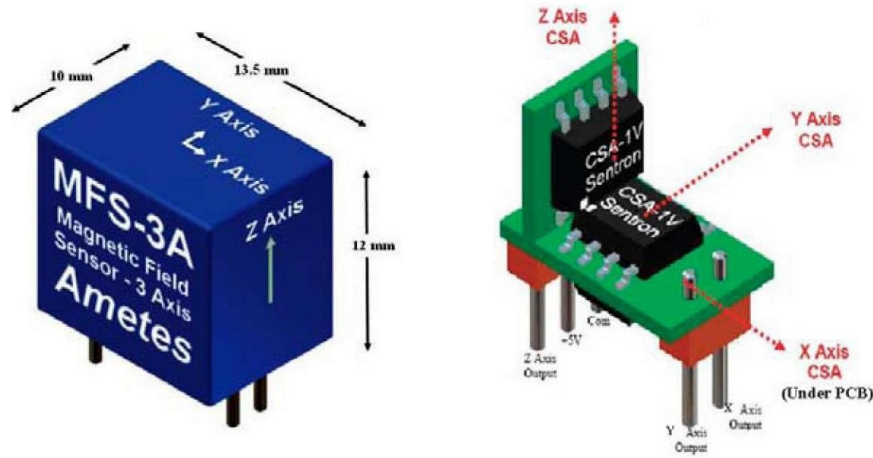


Figure 5-3: GMW three axis sensor.

5.2 Calibration Equipment

5.2.1 Reference Magnetic Field

The inner fluxball winding was used to create a reference magnetic field. The fluxball was arranged so that there was a 38 mm gap between the two hemispheres. This allowed for room to insert and manipulate the probe and sensors during the calibration procedure. The magnetic field created by the fluxball could be calculated numerically using the Biot-Savart Law; this gave a predicted magnetic field of 4.08 mT. The field was then measured at DC with each element of the three probe F.W. Bell Hall Effect probe. All sensors agreed that the reference magnetic field, B_z , was directly proportional to the current in the winding, with the proportionality constant, α , equal to 4.47 mT/A. Therefore the z directed magnetic field could be calculated from the winding current, I , using eq. 5.1.

$$B_z = \alpha I \quad \text{mT}, \quad \alpha = 4.47 \quad \text{mT/A} \quad (5.1)$$

Fig. 5-4 show the magnetic field lines for the fluxball in the calibration arrangement.

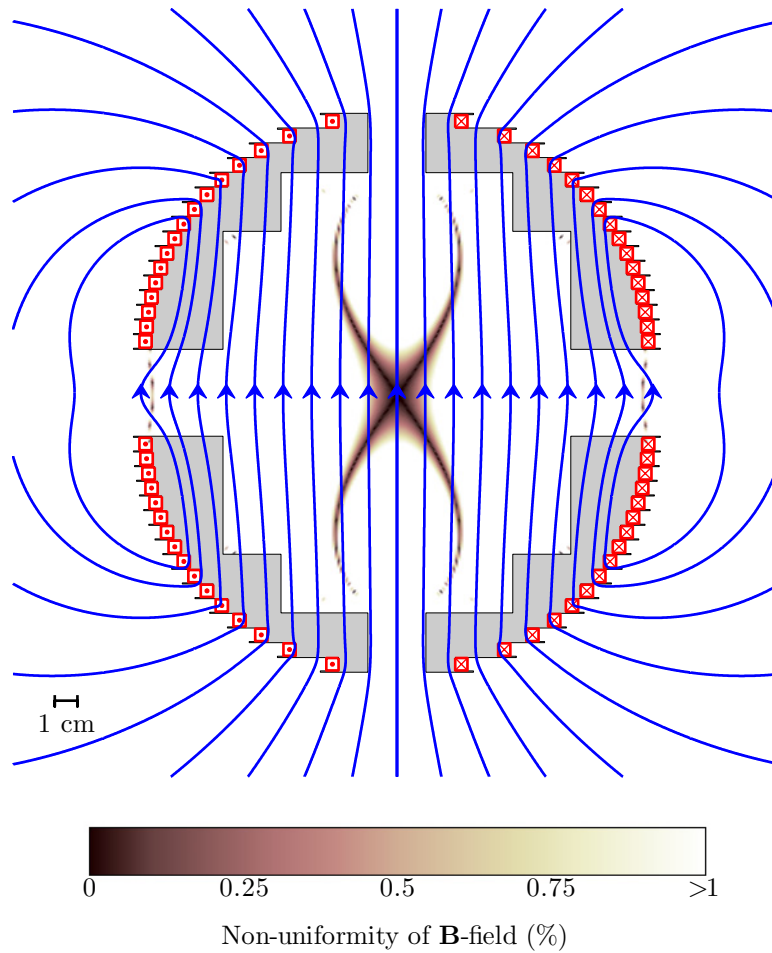


Figure 5-4: The geometry and magnetic field lines for the inner fluxball as set-up for calibration procedures. The gap between the hemispheres is 38 mm. The shading on the plot shows the region in which the magnitude of the magnetic field is uniform to within 1%.

5.2.2 LabVIEW Interface

LabVIEW was used as the primary tool for controlling the fluxball current, monitoring the sensors, and taking measurements. A program was design to automate the data acquisition process so that multiple frequencies and current amplitudes could be tested in a quick and precise way. Data was acquired for a range of frequencies between 1Hz and 1kHz and a range of field strengths between 0 and 5 mT. The upper limit on the field strength was set by the sensitivity ranges on the F.W. Bell Teslameter. Going above 5 mT put the device in a new sensitivity range that could not be changed automatically. This was not really a limitation because of the proportionality of the reference field and because the GMW sensors began to clip at 7.3 mT. The LabVIEW user interface used to control the reference magnet during the calibration procedures was very similar to the one shown in Fig. 4-3.

5.2.3 Data Processing in Matlab

The raw waveform data was written into text files by the LabVIEW program. This data could then be read into the Matlab workspace and processed. The processing routine involved taking the raw waveform and calculating the peak magnetic fields on each sensor. Each text file contained five waveforms. The first two waveforms were the voltages measured across the $1\ \Omega$ resistors that were placed in series with the inner and outer magnet windings. During calibration procedures only the inner winding was energized. The third, fourth, and fifth waveforms corresponded to the voltages produced by the x , y , and z Hall effect elements. Fig. 5-5 shows the voltage waveform data for a case where both windings are energized.

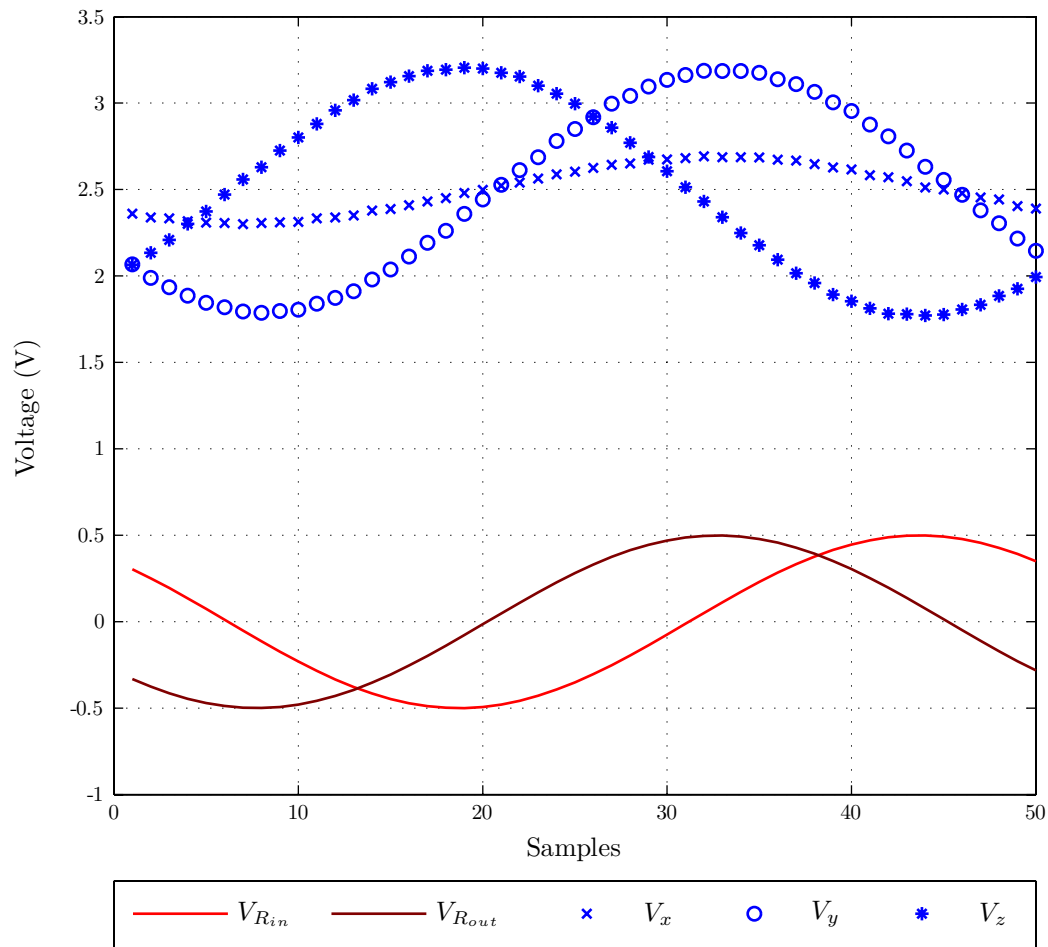


Figure 5-5: The raw voltage waveform data prior to processing in Matlab. One period of data, corresponding to 50 samples, for the GMW sensor is shown. V_x and V_y are excited by the current in the outer winding and are, therefore, proportional to the voltage measured on the outer winding measurement resistor, $V_{R_{out}}$. Similarly, V_z is proportional to $V_{R_{in}}$; however, the direction is exactly opposite. This orientation was chosen for the GMW sensors so that they could be positioned as closely as possible to the F.W. Bell probe elements.

5.3 Procedure

A special apparatus was designed and built in order to keep the probe and sensor aligned along all three axes. Figs. 5-6 and 5-7 show this device.

Both devices were calibrated against the reference field by exciting one axis of the sensor at a time. Care was taken to assure that the excitation at each sensor was precisely the same by positioning the sensors at the exact center of the reference field. Additionally, the excitation of the sensor in the axis being calibrated was ≈ 100 times greater than the excitation of the off axis elements. Figs. 5-8-5-11 show the calibration arrangements for all three axes.

For the x and z elements three independent calibration runs were conducted across the range of frequencies and field intensities. The first two runs were conducted one day and then a third run was conducted on the following day. The sensors were left energized and the geometry was unchanged between the second and third runs. For the y element two runs were conducted on the same day. The entire procedure was completed in three days.

Once the data was collected, the probes were calibrated by fitting the data to the known field using a third order polynomial fit. All of the data from a single run was used to generate the fit. Higher order fits were tried, but they resulted in only marginally better fits. Subsequent runs were plotted using the new fit to verify that it was correct.

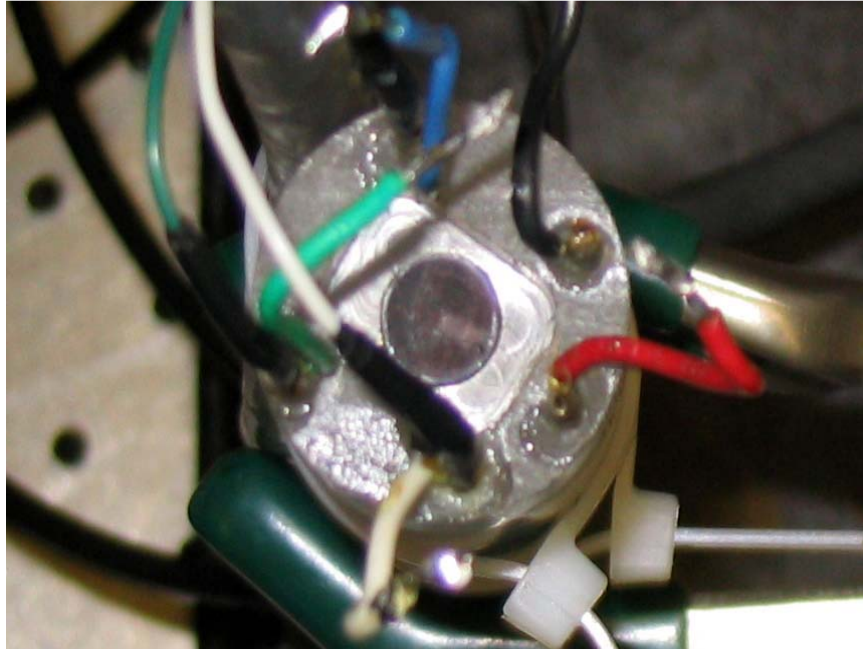


Figure 5-6: Probe and sensor alignment apparatus with GMW sensor removed. The circular tip of the F.W. Bell probe can be seen; it is flush with the bottom of the milled slot for the GMW sensor.

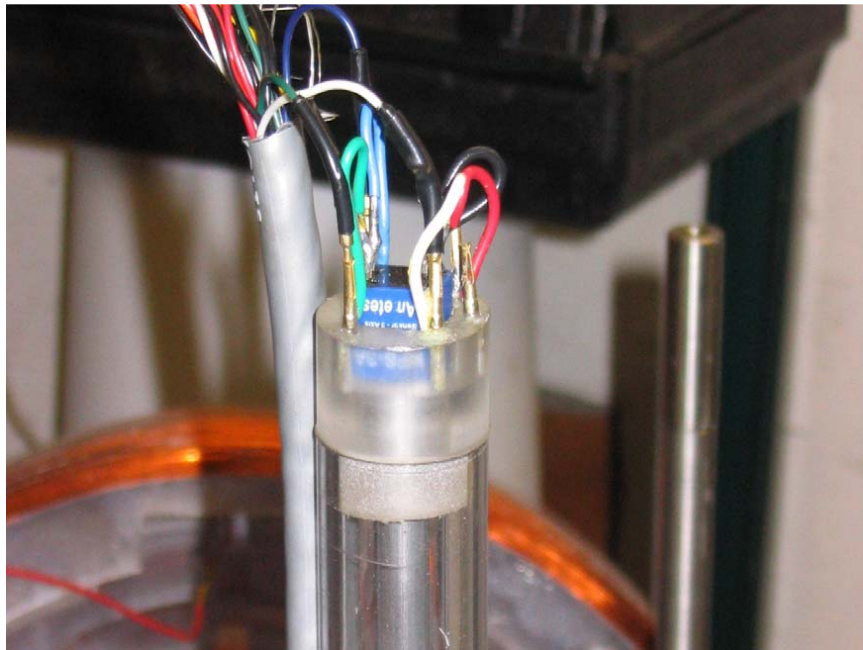


Figure 5-7: Probe and sensor alignment apparatus with GMW sensor installed.

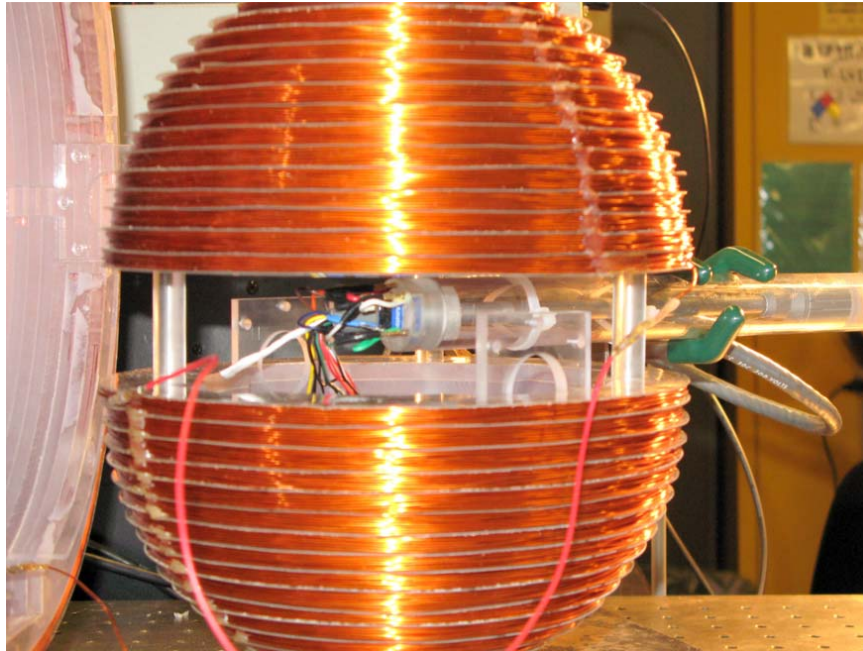


Figure 5-8: Calibration set-up for x and y axis Hall effect elements.

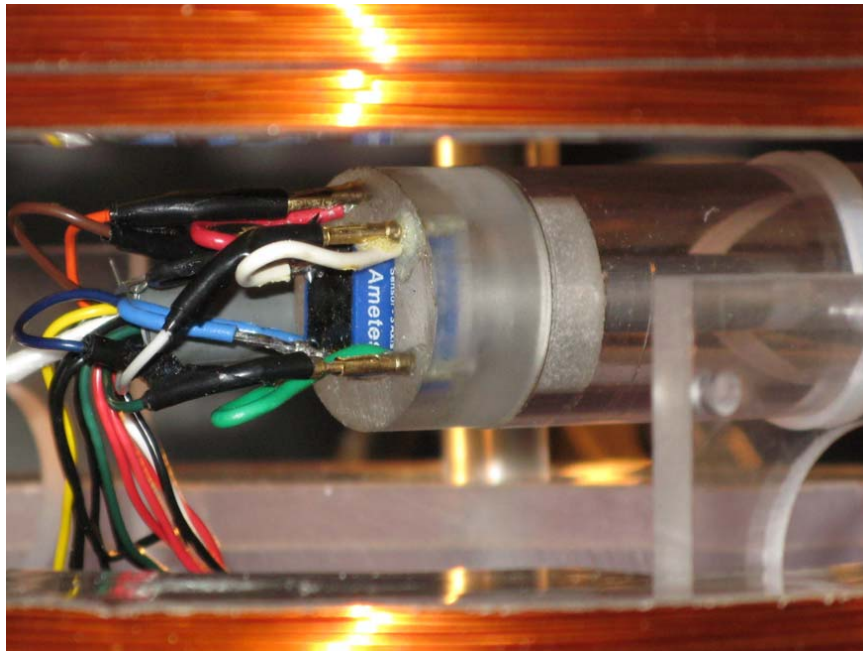


Figure 5-9: A close-up view of the calibration set-up for x and y axis Hall effect elements.

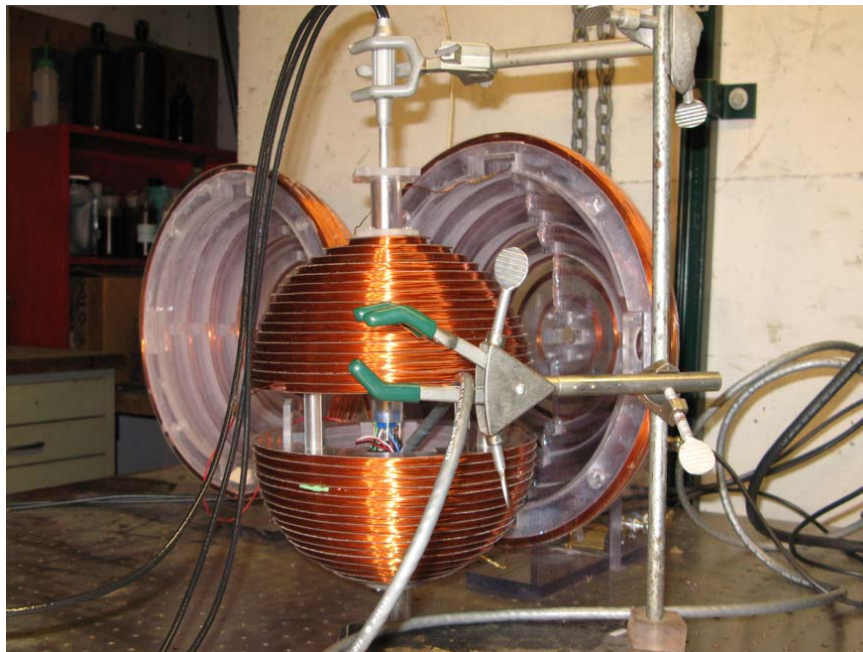


Figure 5-10: Calibration set-up for z axis Hall effect element.

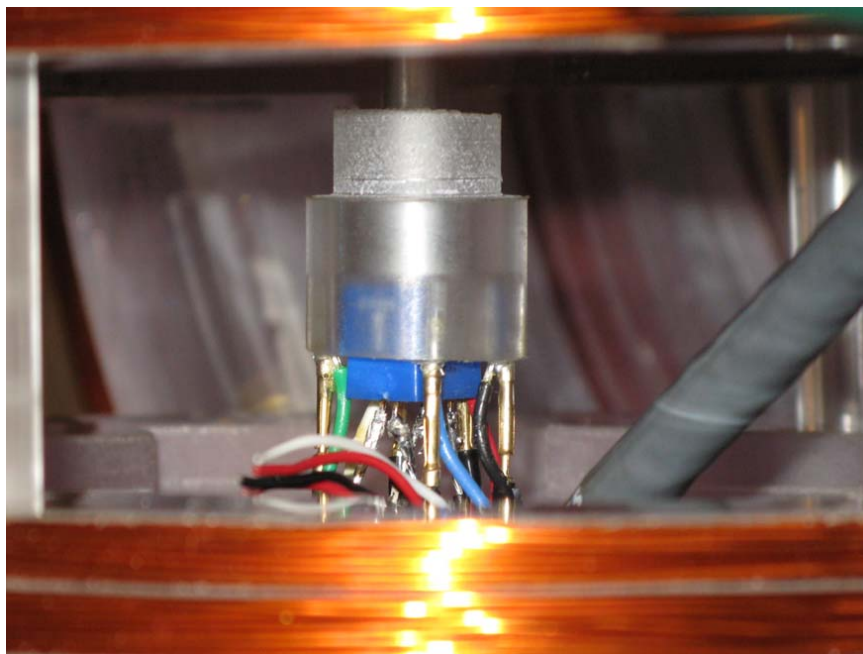


Figure 5-11: A close-up view of the calibration set-up for z axis Hall effect element.

5.4 Results

The calibration procedure was completed for the F.W. Bell probe and for one of the six GMW sensors. The F.W. Bell sensor generally gave better precision across field strengths and frequencies. However it had very poor accuracy in the y and z axis elements, indicating that the systems needed to be calibrated by the manufacturer. Using the known field to calibrate the probe the absolute error could be reduced to less than $25 \mu\text{T}$. Additionally, the calibrated error grew with the field strength so that the error never exceeded 1% of the actual magnetic field. Fig. 5-12 shows the error in the F.W. Bell probe before and after the calibration procedure.

The GMW sensors showed very good initial calibration. The absolute error across the sensor sensitivity range was $\approx \pm 0.05 \text{ mT}$. Unlike the F.W. Bell system, the error curve had a distinctly non-linear shape. This shape can be seen in Fig. 5-13. The sensor measurements were very repeatable and had no significant frequency dependency. All three sensors elements gave the best accuracy around 5 mT. Fitting this data to the known field did not significantly improve the accuracy of the sensors.

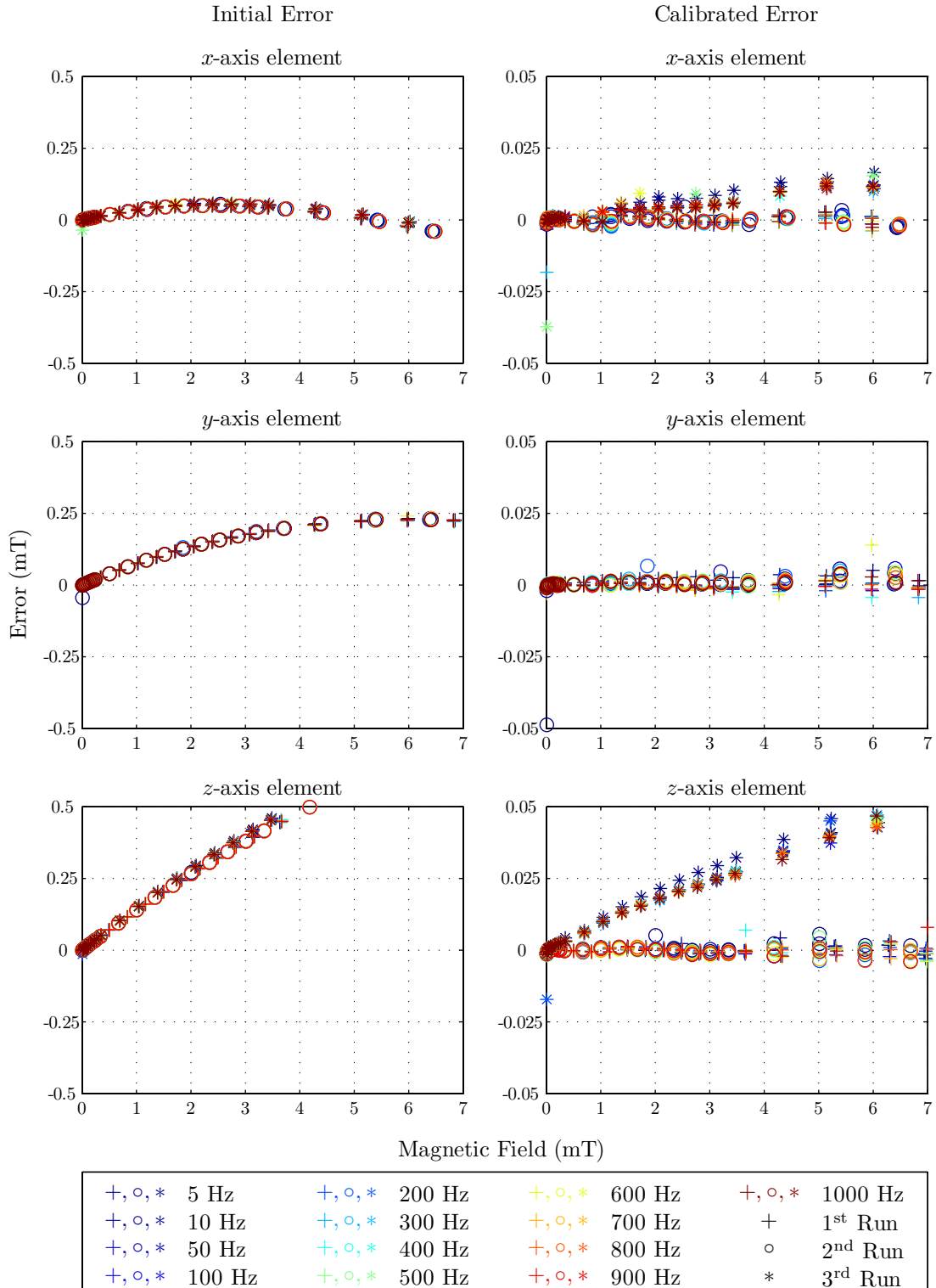


Figure 5-12: The initial and calibrated error for each element of the F.W. Bell three axis Hall effect probe and Teslameter system. Each element was calibrated using a single set of data points for one frequency of one run.

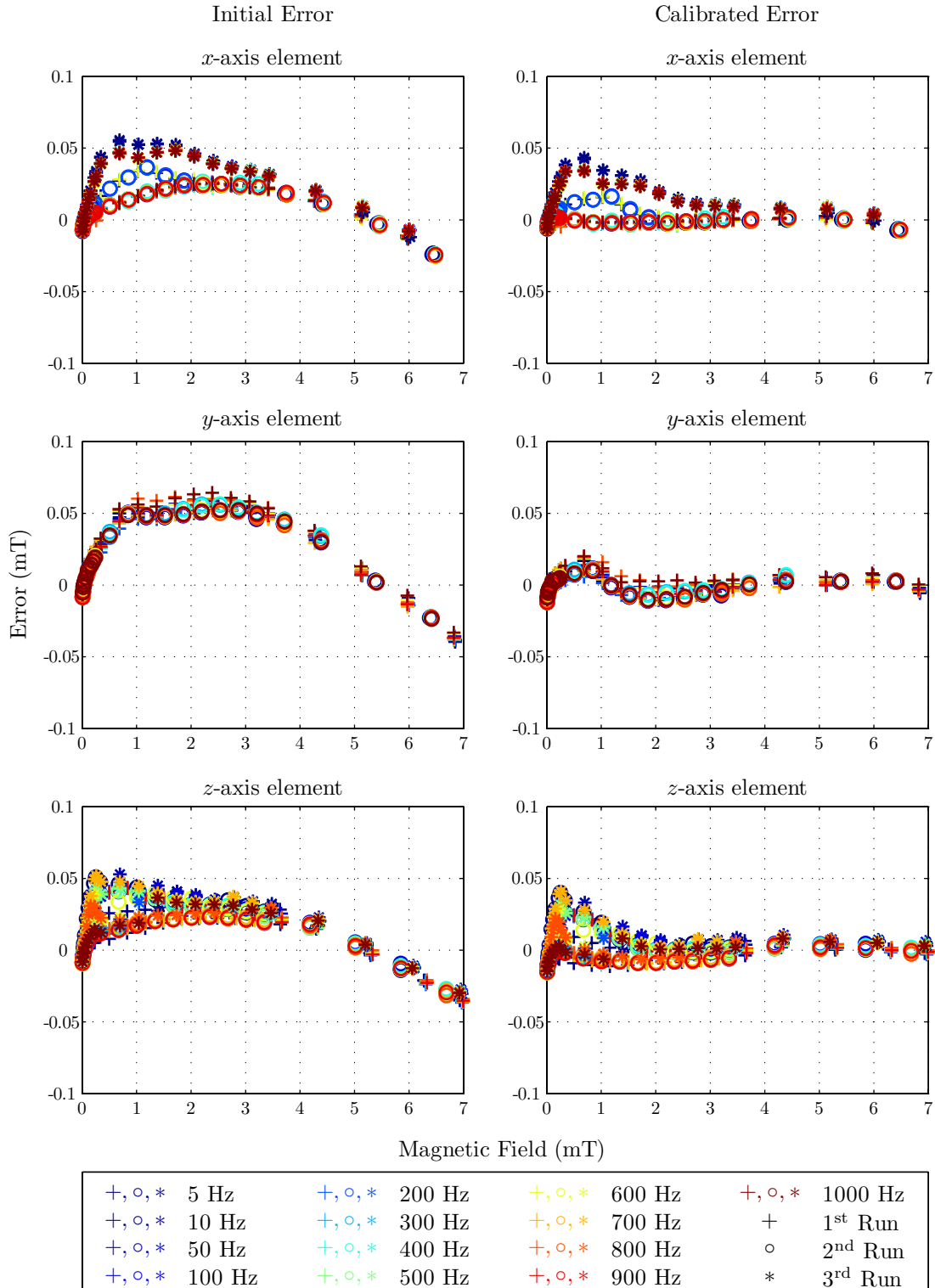


Figure 5-13: The initial and calibrated error for each element of the GMW three axis Hall effect sensor. Each element was calibrated using a single set of data points for one frequency of one run

Chapter 6

Magnetic Field Measurements

6.1 Predicted Magnetic Field

The mathematical machinery for predicting the magnetic fields of the fluxball machine was developed in Chapter 2. Using the current loop as the basic unit of current and neglecting pitch in the current, the predicted field densities were calculated numerically. Fig. 6-1 shows the field lines and predicted non-uniformity of the fluxball machine. The current systems of the fluxball machine are irrotational (i.e. $\nabla \times \mathbf{B} = 0$), which means that all magnetic field lines should close on themselves. Due to numerical limitation in the “streamline” plotting function in matlab, this does not always happen.

6.2 Measured Magnetic Field

The calibration procedures described in Chapter 5 showed that the GMW sensors, using the specified sensitivity of 280 mV/T, were accurate to ± 0.05 mT. Around 5.0 mT the GMW sensors had an accuracy closer to ± 0.015 mT. Therefore, the windings of the fluxball were excited with AC signals of 1 A peak amplitude, generating a peak field of ≈ 5.4 mT and providing measurement accuracy in excess of $\pm 1.0\%$. Sensors were placed at six different locations in the interior volume of the fluxball machine as shown in Fig. 6-2. A new apparatus was constructed to accurately position the sensors in the fluxball machine. Figs. 6-3 and 6-4 show the sensor platforms with the GMW sensors installed. Two different

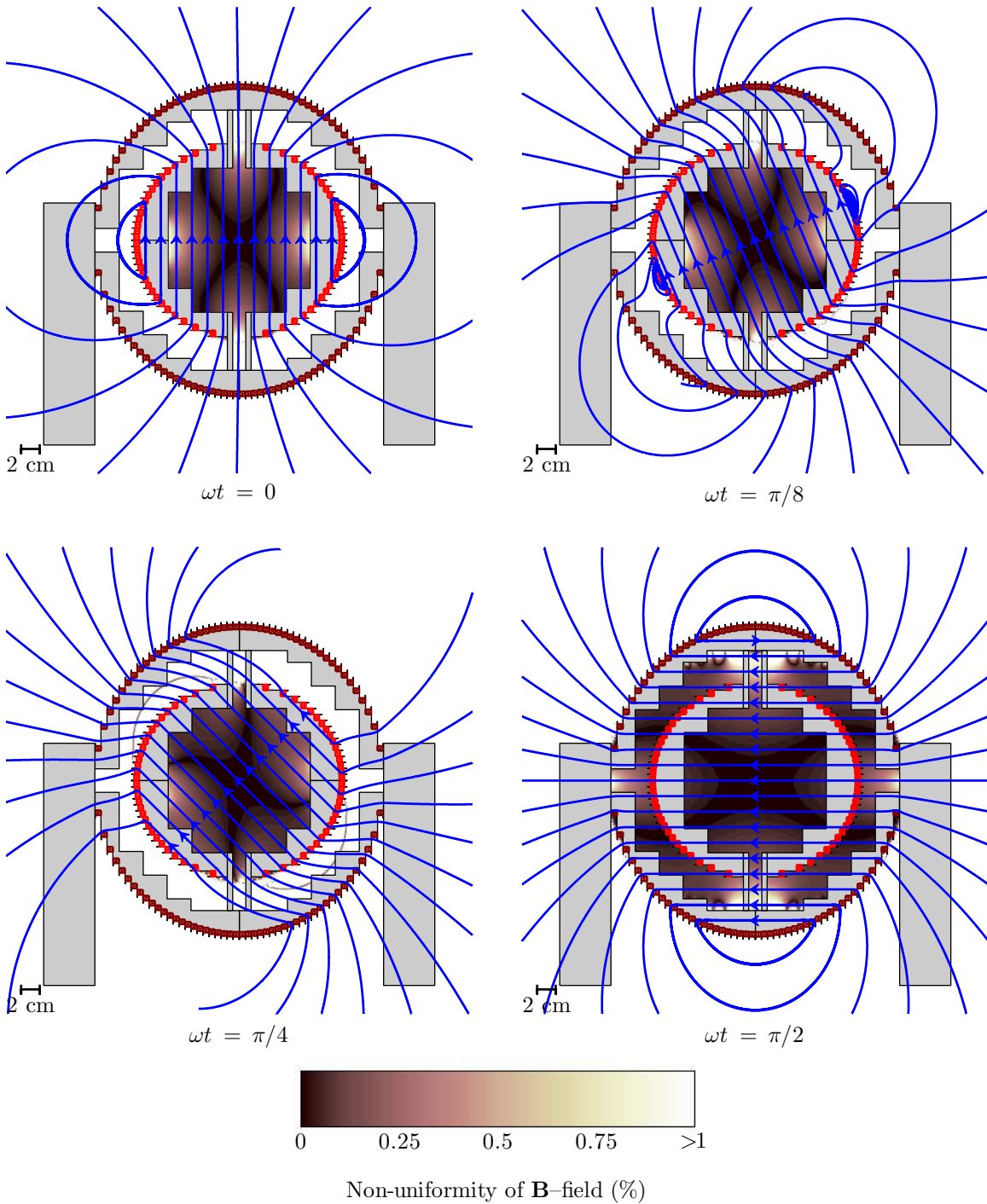


Figure 6-1: The predicted magnetic field lines and percent of non-uniformity of the magnetic field produced by the fluxball machine as built. The windings are energized with currents that are 90° out of phase. $I_{inner} = i_0 \cos(\omega t)$ and $I_{outer} = i_0 \sin(\omega t)$. The open field lines are due to numerical limitations; they are not physical.

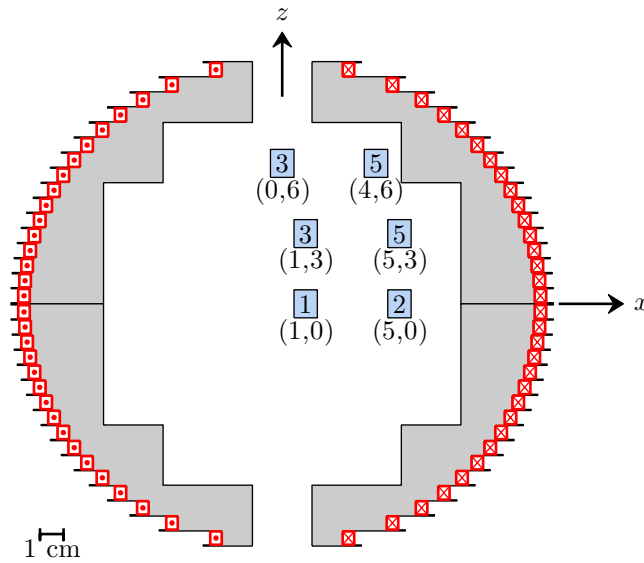


Figure 6-2: The locations of the sensors inside the fluxball machine for magnetic field measurements. The number and coordinates, (x, z) , of each sensor are shown. All sensors were located at $y = 0$. The sensors are drawn to scale.

configurations had to be used to take all of the data. The first set was taken with two sensor platforms mounted on a guide rail that was machined to fit into the access tubes, thereby maintaining vertical alignment. The second set of data was taken with just one sensor platform shimmed to the top of the inner winding structure. A 30 Hz AC waveform was used to excite the fluxball winding for all of the field uniformity measurements.

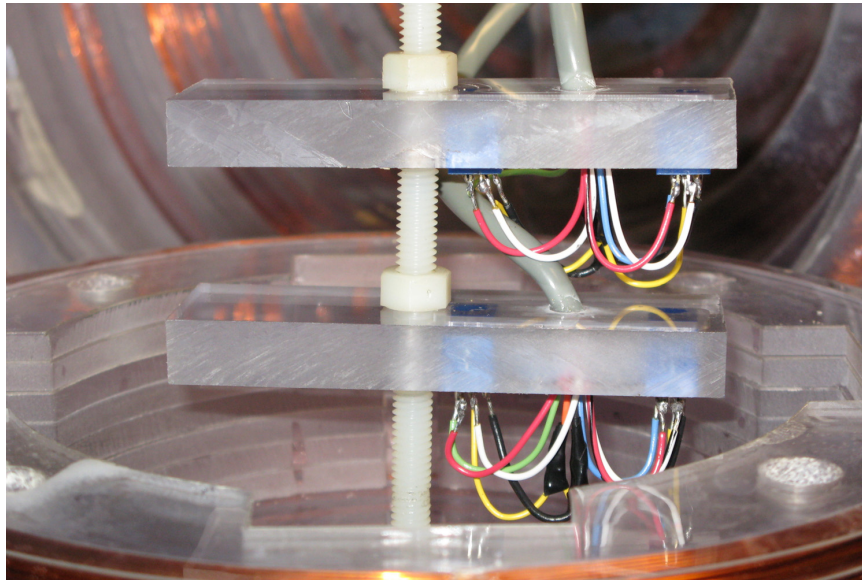


Figure 6-3: The side view of the sensor platform apparatus. The sensors were placed tightly into a milled slot 4 cm apart from each other. The platforms were threaded onto a 20 cm nylon screw and secured with lock washers. The data cables were run out of the machine through the cable-ways, and the screws were capped with cylinders that fit tightly into the access tubes.

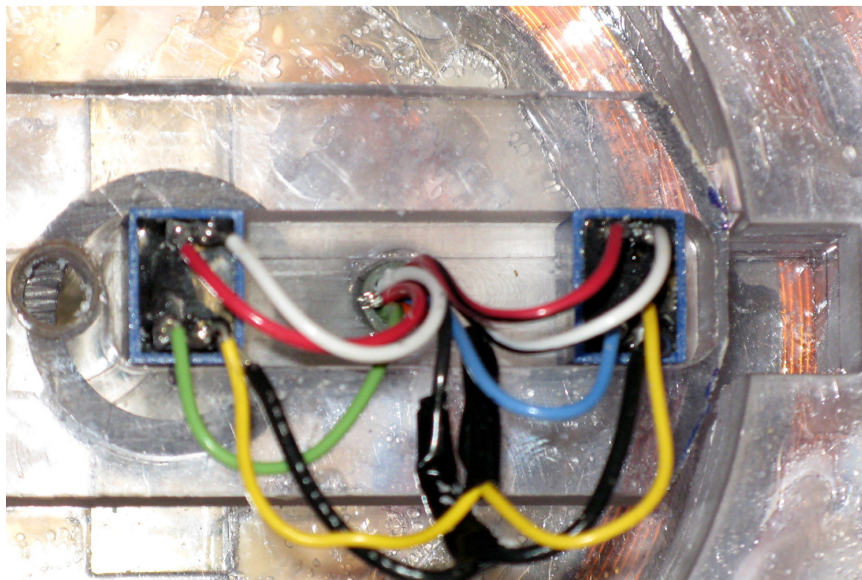


Figure 6-4: The top view of the GMW sensor platform shimmed to the top of the inner fluxball structure.

6.3 Magnetic Field Uniformity

Measurements of the magnetic fields were taken with each winding energized alone and then with both windings energized. Figs. 6-5–6-7 show the results of these measurements. The inner winding produced magnetic fields that were z -directed, while the outer winding produced magnetic fields that were x -directed. When each coil was energized alone the magnetic field components along the two axes orthogonal to the winding axis were negligible. When both windings were operated simultaneously both x and z directed fields were measured, producing very similar values to those measured when each coil was excited alone.

Fig. 6-8 shows one period of the measured data for each sensor, as well as the predicted magnetic field. The waveforms follow each other nicely, showing no distortion of the magnetic field. The measured waveforms had a larger amplitude, in the range of 5–9%, than the predicted waveforms, as shown in Tables 6.1 and 6.2. The reasons for this error are discussed in Chapter 7.

The mechanism for creating a rotating field is clearly present; however, the phase difference between the x and z directed fields is not 90° deg. This occurred because the windings were excited with voltages, rather than currents, that were 90° deg out of phase. As discussed in Chapter 4, the impedance characteristics of the winding are different and therefore the angle between the voltage and the current is different. A slight adjustment must be made to the phase difference in the excitation voltage waveforms in order to account for this. This correction depends on the operating frequency. Using the LabVIEW drive circuitry discussed in Chapter 4 this correction is easily applied.

Tables 6.1 and 6.2 list the predicted and measured magnetic field strength at the sensor's locations, as well as the error of the prediction and the non-uniformity of the field.

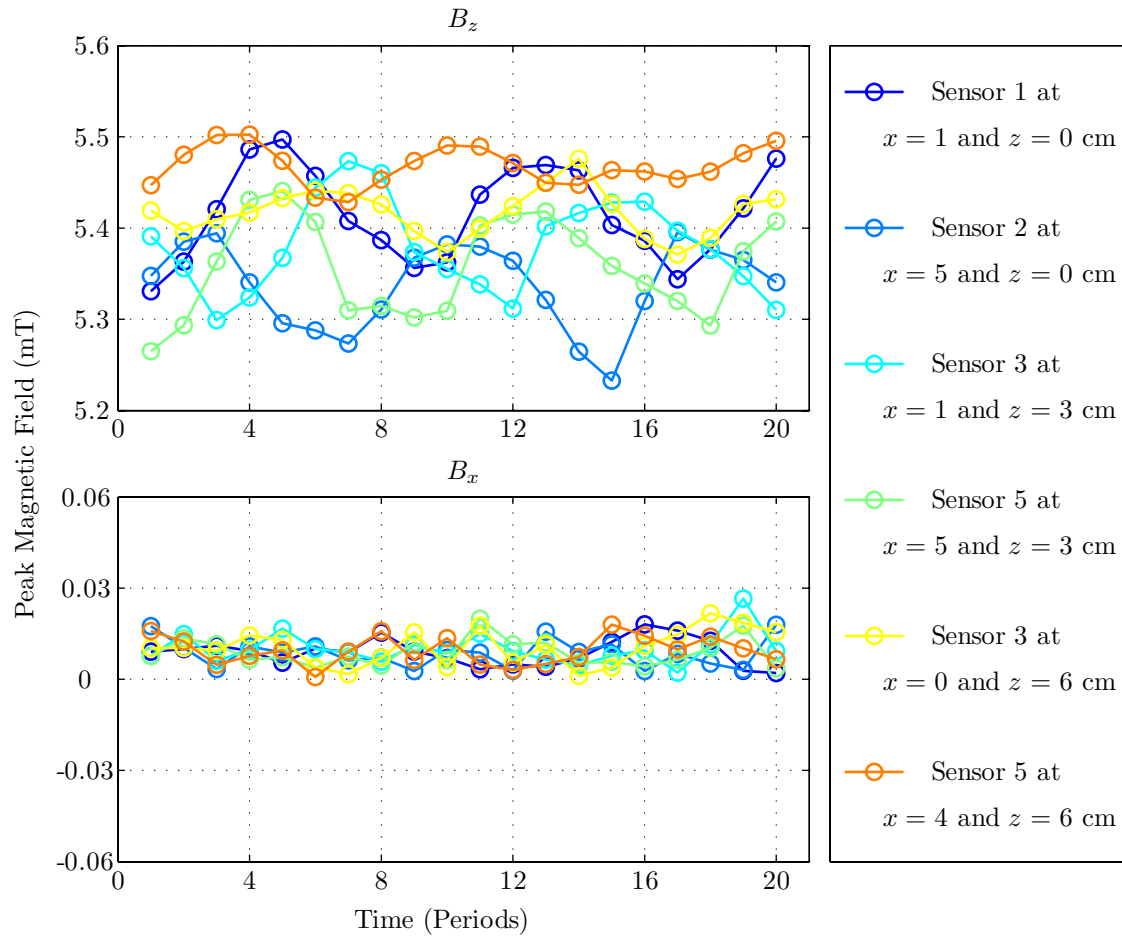


Figure 6-5: The peak magnetic field density inside the fluxball machine with only the inner winding excited by a 30 Hz AC signal with a peak amplitude of 1.0 A. The peak values have been measured over 20 periods and corrected for slight deviations in the winding current from the 1 A peak amplitude.

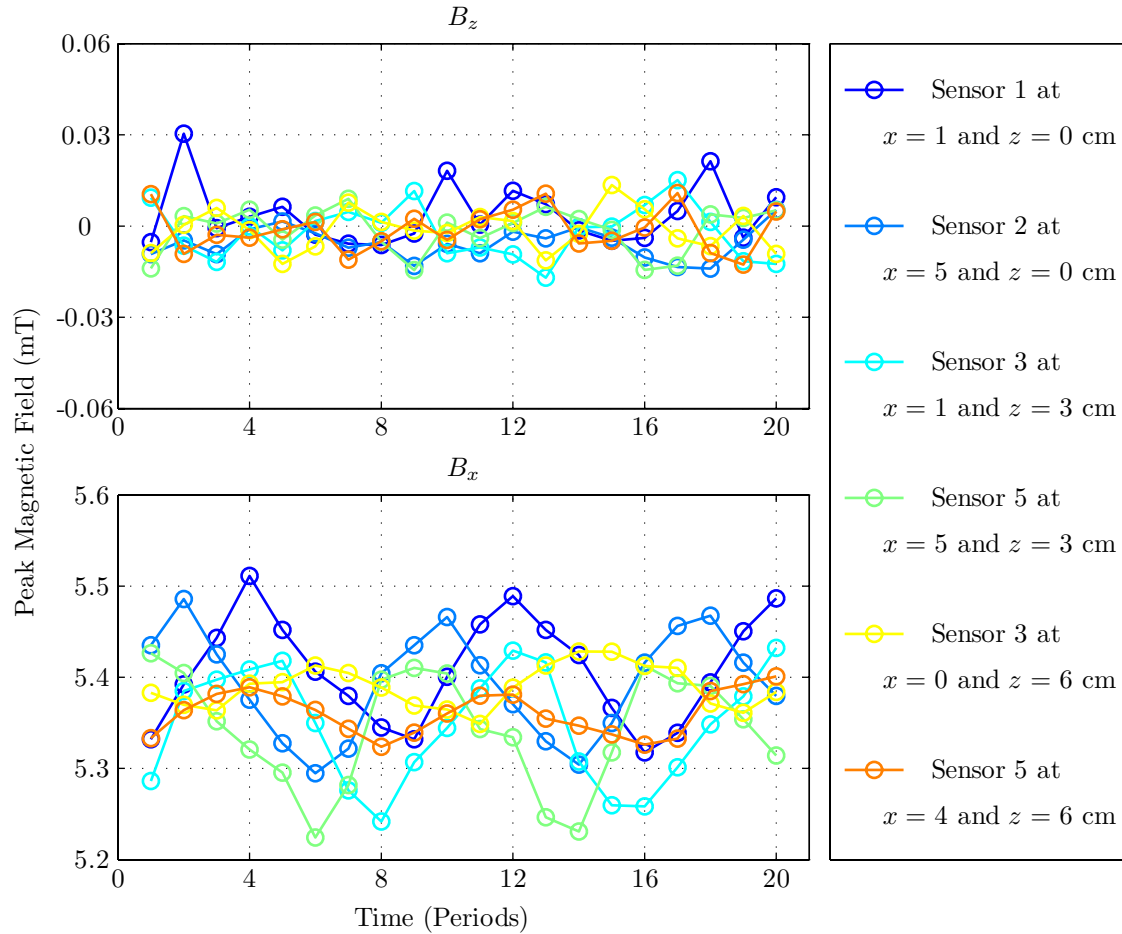


Figure 6-6: The peak magnetic field density inside the fluxball machine with the outer winding excited by a 30Hz AC signal with a peak amplitude of 1.0 A. The peak values have been measured over 20 periods and corrected for slight deviations in the winding current from the 1 A peak amplitude.

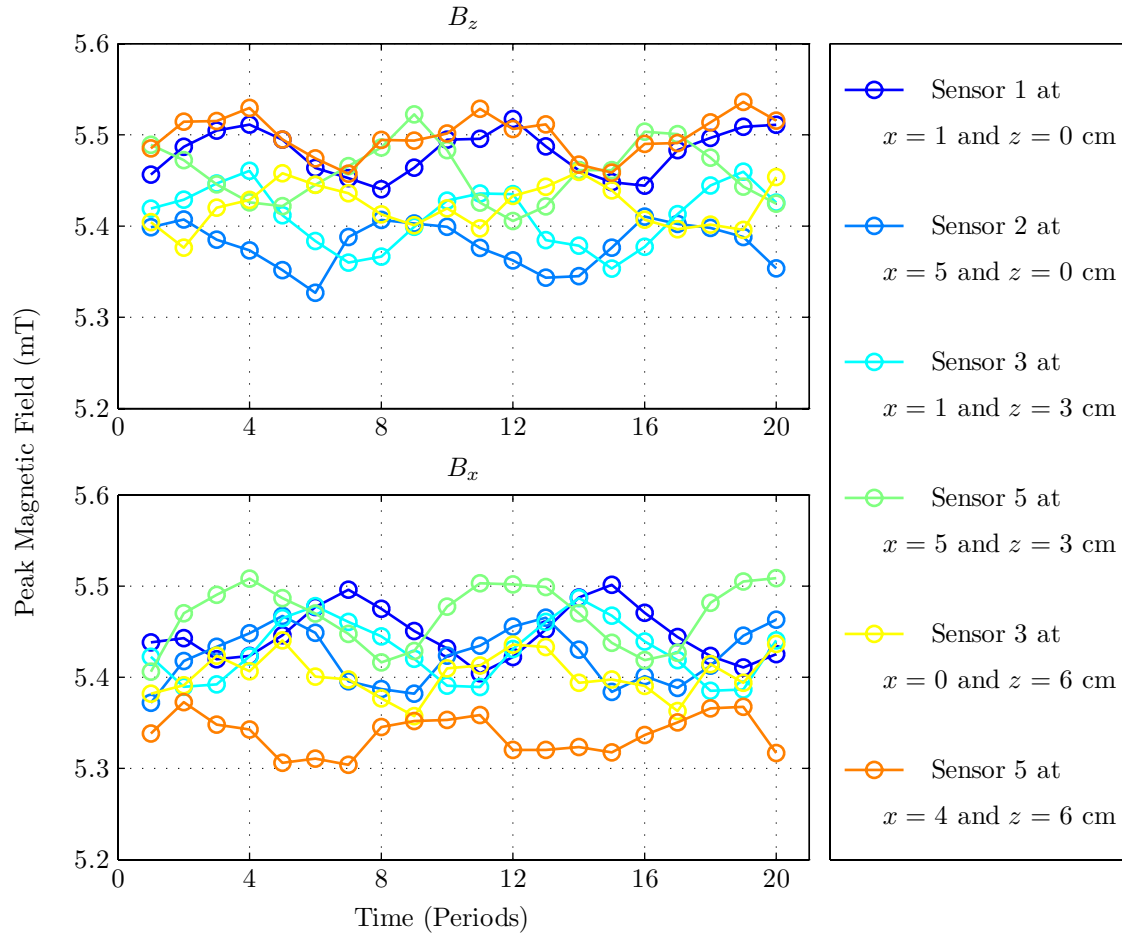


Figure 6-7: The peak magnetic field density inside the fluxball machine with both windings excited by a 30 Hz AC signal with a peak amplitude of 1.0 A. The peak values have been measured over 20 periods and corrected for slight deviations in the winding current from the 1 A peak amplitude.

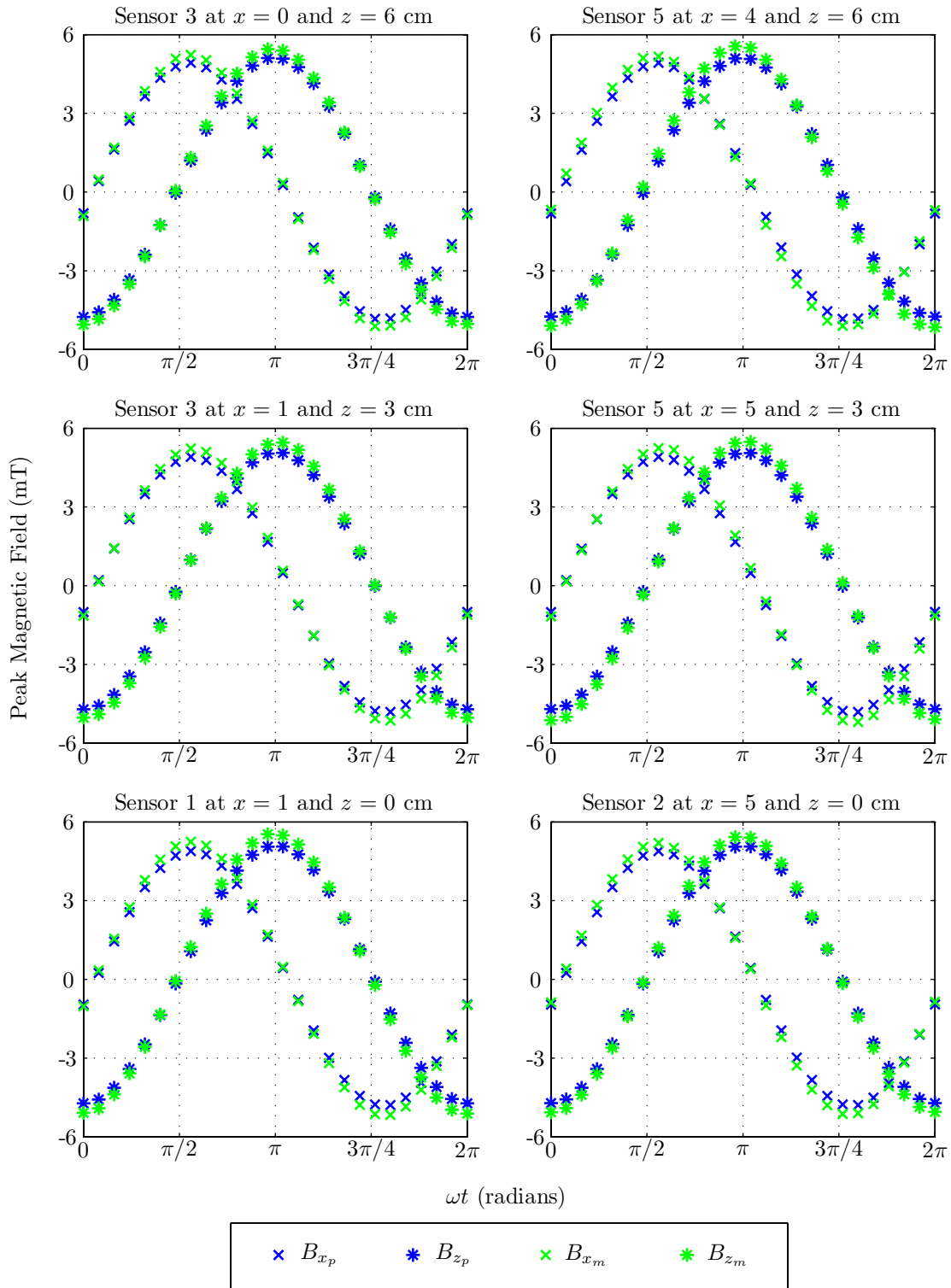


Figure 6-8: One period of the predicted, B_p , and measured, B_m , magnetic field strength at each sensor when both windings are energized with 1 A peak amplitude 30 Hz currents.

Sensor Number	Position x (cm)	Position z (cm)	Predicted B_x (mT/A)	Measured B_x (mT/A)	Error B_x (%)	Non-uniformity B_x (%)
1	1	0	5.06	5.45	7.0	0.3
2	5	0	5.06	5.42	6.6	0.1
3	1	3	5.06	5.43	6.7	0.0
5	5	3	5.06	5.47	7.4	0.7
3	0	6	5.07	5.40	6.2	0.5
5	4	6	5.06	5.34	5.1	1.7

Table 6.1: The predicted and measured values of x -directed magnetic field density at each of the sensor locations with both windings energized. The measured values have been averaged over 20 periods. The field strength at the center of the test chamber is 5.43 mT/A. Both windings have been excited with 1 A peak amplitude 30 Hz currents, with the phase relationship shown in Fig. 6-8.

Sensor Number	Position x (cm)	Position z (cm)	Predicted B_z (mT/A)	Measured B_z (mT/A)	Error B_z (%)	Non-uniformity B_z (%)
1	1	0	5.02	5.48	8.5	0.9
2	5	0	5.01	5.38	6.8	0.9
3	1	3	5.03	5.41	7.0	0.4
5	5	3	5.03	5.46	7.9	0.5
3	0	6	5.05	5.42	6.9	0.2
5	4	6	5.03	5.50	8.5	1.3

Table 6.2: The predicted and measured values of z -directed magnetic field density at each of the sensor locations with both windings energized. The measured values have been averaged over 20 periods. The field strength at the center of the test chamber is 5.43 mT/A. Both windings have been excited with 1 A peak amplitude 30 Hz currents, with the phase relationship shown in Fig. 6-8.

6.4 Magnetic Field Diffusion

It was hypothesized, based on the skin depth of copper, that attenuation of the magnetic field strength might be considerable at operating frequencies above a few Hertz. Using the set-up already described, measurements were taken at six different frequencies. The fluxball machine was operated with the inner winding open circuited and the outer winding energized with the maximum voltage available using the normal mode of operation. The current in the outer winding was measured and the expected magnetic field at DC, B_{DC} , was calculated for the location of the sensor.

The attenuation of the signal could then be measured by looking at the peak magnitudes of the measured AC magnetic fields. Because the outer winding was energized, the uniform field was in the x direction. Therefore, B_x was compared with B_{DC} , and the attenuation due to diffusion was calculated. Distortion of the signal could be seen by graphing a single period of the magnetic field waveform. A small part of the distortion resulted from the response time in the Hall effect sensor. Fig. 6-9 shows the results of the skin effect measurements.

6.5 Magnetic Field with a Sphere of Ferrofluid

A final experiment was conducted to measure the change in inductance of the fluxball when a sphere of ferrofluid was placed inside the test chamber. In this configuration there are three magnetic field regions. The derivation for the fields in this situation can be found in the doctoral thesis of Shihab Elborai [12]. Modeling the ferrofluid as a linear, magnetizable material and applying the constant flux condition, a new inductance, L_a , can be derived. L_a is given by eq. 6.1:

$$L_a = L_0 \left[1 + \frac{2r_a^3}{r_w^3} \left(\frac{\mu_a - \mu_0}{2\mu_0 + \mu_a} \right) \right] \text{ H}, \quad (6.1)$$

where L_0 is the measured self-inductance of the winding at 1 kHz given in Table 6.3, r_a is the radius of the sphere of ferrofluid, r_w is the average radius of inner or outer winding, given in Table 3.2, μ_a is the magnetic permeability of the ferrofluid, and μ_0 is the magnetic permeability of free space.

L_a was measured with a 4 cm diameter sphere, $r_a = 2$ cm, filled with MSG W11

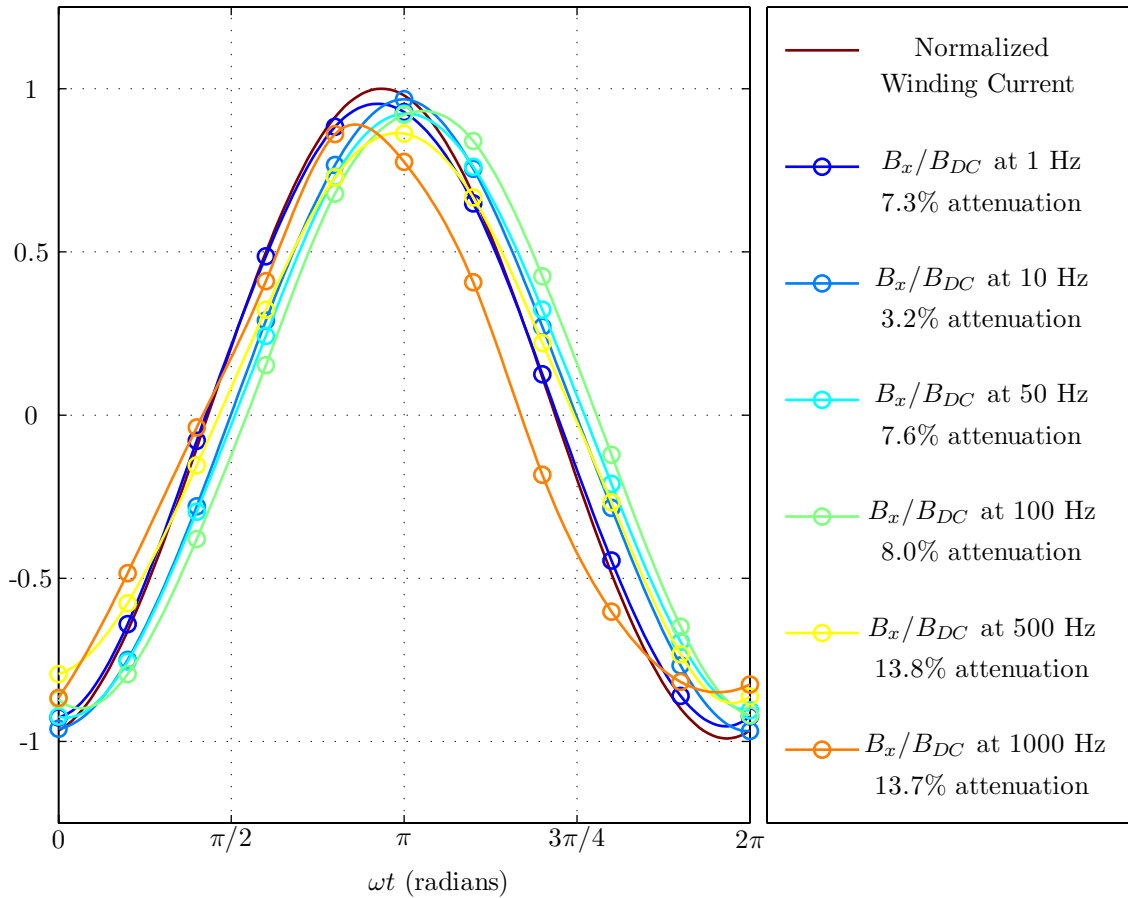


Figure 6-9: The distortion and attenuation of the x -directed magnetic field in the test chamber, B_x , produced by the outer winding at six different operating frequencies between 1–1000 Hz. B_x is normalized by the DC magnetic field, B_{DC} , that would be produced by the same current.

Winding	Initial Value L_0	Predicted Value L_{a_p}	Measured Value L_{a_m}
Inner	171.0 mH	174.9 mH	176.0 mH
Outer	559.7 mH	563.6 mH	561.4 mH

Table 6.3: The predicted, L_{a_p} , and measured, L_{a_m} , values of inductance for each fluxball winding with a 4 cm radius sphere of MSG W11 ferrofluid at the center of the fluxball machine. L_{a_p} was based on an initial winding inductance, L_0 , that was measured for each winding without the sphere of ferrofluid inside the test chamber. All inductances were measured at 1 kHz using a Hewlett-Packard 4192A LF Impedance Analyzer.

ferrofluid, manufactured by Ferrotec Corporation [44], placed in the middle of the fluxball machine. MSG W11 has $\mu_a = 1.56\mu_0$ H/m. Table 6.3 lists the measured and predicted values of the new inductance L_a for both of the fluxball windings.

As predicted the inductance of the windings increased. However, there were significant sources of error in both the prediction and the measurement. First of all the magnetic permeability of the ferrofluid was not verified before it was placed into the 4 cm sphere. The permeability measurement dated back at least two years, during which time there has most likely been degradation of the ferrofluid's magnetic susceptibility. Additionally, the measurement for the inner winding was somewhat unstable using the Hewlett-Packard 4192A LF Impedance Analyzer. The displayed value varied with every update between 173 and 178 mH.

Chapter 7

Conclusions

7.1 Fluxball Machine

7.1.1 Error

This section describes the numerous sources for error in the measurement of the uniformity of the magnetic fields. These sources of error were carefully considered and steps were taken to minimize their effects. Nevertheless, significant error remained in some of the measurements.

Appendix C described how the construction process was controlled to minimize error. Once construction was complete, the geometric dimensions of the fluxball windings were carefully measured. The turns were wrapped with care by the author of this report. The process was very manual, and therefore susceptible to human error. Certainly a few extra turns were wrapped in a few of the slots, but the cumulative error in the turns per fluxball winding did not exceed 25 turns, 2% of the total turns.

All numerical predictions were based on the geometry of the fluxball machine as built. Complete elliptical integrals were solved numerically using double precision numbers to give the highest degree of accuracy to the numerical calculations.

The calibration of the measurement devices was described in detail in Chapter 5. Multiple sensors were used in the both the AC and DC modes to verify the strength of the magnetic fields. These sensors gave very good agreement regarding the strength of the field

in the inner region of the fluxball machine.

The data processing was very involved for the set of experiments described in this thesis. The use of many sensors, in different locations, at different operating frequencies and field amplitudes, made each calculation a little different from the previous. Data was continually plotted graphically in order to ensure that signals were not being corrupted by noise or other sources of error. Additional calculations were made whenever possible to serve as “reality checks” on the processed data.

The main error that is obvious in the work described in this thesis is the difference in magnitude of the predicted and the measured magnetic field densities. There is no real mechanism for error in the prediction, and the measurement process was controlled so that error should be less than 1%. Problems in the construction process can only account for another 1–2% percent of the error.

The remaining error is mostly likely caused by reflected fields from the steel table upon which the machine was sitting. The table is made of a large sheet of stainless steel with non-zero conductivity and magnetic permeability. This table can be modeled as a plane of infinite magnetic permeability, and the reflected fields can be calculated using the method of images. This was done using the geometry of fluxball machine, with the origin of the machine 21 cm above the table. The resulting predicted fields were 5% stronger than the fields predicted when neglecting the image currents. Next the inner winding of the machine was lifted so that its origin was 56 cm off the table and a measurement of the DC field was taken with the winding excited by 1 A of current. The measured magnetic field was $\approx 2\%$ weaker.

Despite the error in the magnitude of the magnetic fields, the uniformity of the fields was very close to the predicted values, and well within the tolerance of the known error. The values, for magnetic field strength, operating voltages, etc. . . , given in this thesis reflect the measured magnetic field densities.

7.1.2 Mathematical Model

The actual geometry of the fluxball machine is quite complex. To develop analytical solutions for experiments that use the fluxball machine, it would be convenient to have a simpler

mathematical model. The model described in Chapter 2 is very convenient since it only requires 3 variables: the total number of turns on the ball, the radius of the winding, and the current, i , in the winding. The proper radius, R_m , is the average radius of the winding and quadrature axis. The proper number of turns, N_m , should be the calculated turns required to produce the fields measured in Chapter 6. Eq. 7.1 gives the mathematical model for the fluxball machine; the parameter values are listed in Table 7.1. Obviously, the coordinates of one of the windings must be changed if the windings are oriented orthogonally.

$$\mathbf{K} = \mathbf{i}_\phi \frac{N_m}{2R_m} i \sin \theta \quad (7.1)$$

Using this model, the magnetic fields, as shown in Chapter 2, are given by eqs. 7.3 and 7.2.

Characteristic	Inner Fluxball	Outer Fluxball
Interior \mathbf{B} -field	5.43 mT/A	5.43 mT/A
Radius, R_m	10.7 cm	15.9 cm
Turns, N_m	1392	2069

Table 7.1: Parameters for the mathematical model of the fluxball machine.

$$\mathbf{B} = \frac{\mu_0 N_m i}{3R_m} (\mathbf{i}_r \cos \theta - \mathbf{i}_\theta \sin \theta) = \frac{\mu_0 N_m i}{3R_m} \mathbf{i}_z \quad r < R \quad (7.2)$$

$$\mathbf{B} = \frac{\mu_0 N_m i}{6R_m} (R_m/r)^3 (\mathbf{i}_r 2 \cos \theta + \mathbf{i}_\theta \sin \theta) \quad r > R_m \quad (7.3)$$

7.2 Future Ferrofluid Experiments

The fluxball machine can be used to conduct a large variety of experiments involving ferrofluids. Because of the spherical geometry of the current distribution, it is convenient to work with spherical volumes of ferrofluids. An experimental set-up for working with a sphere of ferrofluid has been established. An 8 cm diameter plastic ball was filled with ferrofluid using a syringe. This sphere was then placed at the center of the test chamber using a funnel that was fitted to the bottom access tube of the inner fluxball structure. GMW sensors were placed in the interior and exterior regions of the fluxball machine in order to measure the changes to both the uniform field region and the point magnetic dipole field

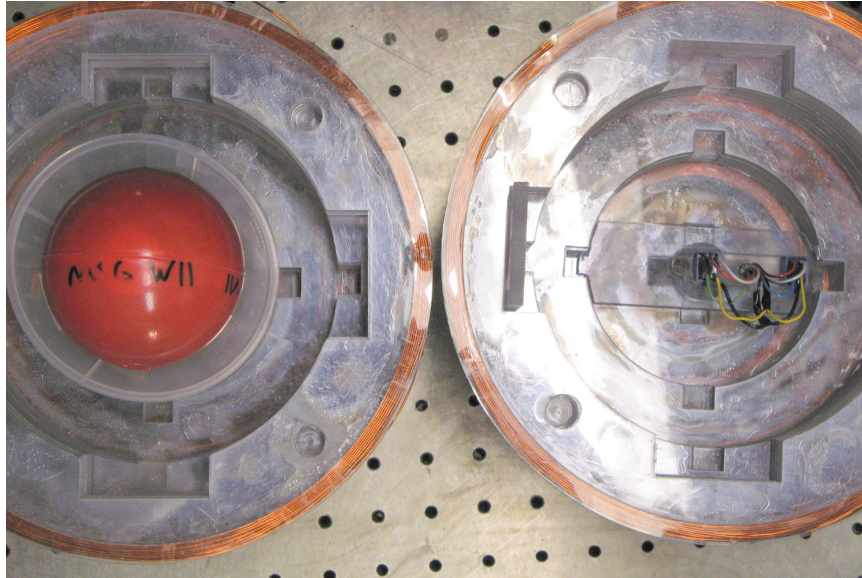


Figure 7-1: A top view of the inner fluxball winding with the sphere of ferrofluid positioned at the center of the fluxball machine. The sphere of ferrofluid is held by a funnel that is fitted to the bottom access tube. The funnel may be adjusted to hold spheres with different diameters. The GMW sensors can be seen shimmed to the top of the test chamber, seen on the hemisphere to the right.

region. This set-up can be seen in Figs. 7-1 and 7-2.

In addition to measuring changes in the magnetic fields that result from the addition of ferrofluids to the machine, future fluid dynamical measurements could be made with the fluxball machine. As described in Chapter 3, ultrasound velocimetry experiments could be conducted inside the test chamber of the machine by running the ultrasound probes through the machine's cable-ways. These experiments would verify and build on the results presented by Shihab Elborai and Xiaowei He [12, 13]

7.3 Future Machinery Experiments

The demand for electrical power and speed has driven military and commercial shipbuilders to move towards ever larger electric machines. The U.S. Navy has recently embarked on the contract design of a new class of destroyers that will feature a fully integrated electric propulsion system; an artist rendering of this ship can be seen in Fig. 7-3. This systems is

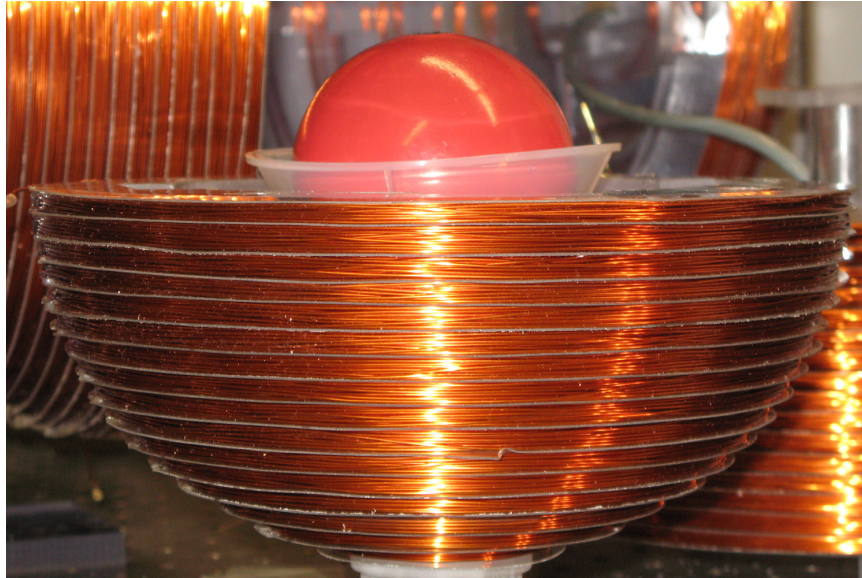


Figure 7-2: A side view of the inner fluxball winding with the sphere of ferrofluid positioned at the center of the fluxball machine.

composed of four gas turbine engines that provide electrical power for two 34.6 MW electric motors, as well as all ship service electrical requirements [45]. The two large electric motors will be operated in machinery rooms where personnel will be exposed to alternating and rotating magnetic fields. While the medical community has studied the effects of electric and magnetic fields on the human body, there is still not a consensus on the effects of low and mid level magnitude fields in the low frequency range [46–50]. These are exactly the types of fields to which shipboard personnel will be exposed. The fluxball machine could be used to conduct a variety of experiments related to the biological effects of these types of fields.

A second set of experiments that could be conducted using the fluxball machine involve podded propulsors, such as the one show in Fig. 7-4. These pods contain large electric motors that radiate very specific electromagnetic fields. While most of these fields are confined to the ferrous elements of the motors, a portion of the fields radiate. These fields are further attenuated by the enclosures that support them, which are usually made of steel. Nevertheless, low-level fields passing through the propulsor enclosures are present and could be used to detect and classify particular ships. The fluxball machine could be used to model

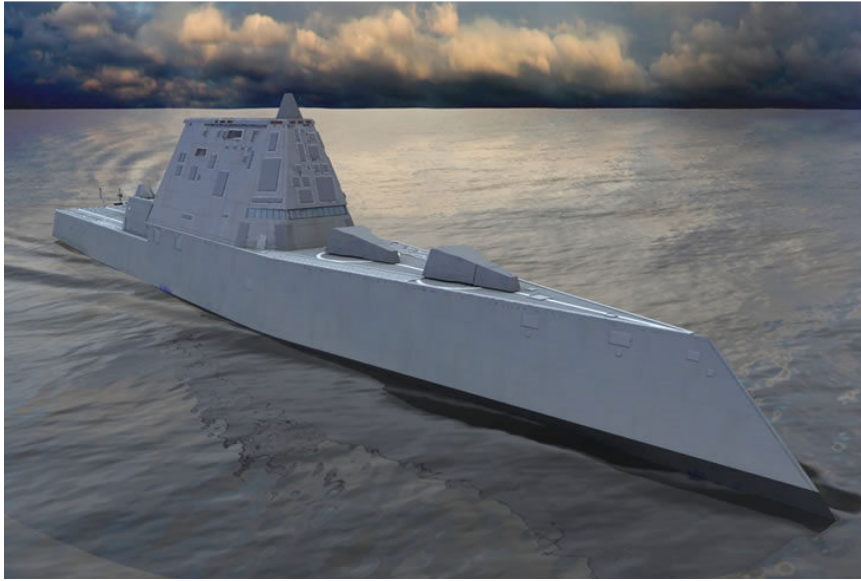


Figure 7-3: An artist's rendering of the next generation destroyer. This ship will have two 34.6 MW electric motors [45].

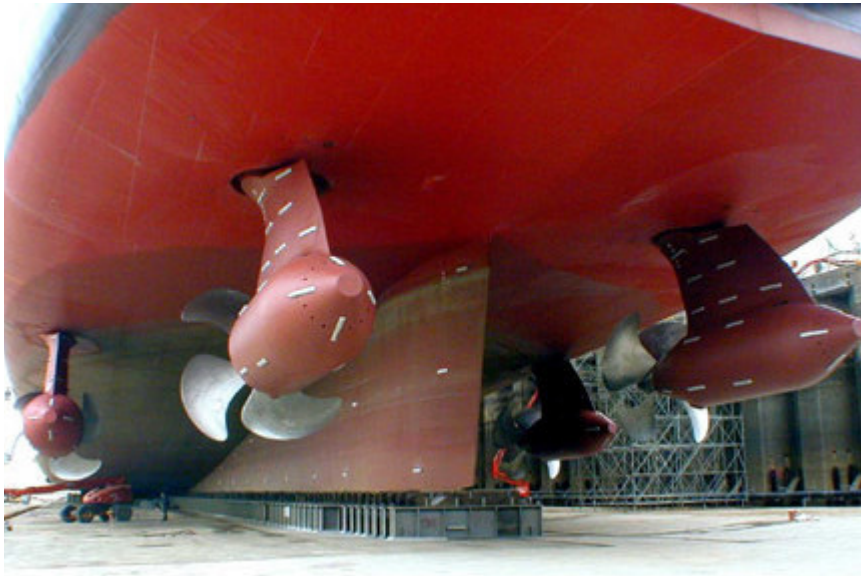


Figure 7-4: The podded propulsors installed on the Queen Mary 2. These are Rolls-Royce MermaidTM pods that contain 21.5 MW Alstom electric motors [51].

the flux leakage from large electric motors and to test the efficacy of propulsor enclosures in containing radiated magnetic fields.

Appendix A

Fluxball — A Design History

A.1 John W. Clark's Fluxball

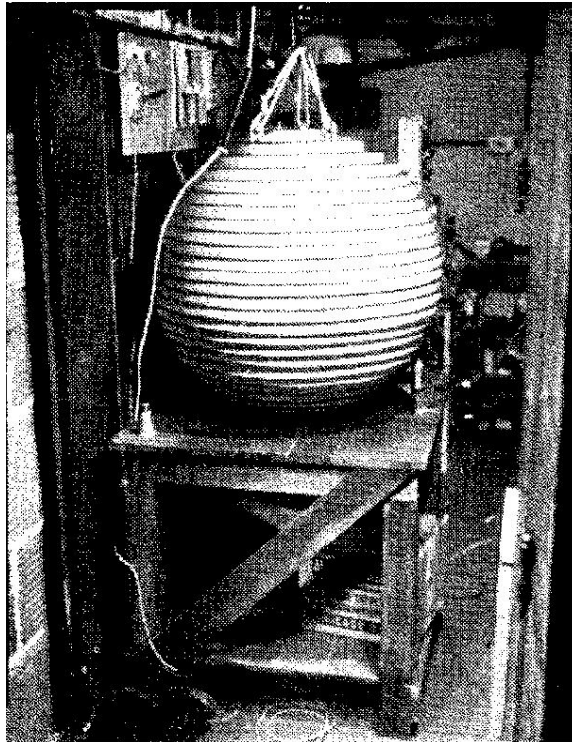


Figure A-1: A spherical magnet designed by John W. Clark in 1938 for producing uniform magnetic fields used for nuclear research [3].



Figure A-2: A fluxball of Clark's design is still operated by the Physics Department at the Massachusetts Institute of Technology.

A.2 John A. Hipple Jr.'s Fluxball

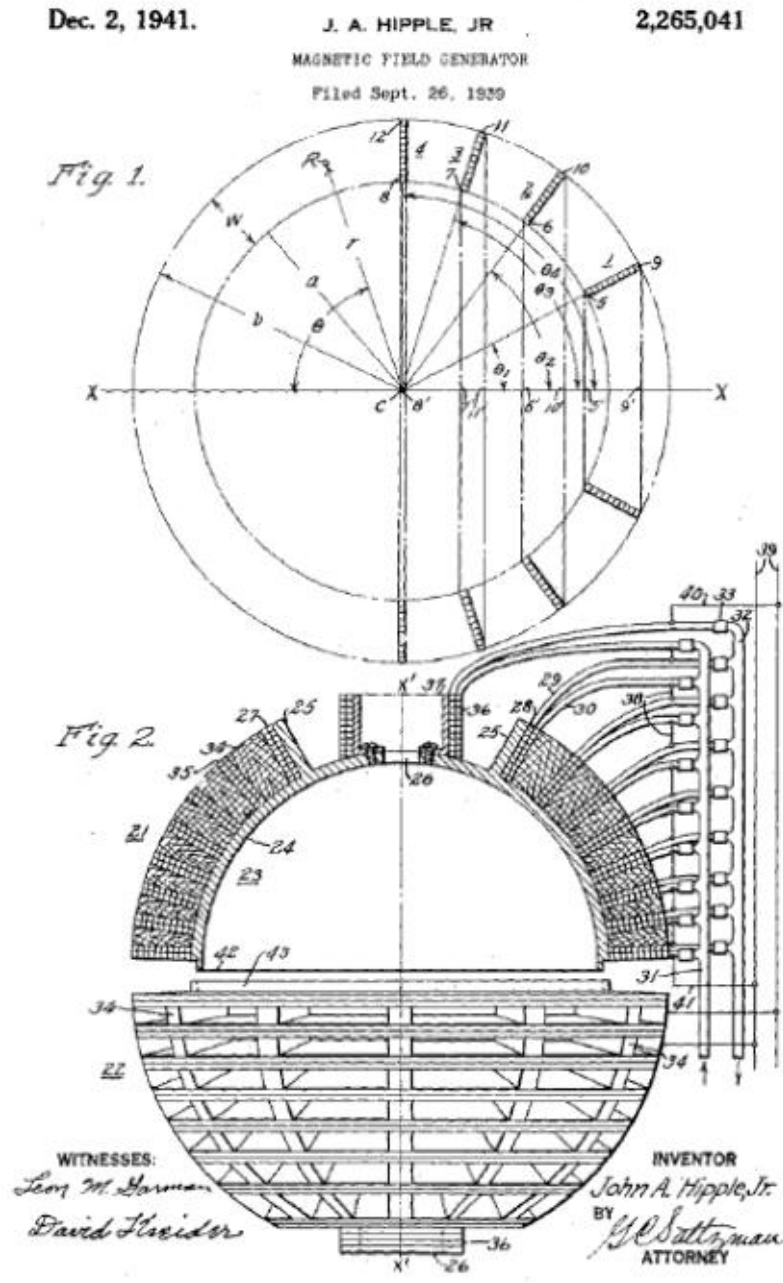


Figure A-3: Spherical winding drawing by John A. Hipple Jr. from his 1941 United States Patent for a *Magnetic Field Generator* [7].

A.3 William F. Brown and John H. Sweers' Fluxball

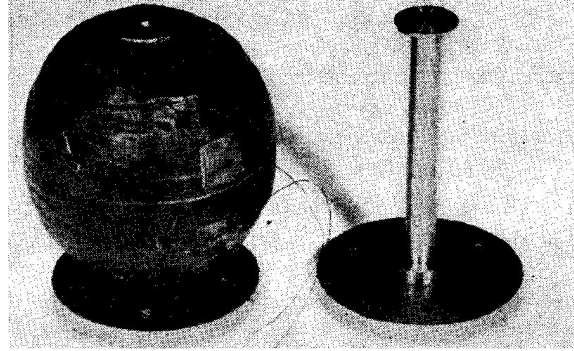


Figure A-4: A 1945 fluxball test coil for point magnetic field measurements, as constructed [4].

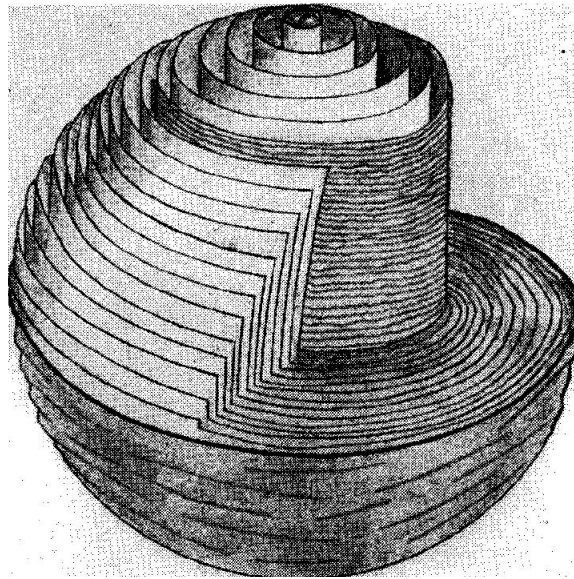


Figure A-5: A 1945 fluxball test coil for point magnetic field measurements, in cross section [4].

A.4 J.E. Everett and J.E. Osemeikhians' Fluxball

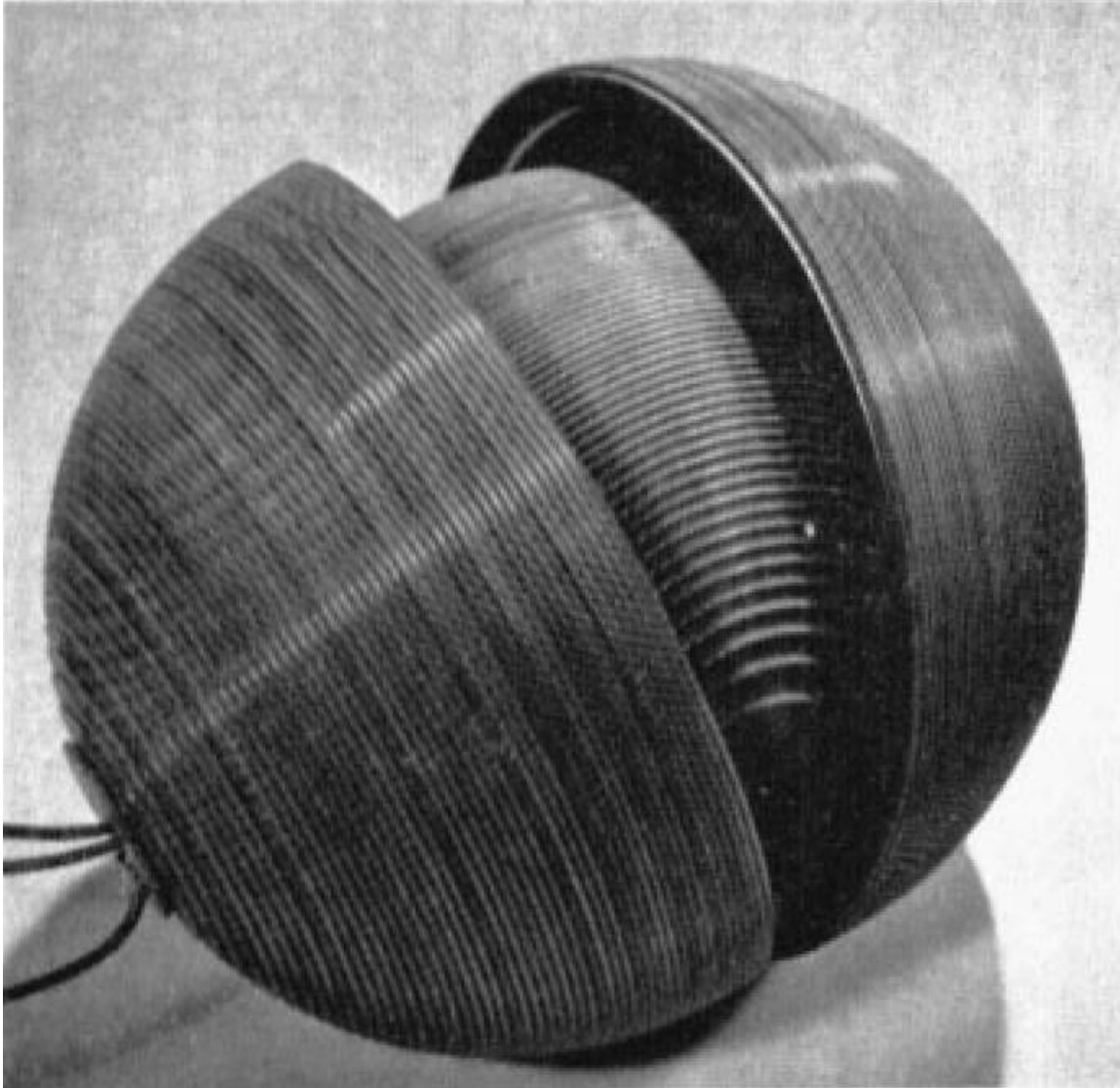


Figure A-6: A 1966 three axis fluxball arrangement used to build a proton magnetometer [5].

A.5 F. Primdahl and P Jensens' Fluxball

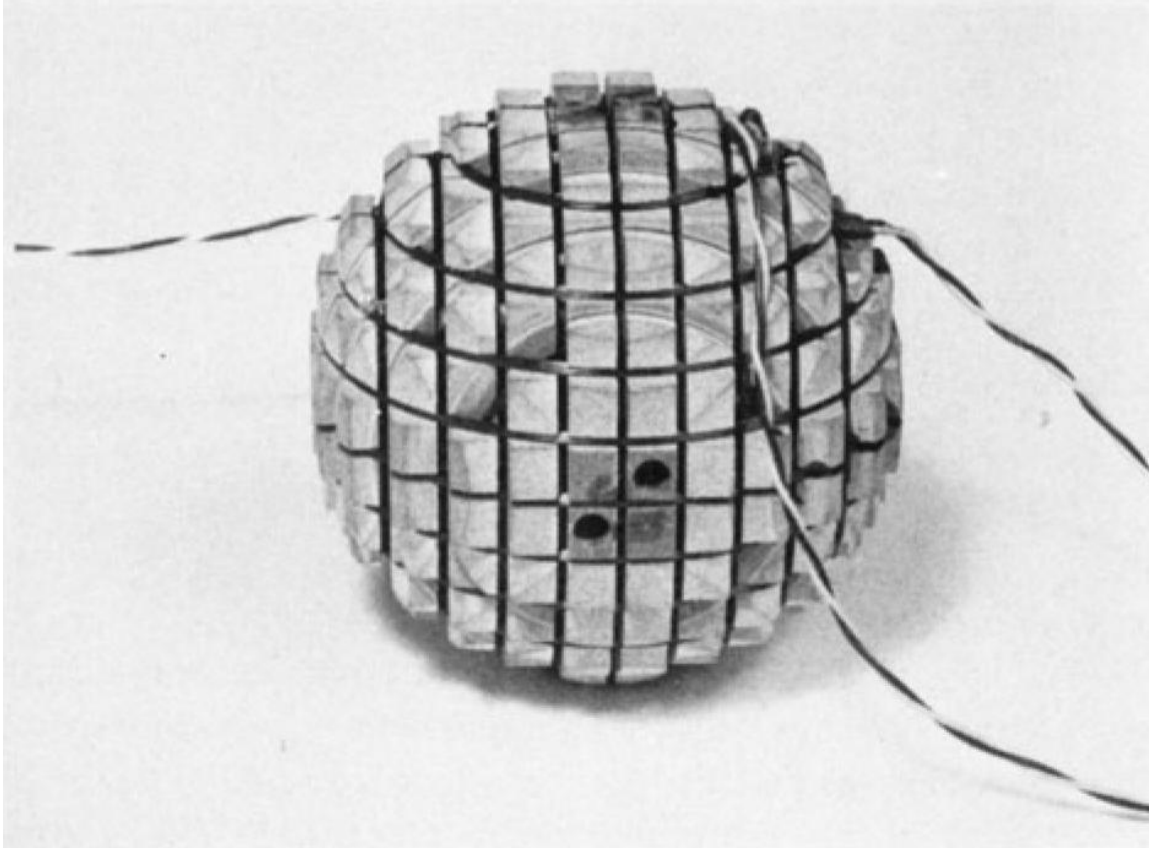


Figure A-7: A 1981 three axis fluxball arrangement for fluxgate magnetometer vector feedback [6].

Appendix B

Computer Design Tools

B.1 MATLAB[®]

This section contains useful pieces of commented code that were used to aid in the construction and analysis of the fluxball machine.

B.1.1 Magnetic Fields Generated by a Loop of Current

```
% Script Name: current_loop.m
% Author: Clint Lawler
% Date: 19 APR 2007
% This function calculates the magnetic field at a point (rp,zp) in
% cylindrical coordinates due to a loop of current with magnitude i_wire
% with radius r_wire that is centered at z_wire. J1 and J2 are the first
% and second elliptical integrals of Legendre
%
function [Br Bz] = current_loop(rp,zp,i_wire,r_wire,z_wire)
%
mu=pi*4e-7; z = zp-z_wire; p = abs(rp); a = r_wire;
%
if p == 0
    Br = 0;
    [J1 J2] = ellipke(0);
    Bz = ellipke(0)*(1+(a^2-z^2)/(a^2+z^2))*mu*i_wire/(2*pi*(a^2+z^2)^0.5);
    return
end
%
```

```

k=sqrt(4*a*p/((a+p)^2+z^2)); const = mu*i_wire*k/(4*pi*sqrt(a*p));
[J1 J2] = ellipke(k^2);
if z == 0
    Br = 0;
else
    Br = (rp/p)*const*(z/p)*(-J1+J2*(a^2+p^2+z^2)/((a-p)^2+z^2));
end
Bz = const*(J1+J2*(a^2-p^2-z^2)/((a-p)^2+z^2));
%
```

B.1.2 Magnetic Fields by the Superposition of Current Loops

```

% Script Name: Magnet.m
% Author: Clint Lawler
% Date: 25APR2007
% Description: This script takes a winding geometry and current
% distribution, and then it calculates the magnetic field at specified
% positions and draws the magnetic field lines. If has an option to show
% the uniformity of the fields. The numbers specified here are for a
% Helmholtz coil. This routine is for air-cored, axially symmetric coils.
% The function current_loop is required.
%
percent_uniform = 1;
axes; hold on; grid off
rho=1.724e-8; %Resistivity of Copper at 20 deg C
a_wire = pi*(0.00082/2)^2; %20 AWG wire
i_wire = [1 1]; % Current distribution (A)
r_wire = [1 1]; % Radius of loops (m)
z_wire = [0.5 -0.5]; % Height of loops (m)
N=length(i_wire); max_r = max(r_wire); pts = 128; nr=pts;
r_end=max_r; dr=r_end/(nr-1); r=0:dr:r_end; nz=pts; z_end=max_r;
dz=z_end/(nz-1); z=0:dz:z_end; B=zeros(nr,nz,2);
%This uses the Biot-Savart Law to calculate the magnetic field
%from the superposition of each hoop of line current.
for i_r=1:nr
    for i_z=1:nz
        for n=1:N
            [Br Bz]=current_loop(r(i_r),z(i_z),...
                i_wire(n),r_wire(n),z_wire(n));
            B(i_r,i_z,1)=B(i_r,i_z,1)+Br;
            B(i_r,i_z,2)=B(i_r,i_z,2)+Bz;
            Br = 0;
            Bz = 0;
        end
    end
end
```

```

        end
    end
end
%Calculate resistance for the specified magnet
Length_winding = 2*pi*sum(r_wire);
R_winding=rho*Length_winding/a_wire;
% Plot the Field Lines - this assumes symmetry around x and z axis
sr_end=max_r; ds=sr_end/8; SR=0:ds:sr_end; SZ=zeros(size(SR));
h_stream(1,:) = streamline(r,z,B(:,:,1)',B(:,:,2)',SR,SZ);
h_stream(2,:) = streamline(r,-z,B(:,:,1)',-B(:,:,2)',SR,SZ);
h_stream(3,:) = streamline(-r,z,-B(:,:,1)',B(:,:,2)',-SR,SZ);
h_stream(4,:) = streamline(-r,-z,-B(:,:,1)',-B(:,:,2)',-SR,SZ);
axis([-max_r max_r -max_r max_r]) colormap('pink')
Error=abs((B(:,:,2)-B(1,1,2))/B(1,1,2));
Error(nr,nz)=percent_uniform*1e-2;% Max deviation at 1 percent
Error(Error>Error(nr,nz))= Error(nr,nz);
[X,Z] = meshgrid(r,z);
h_pcolor(1) = pcolor(X,Z,Error);
h_pcolor(2) = pcolor(-X,Z,Error);
h_pcolor(3) = pcolor(X,-Z,Error);
h_pcolor(4) = pcolor(-X,-Z,Error);
shading interp

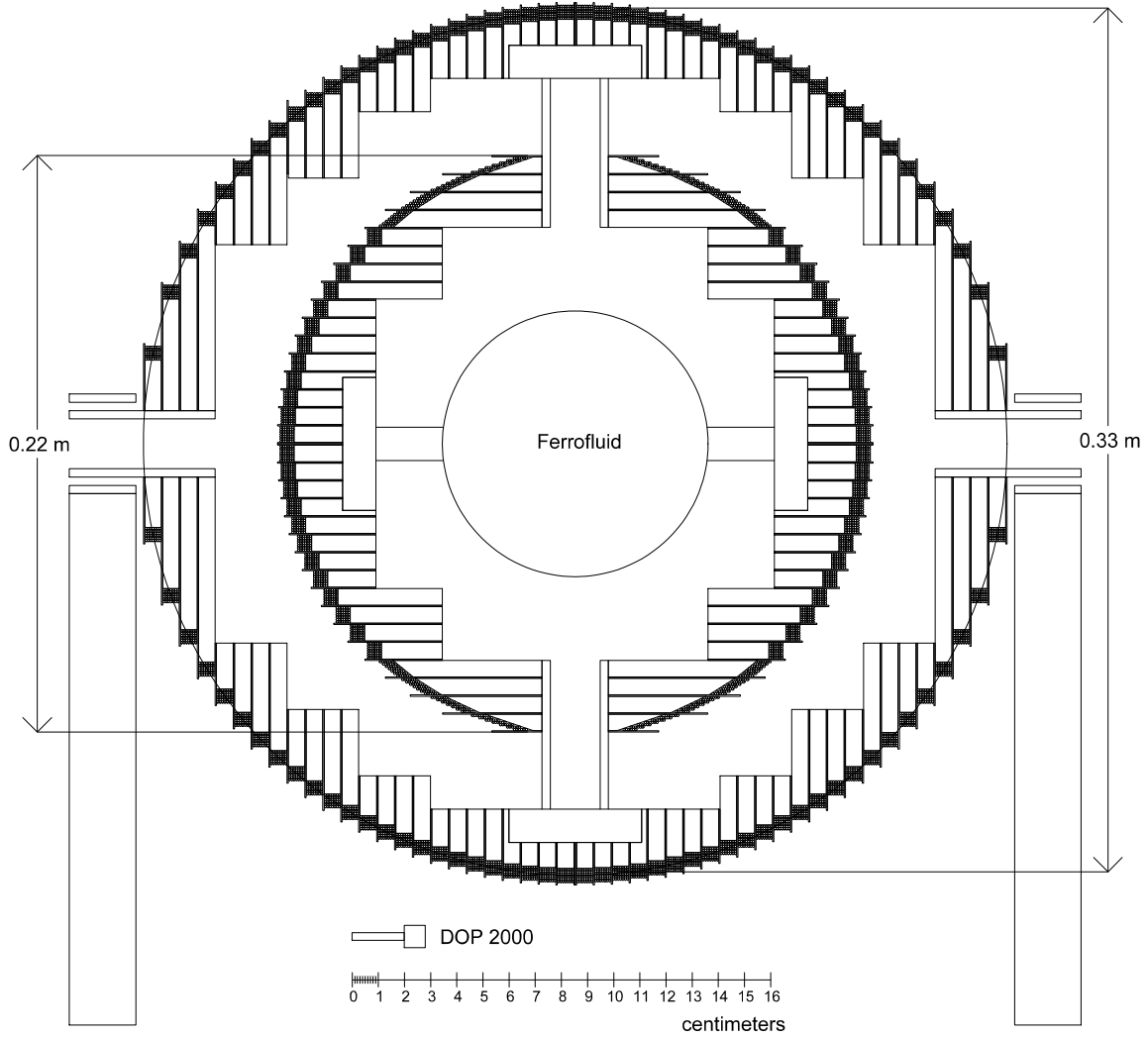
```

B.2 RHINOCEROS[®] 3.0 CAD/CAM

In addition to analyzing the magnetic field lines and uniformity, Matlab was used to write a text file that could be read into Rhinoceros and rendered. This was important because Rhinoceros was a much better tool for exploring geometry changes, and it was necessary in order to produce the type of file, .dfx, that could be used to by the waterjet machine software. Fig. B-1 shows a rendering of an intermediate design that was produced by Rhinoceros. Fig. B-2 show one of the flange layouts that was created using Rhinoceros.

B.3 OMAX[®] Layout and Make

OMAX Layout is a computer-aided machining (CAM) program that can be used to generate tool paths for OMAX Make, the software program that actually controls the waterjet cutter [52]. Layout was used to import the rhino generated disc patterns and then to generate tool paths.



Operating Parameters	
B Field:	243 Gauss
Current:	5.0 Amps
Average Radius:	0.11 m
Total Turns:	1280
Power:	237 Watts

Operating Parameters	
B Field:	244 Gauss
Current:	5.0 Amps
Average Radius:	0.17 m
Total Turns:	1920
Power:	531 Watts

Figure B-1: A 2-D RHINO rendering of an intermediate fluxball machine design.

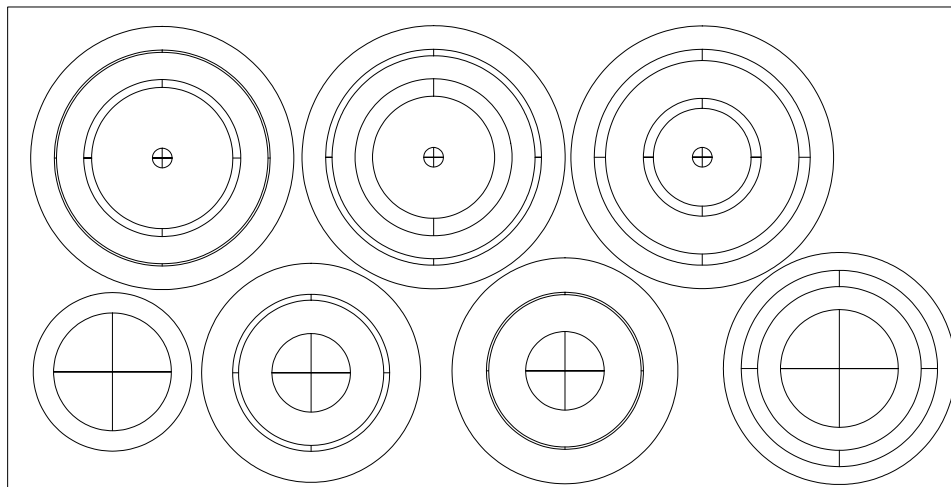


Figure B-2: An example of the layout patterns done in RHINO for machining. This is one of three 48 x 24 in sheets that was arranged with flanges. The alignment details were added later.

Appendix C

Fluxball Construction

C.1 Fabrication of Parts

Nearly all of parts for the fluxball machine were fabricated in the MIT hobby shop using the OMAX 2626 waterjet cutter, shown in Fig. C-1. 80 discs were cut from 0.25 in polycarbonate sheet. 82 flanges were cut from 0.07 in polycarbonate film. For both discs and flanges, two sheets were stacked and cut together to save time. One mistake that was made in this process was the calculation of the disc diameters. The calculation was made before the actual material was received and measured. The small error in the actual thickness was small enough that the calculations and processing of the model did not need to be redone, but it was still significant.

In addition to the discs and flanges, a number of smaller connectors had to be built. Fig. C-2 shows the two main designs that were employed. The circular pieces held the top flanges on securely and created a part that could be removed, by simply removing four screws, in order to change the configuration. The square pieces were used to align the two hemispheres and to hold the two fluxball structures together. Additionally the square pieces could be used to construct interchangeable set-ups inside the test chamber.



Figure C-1: The Omax 2626 Waterjet cutting machine, maintained by the MIT Hobby Shop, that was used to fabricate the parts for the fluxball machine.

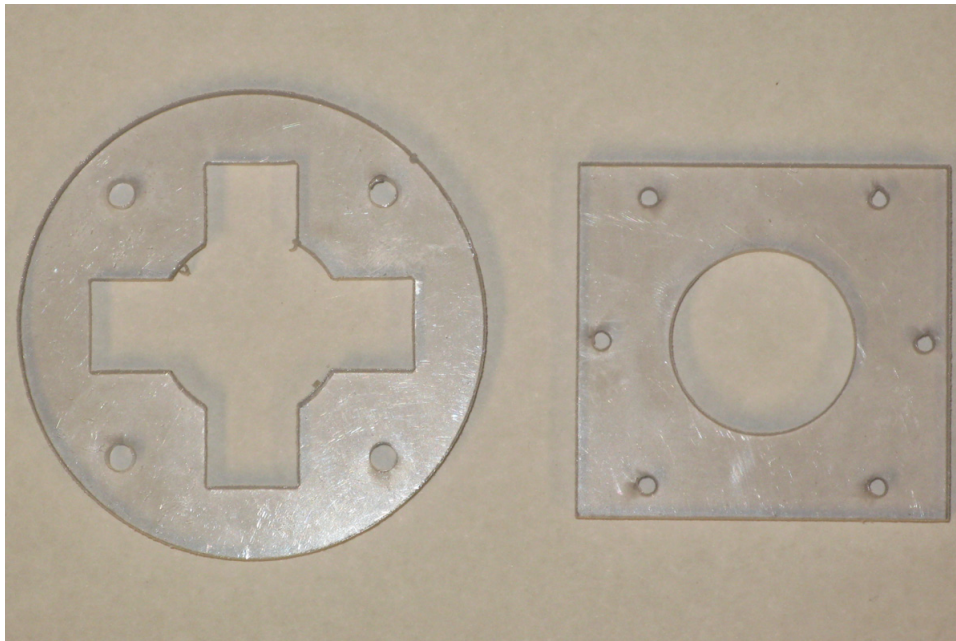


Figure C-2: Two parts that were created for alignment and connection of the fluxball structures.



Figure C-3: The fixture that was made and used for alignment of the discs and flanges.

C.2 Assembly and Bonding

Notches had been cut into the inner radii of all of the discs and flanges to aid in the assembly. Nevertheless, a complex fixture had to be built in order to ensure proper alignment of the individual parts. Figs. C-3 and C-4 show these fixtures. This method is not recommended. A better method would be to cut two alignment holes in each disc. Then a plastic rod could be inserted and either bonded or mechanically fastened until the until the bonding step was completed. These alignment holes would have to be staggered, but this design could easily be completed using 3-D computer modeling tools.

The waterjet machine leaves a lot of sediment on the parts, so before the parts could be assembled, they needed a thorough cleaning. All of the discs were washed with soapy water and then dried. Before final assembly the discs were wiped down with isopropyl alcohol.

Using the alignment fixtures the discs and flanges were stacked one by one. Acrylic cement was dropped on the surface of the highest part on the stack and then the next part was laid down. This was done until the entire hemisphere was bonded, then a weight was put atop the stack and the hemisphere was left for a day to cure. The bonding procedure



Figure C-4: The alignment fixtures stacked with discs and flanges.

was done in a hood because of the large amounts of acrylic cement that were used.

This procedure left small gaps between some of the flanges and discs where the cement didn't make it to the edge, therefore a second round of bonding was conducted. This time the hemisphere was turned on its side and a small bead of cement was run down the crack between each disc and flange. The cement filled in the gaps quite nicely. Figs. C-5 and C-6 show the final, bonded fluxball structures.



Figure C-5: The inner fluxball structure after both bonding procedures were completed.

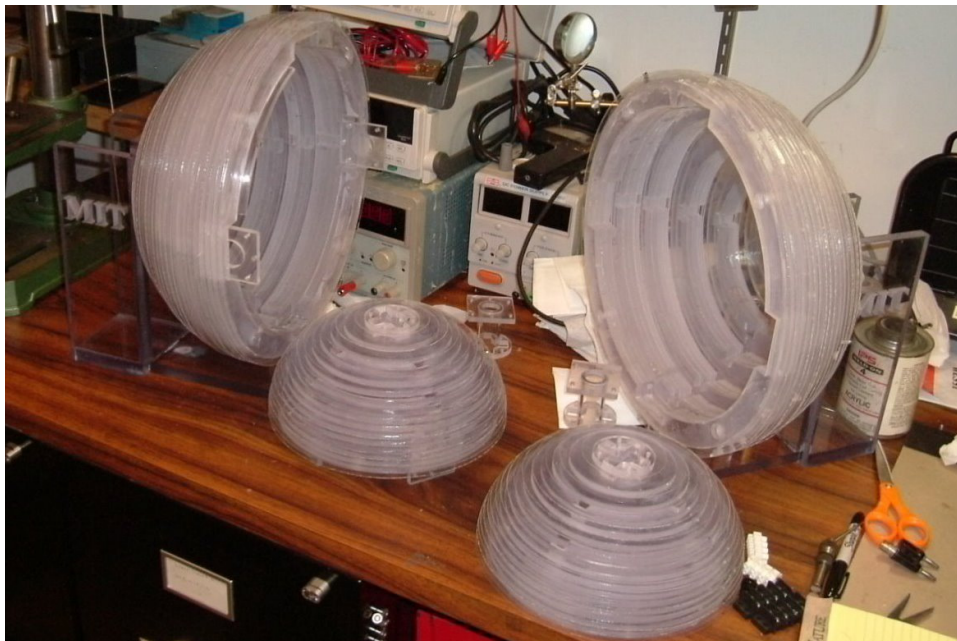


Figure C-6: The fluxball structures just prior to winding of coils.

C.3 Winding the Coils

A number of methods were experimented with for winding the fluxballs. The best method was a lathe assisted method. A plastic rod with an outer diameter of $3/4$ in was inserted into the bits of the lathe. Next the fluxball structure, with a $3/4$ in inner diameter access tube was fitted onto the smaller rod. Finally a spool of wire was secured parallel to the axis of the sphere so that it could payout easily into the slots of the fluxball. The lathe was turned at its slowest speed and the loose coupling between the rod and the access tube turned the hemisphere. The hemisphere could be stopped from turning just by holding it tightly. In this case the rod would continue spinning, while the hemisphere stood still. This method increased both the speed and the safety of the operation significantly. The author was then able to man the spool, ensuring that the correct number of turns were going into each slot and that the wire was laying nicely and tightly. The diameter of the large fluxball ball exceeded the height of the lathe bed, so a similar process was used by feeding the rod out the non bed side of the lathe bits. Figs. C-7 and C-8 show the set-up that was used for winding the coil onto the fluxball structures.

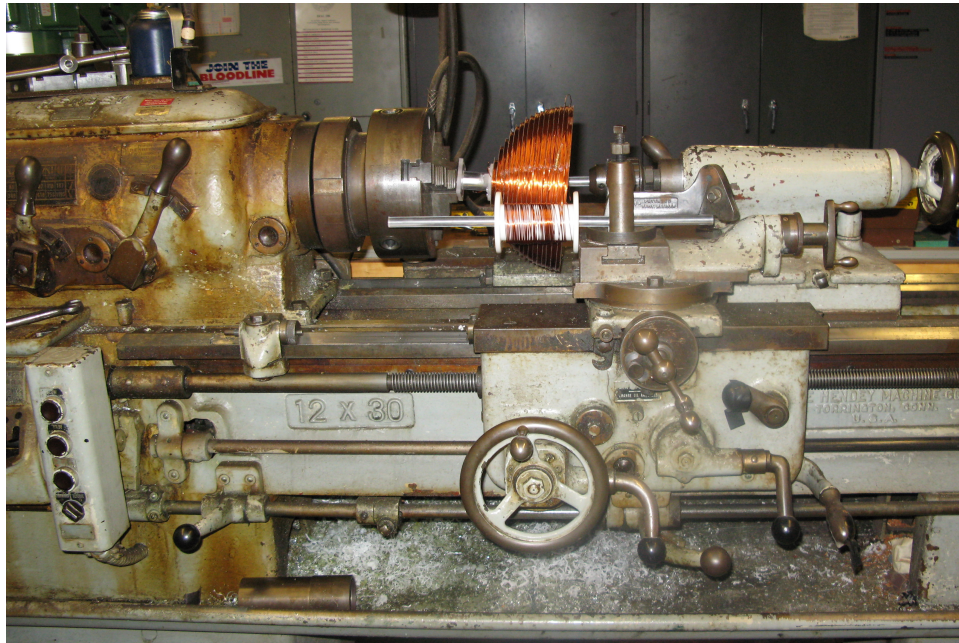


Figure C-7: The fluxball structure on the lathe as positioned for winding the coil around the structure.

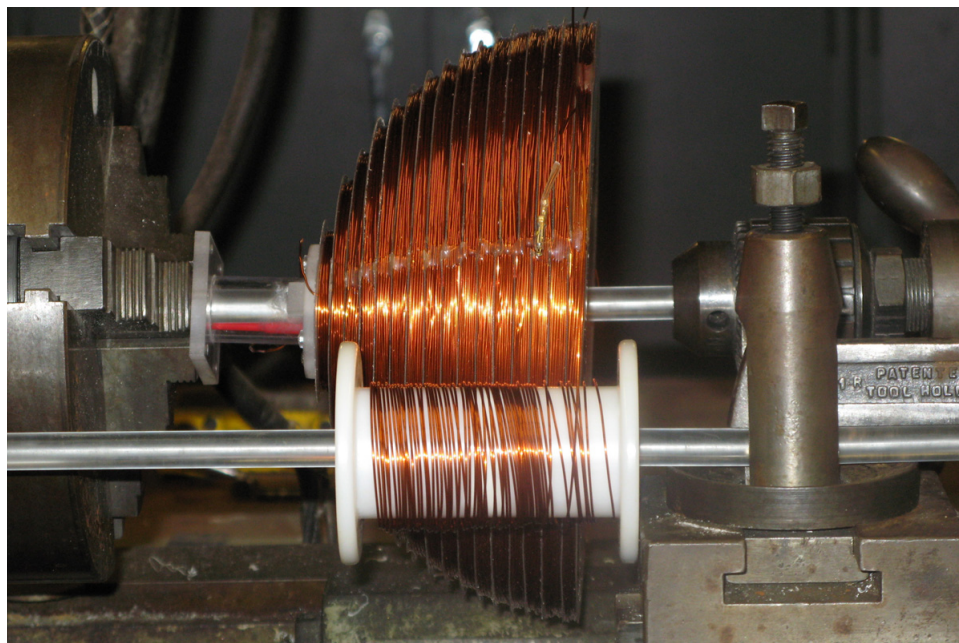


Figure C-8: A close-up view of the fluxball structure on the lathe as positioned for winding the coil around the structure.

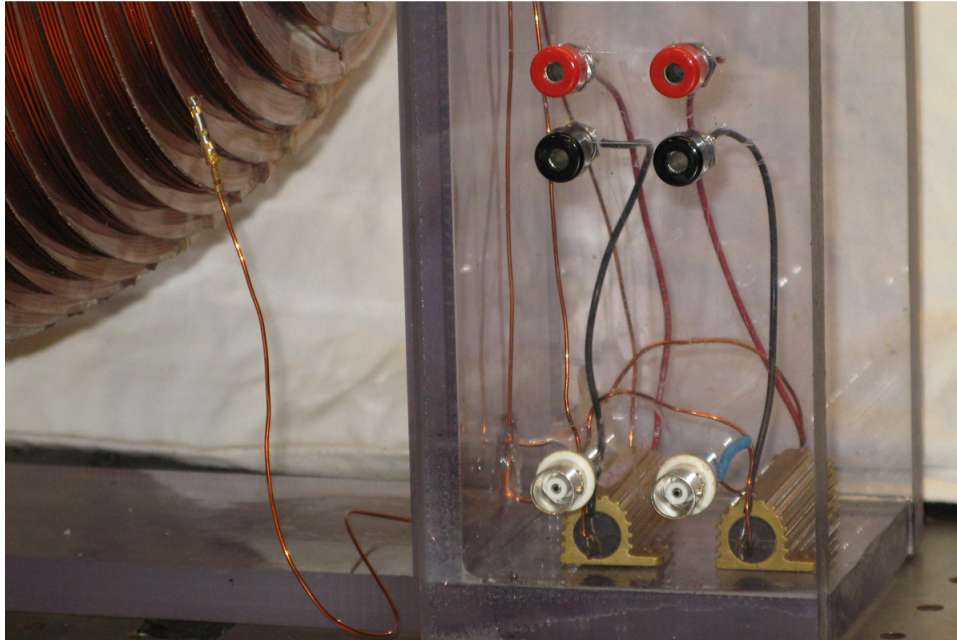


Figure C-9: The electrical connections on the support structure of the fluxball machine. There are BNC power connections for each of the fluxball windings and banana plug connections for reading the voltage over the $1\ \Omega$ current measurement resistors.

C.4 Electrical Connections

As the coil was being wound, solder connections were located approximately every 300 ft. Besides these connections, the hemisphere had to be connected to each other and the power sources needed to be connected to each of the windings. Inline male and female connectors were used to connect the hemispheres to one another. BNC terminals were placed in the left leg of the outer fluxball structure for connections to power sources. Additionally, banana jacks were soldered in parallel with the terminals of the $1\ \Omega$ current measurement resistors. All of these details can be seen in Fig. C-9.

C.5 Final Configuration

The final configuration is discussed in detail throughout this thesis. Figs. C-10–C-12 show various details of the fluxball machine.

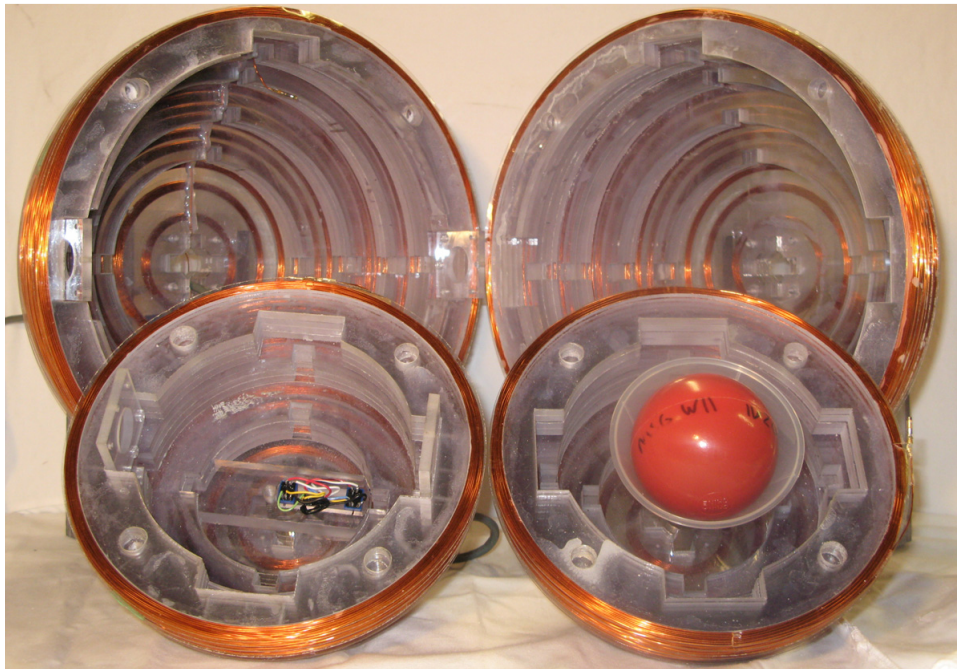


Figure C-10: An interior view of the four winding hemispheres.

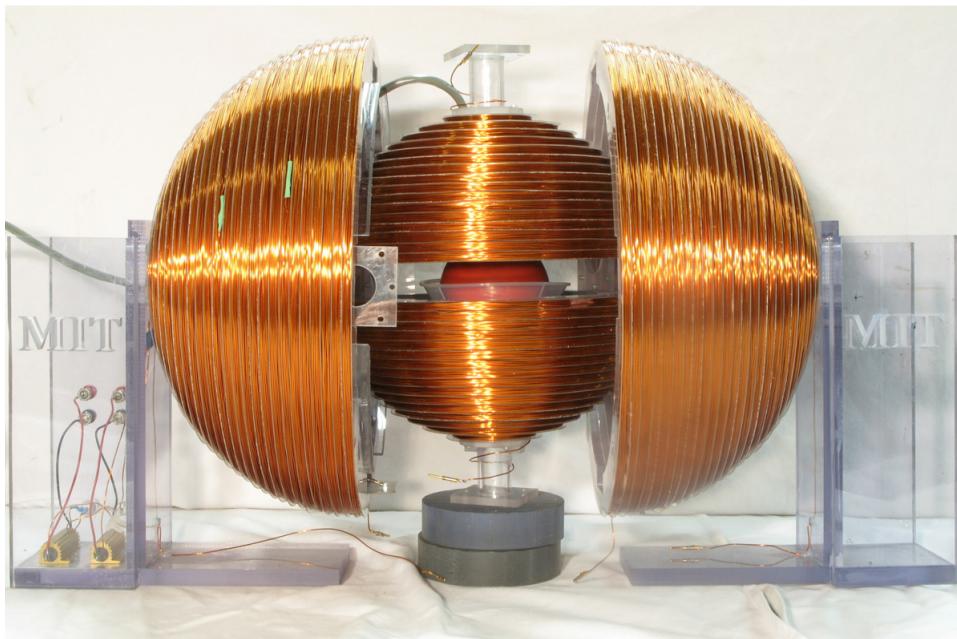


Figure C-11: An exploded front view of the fluxball machine.

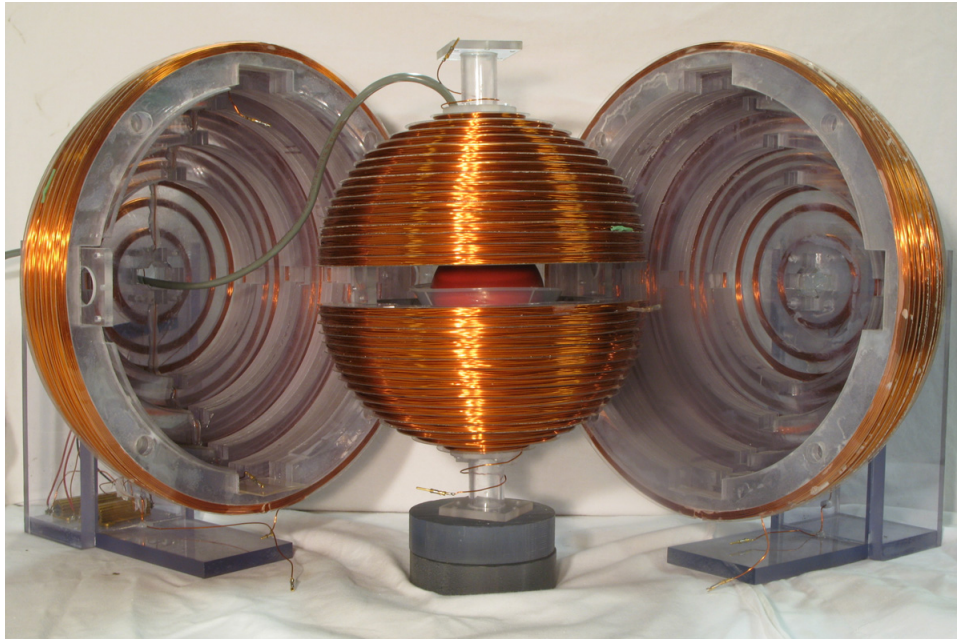


Figure C-12: The fluxball machine with the outer winding canted outwards.

Appendix D

Specifications

D.1 Fluxball Materials

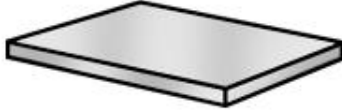
All of the materials for the fluxball machine were ordered from [McMaster-Carr](#).



Part Number: [7588K61](#)

\$49.30 per Spool

Type	Single-Conductor Wire and Cable
Single-Conductor Wire and Cable Type	Magnet Wire
Gauge (AWG)	20
Number of Conductors	1
Conductor Type	Solid
Conductor Material	Enamel-Coated Copper
Temperature Range	Up to +392° F (Up to +200° C)
Outer Diameter	.035"
Length	900'
Specifications Met	National Electrical Manufacturers Association (NEMA) and Underwriters Laboratories (UL)
NEMA Specification	1000 MW-35C and 1000 MW-73C
UL Specification	UL Recognized

Part Number: [8574K75](#)

\$177.31 Each

Material	Polycarbonate
Polycarbonate Material	Polycarbonate
Backing	Plain Back
Shape	Sheets, Bars, Strips, and Cubes
Sheets, Bars, Strips, and Cubes Type	Rectangular Sheet
Thickness	1/4"
Thickness Tolerance	+0 to -.026"
Length	8'
Length Tolerance	+.625"
Width	48"
Width Tolerance	+.625"
Clear	Clear with No Tint
Operating Temperature Range	-40° to +240° F
Performance Characteristic	High Impact Strength and Flame Retardant and Weather Resistant
Tensile Strength	9000 psi
Impact Strength	12 ft.-lbs./in.
Tolerance	Standard
Hardness	Rockwell R: 118
Specifications Met	Underwriters Laboratories (UL)
UL Rating	UL 972 and UL 94HB

Part Number: [85585K25](#)

\$12.18 Each

Material	Polycarbonate
Polycarbonate Material	Polycarbonate
Backing	Plain Back
Finish	Smooth on Both Sides
Shape	Film
Thickness	.02"
Thickness Tolerance	±.001"
Length	48-1/2"
Length Tolerance	±.063"
Width	24-1/2"
Width Tolerance	±.063"
Film Type	Standard
Clear	Clear with No Tint
Performance Characteristic	Flame Retardant
Tensile Strength	9000 psi
Impact Strength	12-16 ft.-lbs./in.
Tolerance	Standard
Specifications Met	Underwriters Laboratories (UL)
UL Rating	UL 94V2

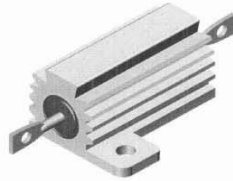
D.2 Series Resistor

RH, NH

Vishay Dale



Wirewound Resistors, Military, MIL-PRF-18546 Qualified, Type RE, Aluminum Housed, Chassis Mount



FEATURES

- Molded construction for total environmental protection
- Complete welded construction
- Meets applicable requirements of MIL-PRF-18546
- Available in non-inductive styles (type NH) with Aryton-Perry winding for lowest reactive components
- Mounts on chassis to utilize heat-sink effect
- Excellent stability in operation

GLOBAL MODEL	HISTORICAL MODEL	MIL-PRF-18546 TYPE	POWER RATING		RESISTANCE RANGE				WEIGHT (Typical) g
			$P_{25^{\circ}C}$ W		MIL. RANGE SHOWN IN BOLD FACE				
			DALE	MILITARY	$\pm 0.05\%, \pm 0.1\%$	$\pm 0.25\%$	$\pm 0.5\%$	$\pm 1\%, \pm 3\%, \pm 5\%$	
RH005	RH-5	RE60G	7.5 (5)	5	0.5 - 6.75k	0.1 - 8.6k	0.05 - 8.6k	0.02 - 24.5k 0.10 - 3.32k	3
NH005	NH-5	RE60N	7.5 (5)	5	0.5 - 2.32k	0.1 - 3.27k	0.05 - 3.27k	0.05 - 12.75k 1.0 - 1.65k	3.3
RH010	RH-10	RE65G	12.5 (10)	10	0.5 - 12.7k	0.1 - 16.69k	0.05 - 16.69k	0.01 - 47.1k 0.10 - 5.62k	6
NH010	NH-10	RE65N	12.5 (10)	10	0.5 - 4.45k	0.1 - 5.54k	0.05 - 5.54k	0.05 - 23.5k 1.0 - 2.8k	8.8
RH025	RH-25	RE70G	25	20	0.5 - 25.7k	0.1 - 32.99k	0.05 - 32.99k	0.01 - 95.2k 0.10 - 12.1k	13
NH025	NH-25	RE70N	25	20	0.5 - 9.09k	0.1 - 12.8k	0.05 - 12.8k	0.05 - 47.6k 1.0 - 6.04k	16.5
RH050	RH-50	RE75G	50	30	0.5 - 73.4k	0.1 - 96k	0.05 - 96k	0.01 - 273k 0.10 - 39.2k	28
NH050	NH-50	RE75N	50	30	0.5 - 26k	0.1 - 36.7k	0.05 - 36.7k	0.05 - 136k 1.0 - 19.6k	35
RH100	RH-100	RE77G	100	75	0.5 - 90k	0.1 - 90k	0.05 - 90k	0.05 - 90k 0.05 - 29.4k	350
NH100	NH-100	RE77N	100	75	0.5 - 37.5k	0.1 - 37.5k	0.05 - 37.5k	0.05 - 37.5k 1.0 - 14.7k	385
RH250	RH-250	RE80G	250	120	0.5 - 116k	0.1 - 116k	0.05 - 116k	0.05 - 116k 0.10 - 35.7k	630
NH250	NH-250	RE80N	250	120	0.5 - 48.5k	0.1 - 48.5k	0.05 - 48.5k	0.05 - 48.5k 1.0 - 17.4k	690

NOTE: Figures in parentheses on RH-5 and RH-10 indicate wattage printed on parts, new construction allows these resistors to be rated at higher wattage but will **only** be printed with the higher wattage on customer request.

GLOBAL PART NUMBER INFORMATION				
New Global Part Numbering: RH0054R125FC02 (preferred part numbering format)				
<div style="display: flex; justify-content: space-around; font-weight: bold;"> RH0054R125FC02 </div>				
GLOBAL MODEL	RESISTANCE VALUE	TOLERANCE CODE	PACKAGING	SPECIAL
RH005	L = Milliohm R = Decimal K = Thousand 8L000 = 0.008Ω 15R00 = 15Ω 10K00 = 10KΩ	A = ± 0.05% B = ± 0.1% C = ± 0.25% D = ± 0.5% F = ± 1.0% J = ± 5.0%	*E02 = Lead Free, Card Pack (RH005 – RH050) *E01 = Lead Free, Skin Pack (RH100 & RH250) Lead Free is not available on RE military type *(Lead Free parts to be released Q1 2005) C02 = Tin/Lead, Card Pack (RH005 – RH050) J01 = Tin/Lead, Skin Pack (RH100 & RH250)	(Dash Number) (up to 3 digits) From 1-999 as applicable
Historical Part Number example: RH-5 4.125Ω 1% C02 (will continue to be accepted)				
RH-5	4.125Ω	1%	C02	
HISTORICAL MODEL	RESISTANCE VALUE	TOLERANCE CODE	PACKAGING	



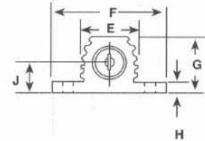
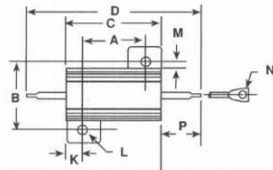
RH, NH

Wirewound Resistors, Military, MIL-PRF-18546 Qualified,
Type RE, Aluminum Housed, Chassis Mount

Vishay Dale

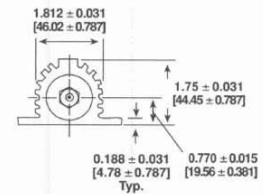
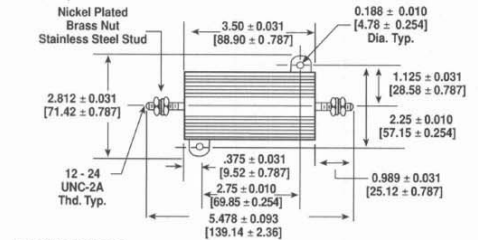
DIMENSIONS

RH-5, -10, -25, -50
NH-5, -10, -25, -50

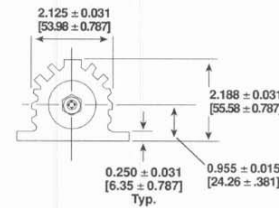
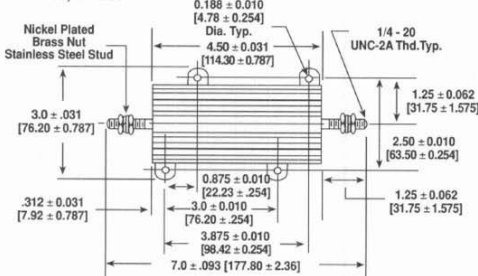


MODEL	DIMENSIONS in inches [millimeters]													
	A	B	C	D	E	F	G	H	J	K	L	M	N	P
RH-5 NH-5	0.444 ± 0.005 [11.28 ± 0.127]	0.490 ± 0.005 [12.45 ± 0.127]	0.600 ± 0.031 [15.24 ± 0.787]	1.125 ± 0.062 [28.58 ± 1.57]	0.334 ± 0.015 [8.48 ± 0.381]	0.646 ± 0.015 [16.41 ± 0.381]	0.320 ± 0.015 [8.13 ± 0.381]	0.065 ± 0.010 [1.65 ± 0.254]	0.133 ± 0.010 [3.38 ± 0.254]	0.078 ± 0.010 [1.98 ± 0.254]	0.093 ± 0.005 [2.36 ± 0.127]	0.078 ± 0.015 [1.98 ± 0.381]	0.050 ± 0.005 [1.27 ± 0.127]	0.266 ± 0.062 [6.76 ± 1.57]
RH-10 NH-10	0.562 ± 0.005 [14.27 ± 0.127]	0.625 ± 0.005 [15.88 ± 0.127]	0.750 ± 0.031 [19.05 ± 0.787]	1.375 ± 0.062 [34.93 ± 1.57]	0.420 ± 0.015 [10.67 ± 0.381]	0.800 ± 0.015 [20.32 ± 0.381]	0.390 ± 0.015 [9.91 ± 0.381]	0.075 ± 0.010 [1.91 ± 0.254]	0.165 ± 0.010 [4.19 ± 0.254]	0.093 ± 0.010 [2.36 ± 0.254]	0.094 ± 0.005 [2.39 ± 0.127]	0.102 ± 0.015 [2.59 ± 0.381]	0.085 ± 0.005 [2.16 ± 0.127]	0.312 ± 0.062 [7.92 ± 1.57]
RH-25 NH-25	0.719 ± 0.005 [18.26 ± 0.127]	0.781 ± 0.005 [19.84 ± 0.127]	1.062 ± 0.031 [26.97 ± 0.787]	1.938 ± 0.062 [49.23 ± 1.57]	0.550 ± 0.015 [13.97 ± 0.381]	1.080 ± 0.015 [27.43 ± 0.381]	0.546 ± 0.015 [13.87 ± 0.381]	0.075 ± 0.010 [1.91 ± 0.254]	0.231 ± 0.010 [5.87 ± 0.254]	0.172 ± 0.010 [4.37 ± 0.254]	0.125 ± 0.005 [3.18 ± 0.127]	0.115 ± 0.015 [2.92 ± 0.381]	0.085 ± 0.005 [2.16 ± 0.127]	0.438 ± 0.062 [11.13 ± 1.57]
RH-50 NH-50	1.562 ± 0.005 [39.67 ± 0.127]	0.844 ± 0.005 [21.44 ± 0.127]	1.968 ± 0.031 [49.99 ± 0.787]	2.781 ± 0.062 [70.64 ± 1.57]	0.630 ± 0.015 [16.00 ± 0.381]	1.140 ± 0.015 [28.96 ± 0.381]	0.610 ± 0.015 [15.49 ± 0.381]	0.088 ± 0.010 [2.24 ± 0.254]	0.260 ± 0.010 [6.60 ± 0.254]	0.196 ± 0.010 [4.98 ± 0.254]	0.125 ± 0.005 [3.18 ± 0.127]	0.107 ± 0.015 [2.72 ± 0.381]	0.085 ± 0.005 [2.16 ± 0.127]	0.438 ± 0.062 [11.13 ± 1.57]

RH-100, NH-100



RH-250, NH-250



RH, NH



Vishay Dale Wirewound Resistors, Military, MIL-PRF-18546 Qualified, Type RE, Aluminum Housed, Chassis Mount

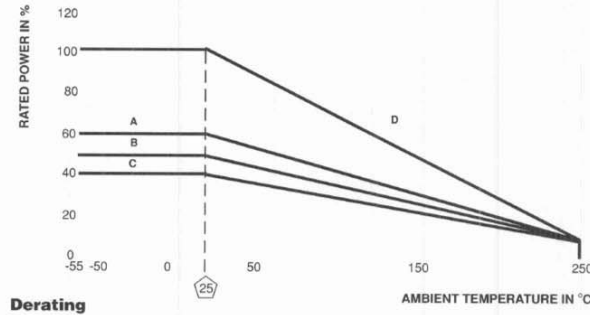
TECHNICAL SPECIFICATIONS		
PARAMETER	UNIT	RH RESISTOR CHARACTERISTICS
Temperature Coefficient	ppm/°C	± 100 for 0.1Ω to 0.99Ω, ± 50 for 1Ω to 9.9Ω, ± 20 for 10Ω and above
Dielectric Withstanding Voltage	V _{AC}	1000 for RH-5, RH-10 and RH-25, 2000 for RH-50, 4500 for RH-100 and RH-250
Short Time Overload	-	5 x rated power for 5 seconds
Maximum Working Voltage	V	(P X R) ^{1/2}
Insulation Resistance	Ω	10,000 Megohm minimum dry, 1000 Megohm minimum after moisture test
Terminal Strength	lb	5 minimum for RH-5 and RH-10, 10 minimum for all others
Solderability	-	MIL-PRF-18546 Type - Meets requirements of ANSI J-STD-002
Operating Temperature Range	°C	- 55/+ 250

POWER RATING

Vishay RH resistor wattage ratings are based on mounting to the following heat sink:
 RH-5 and RH-10: 4" x 6" x 2" x 0.040" thick aluminum chassis (129 sq. in. surface area)
 RH-25: 5" x 7" x 2" x 0.040" thick aluminum chassis (167 sq. in. surface area)
 RH-50: 12" x 12" x 0.059" thick aluminum panel (291 sq. in. surface area)
 RH-100 and RH-250: 12" x 12" x 0.125" thick aluminum panel (294 sq. in. surface area)

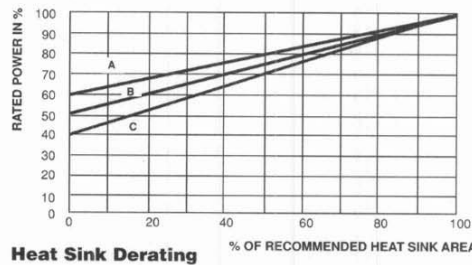
AMBIENT TEMPERATURE DERATING

Derating is required for ambient temperatures above 25°C, see the following graph.
 Curves A, B, C apply to operation of unmounted resistors. Curve D applies to all types when mounted to specified heat sink.
 A = RH-5 and RH-10 size resistor, unmounted
 B = RH-25 size resistor, unmounted
 C = RH-50, RH-100 and RH-250 size resistor, unmounted
 D = All types mounted to recommended aluminum heat sink



REDUCED HEAT SINK DERATING:

Derating is also required when recommended heat sink area is reduced.
 A = RH-5 and RH-10 size resistor
 B = RH-25 size resistor
 C = RH-50, RH-100 and RH-250 size resistor



**RH, NH**

Wirewound Resistors, Military, MIL-PRF-18546 Qualified,
Type RE, Aluminum Housed, Chassis Mount

Vishay Dale

MATERIAL SPECIFICATIONS

Element: Copper-nickel alloy or nickel-chrome alloy, depending on resistance value

Core: Ceramic, steatite or alumina, depending on physical size

Encapsulant: Silicone molded construction

Housing: Aluminum with hard anodic coating

End Caps: Stainless steel

Standard Terminals: 100% Sn, w/Nickel underplate, or 60/40 Sn/Pb, w/Nickel underplate, coated Copperweld® on RH-5 through RH-50 size. Threaded stainless steel terminals on RH-100 and RH-250.

NOTE: Military (RE) parts are only available with 60/40 Sn/Pb finish.

Part Marking: DALE, Model, Wattage, Value, Tolerance, Date Code

NH NON-INDUCTIVE

Models of equivalent physical and electrical specifications are available with non-inductive (Aryton-Perry) winding. They are identified by substituting the letter N for R in the model number (NH-5, for example).

SPECIAL MODIFICATIONS

A number of special modifications to the aluminum housed resistor style are available upon request. Special modifications include:

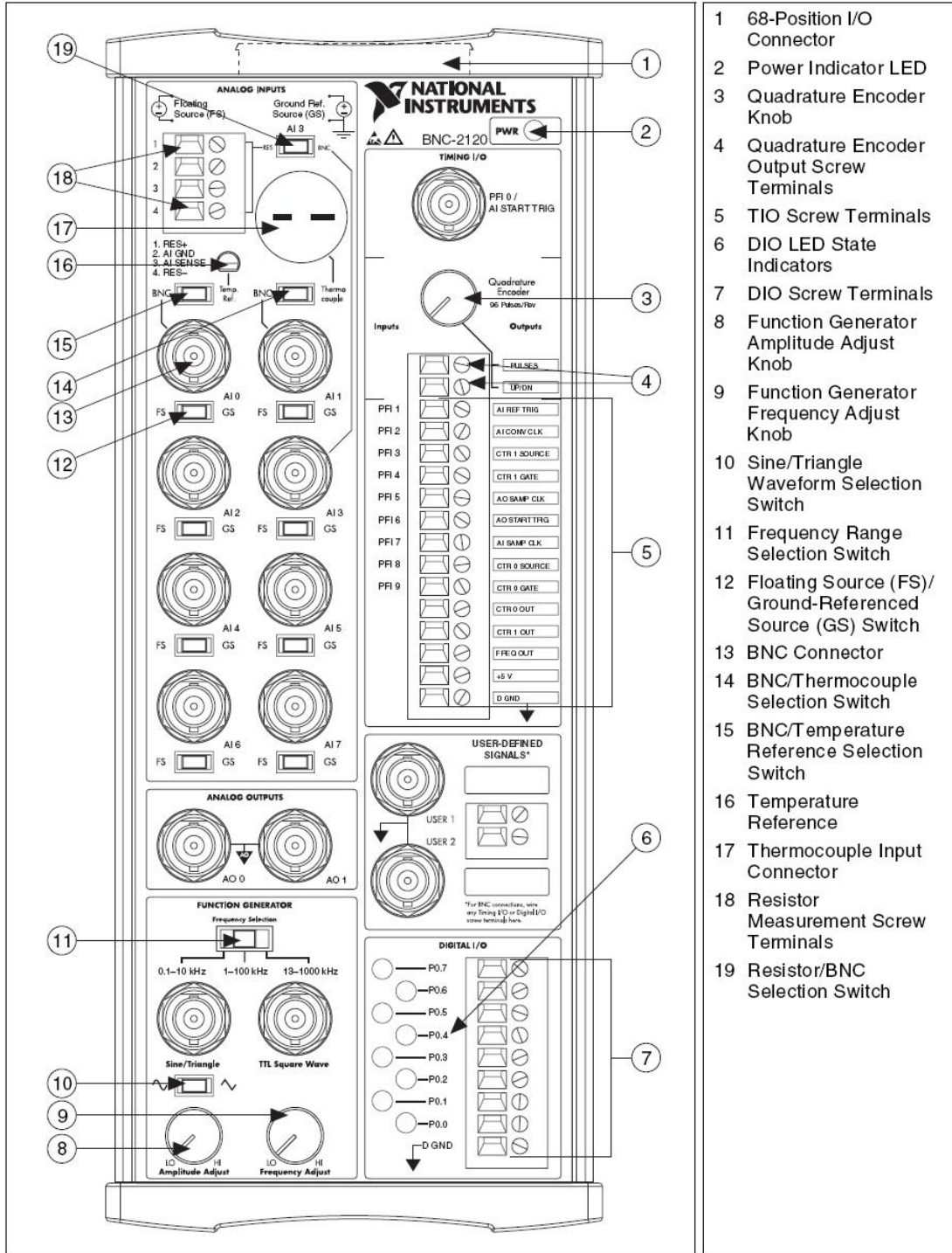
- Terminal configurations and materials
- Resistance values and tolerances
- Low resistance temperature coefficient (RTC)
- Housing configuration
- Threaded mounting holes
- Preconditioning and other additional testing

APPLICABLE MIL SPECIFICATIONS

MIL-PRF-18546 is the military specification covering aluminum housed, chassis mount, power resistors. VISHAY RH and NH resistors are listed as qualified on the MIL-PRF-18546 QPL.

PERFORMANCE		
TEST	CONDITIONS OF TEST	TEST LIMITS
Thermal Shock	Rated power applied until thermally stable, then a minimum of 15 minutes at - 55°C	± (0.5% + 0.05Ω) ΔR
Short Time Overload	5 x rated power for 5 seconds	± (0.5% + 0.05Ω) ΔR
Dielectric Withstanding Voltage	1000Vrms for RH-5, RH-10 and RH-25; 2000Vrms for RH-50 4500Vrms for RH-100 and RH-250; duration one minute	± (0.2% + 0.05Ω) ΔR
Temperature	250°C for 2 hours	± (0.5% + 0.05Ω) ΔR
Moisture Resistance	MIL-STD-202 Method 106, 7b not applicable	± (1.0% + 0.05Ω) ΔR
Shock, Specified Pulse	MIL-STD-202 Method 213, 100g's for 6 milliseconds, 10 shocks	± (0.2% + 0.05Ω) ΔR
Vibration, High Frequency	Frequency varied 10 to 2000Hz, 20g peak, 2 directions 6 hours each	± (0.2% + 0.05Ω) ΔR
Load Life	1000 hours at rated power, + 25°C, 1.5 hours "ON", 0.5 hours "OFF"	± (1.0% + 0.05Ω) ΔR
Terminal Strength	30 second, 5 pound pull test for RH-5 and RH-10, 10 pound pull test for other sizes, torque test - 24 pound inch for RH-100 and 32 pound inch for RH-250	± (0.2% + 0.05Ω) ΔR

D.3 National Instruments BNC 2120



- 1 68-Position I/O Connector
- 2 Power Indicator LED
- 3 Quadrature Encoder Knob
- 4 Quadrature Encoder Output Screw Terminals
- 5 TIO Screw Terminals
- 6 DIO LED State Indicators
- 7 DIO Screw Terminals
- 8 Function Generator Amplitude Adjust Knob
- 9 Function Generator Frequency Adjust Knob
- 10 Sine/Triangle Waveform Selection Switch
- 11 Frequency Range Selection Switch
- 12 Floating Source (FS)/Ground-Referenced Source (GS) Switch
- 13 BNC Connector
- 14 BNC/Thermocouple Selection Switch
- 15 BNC/Temperature Reference Selection Switch
- 16 Temperature Reference
- 17 Thermocouple Input Connector
- 18 Resistor Measurement Screw Terminals
- 19 Resistor/BNC Selection Switch

D.4 AE Techron Inc LVC 5050 Amplifier

The LEES facility in building N10 operates two of these amplifiers. Although these amplifiers look identical, one is actually an older model that is operated differently. In the older model, the front panel controls have been disabled so that the only voltage controls are the on/off switch and the gain selector in the rear.

APPLICATION

The **LVC 5050** is a general purpose, high voltage, medium continuous current, linear power amplifier. It works best when driving loads of 2 - 16 ohms. The **LVC 5050** works well with either pulsed or continuous test signals or environments that have both

conditions. The **LVC 5050** has two (2) separate channels that can be operated independently or combined for greater maximum voltage or current. In *Bridge-mono mode* the available output voltage doubles. In *Parallel-mono mode* the amplifier operates with twice the available output current

FEATURES

- ▶ Bi Level™ Power Supply, amplifier optimizes itself for either, high pulse voltage or low voltage high current, dynamically. The **LVC 5050** produces less heat, higher long term power, with no added distortion.
- ▶ Output of 20.0 amperes rms, or 106 volts rms, per channel depending on load.
- ▶ Frequency bandwidth of DC to 20 kHz at full power.
- ▶ Option of controlled voltage, or controlled current operation, modes changed via a jumper
- ▶ User-adjustable voltage or current limiting
- ▶ Remote switching to standby mode by contact closure
- ▶ External monitoring of voltage and current output
- ▶ Equipped with circuitry to protect the amplifier from input overloads, improper output connection (including shorts and improper loads), excessive temperature, voltage or current.
- ▶ Shipped ready to operate using single-phase, 120-volt AC mains. Also available in 100, 200, 208, 230 and 240 VAC versions.
- ▶ Installs easily into a standard 19 inch rack, or stands alone for bench top operations

INDICATORS AND CONTROLS

- ▶ Front panel LEDs indicate signal presence and output overload
- ▶ A pushbutton power "On/Off" located on the front panel
- ▶ Two gain controls on the front panel for controlled voltage applications
- ▶ A back panel slide switch to lift signal ground from chassis ground
- ▶ A back panel slide switch to choose between 2 channel, bridge mono and parallel mono operation



AE Techron, Inc. LVC 5050



Call us or visit our website! When your project or product requires a low noise, low distortion, high power amplifier solution, contact **AE Techron Inc.** We are happy to help.

PERFORMANCE (One hour continuous ratings)

Frequency response

+/- 0.1 dB from 20 Hz to 20 kHz at 1 watt

Phase response

+/- 10 Degrees (10 Hz to 20 kHz at 1 watt)

Signal-to-noise ratio

At 26 dB gain, better than 105 dB (A-weighted) below full output

THD

Less than 0.05% from 20 Hz to 1 kHz increasing linearly to 0.1% at 20 kHz at full output

I.M. Distortion

<0.05% from 410 milliwatts to full output at 26 dB gain with and 8 ohm load

Slew rate

> 31V per microsecond

Load Impedance

Rated for 16,8,4 and 2 ohm use. Safe with all load types even reactive ones.

Input Impedance

Greater than 10K ohms, balanced, and 5K ohms unbalanced.

Output impedance

Less than 10 milliohms in series with less than 2 microhenries

OUTPUT POWER LVC 5050

	40 mSec			1 Hour Continuous			
	Ohms	Watts	Volts	Amps	Watts	Volts	Amps
Single Channel	2	2505	71	35	800	40	20
	4	1940	88	22	576	48	12
	8	1270	101	12	1205	98.2	12
	16	702	106	7	702	106	7

	40 mSec			1 Hour Continuous			
	Ohms	Watts	Volts	Amps	Watts	Volts	Amps
Bridged Mono	4	5320	146	36			
	8	3003	155	19	3003	155	19
	16	2036	180	11	2036	180	11

	40 mSec			1 Hour Continuous			
	Ohms	Watts	Volts	Amps	Watts	Volts	Amps
Parallel Mono	1	5320	73	73			
	2	4045	90	45			
	4	2670	103	26	2416	98.3	25
	8	1378	105	13	1324	102.9	13



PHYSICAL CHARACTERISTICS

Chassis: The Amplifier is designed for stand alone, or rack mounted, operation. The Chassis is black steel with a silver finished aluminum front panel. The unit occupies three EIA 19-inch-wide units.

Weight: 77 lbs. (35.2 kg), Shipping 88 lbs. (40.2 kgs)

AC Power: Single phase, 120 volts, 60 Hz, 30 amperes ac service. (Note: 100, 120, 200, 208, 230 or 240 volt, 50-60 Hz models are available Call for specifications.) US models come with 3 blade NEMA TT30P plug.

Cooling: Forced air cooling from the front, through removable filters, to the back.

Dimensions: 19 in. x 16 in. x 5.25 in (48.3 cm x 40.3.0 cm x 13.3 cm)

SUPPORT

When you purchase an **AE Techron** amplifier, a full complement of technical and factory support personnel join your team. **AE Techron Inc.** provides:

- ▶ Applications engineering for your technical questions and customized product needs.
- ▶ A one year limited warranty to protect your equipment investment.
- ▶ A fully equipped service center to keep your amplifier operating at original performance requirements.

AE Techron Inc.

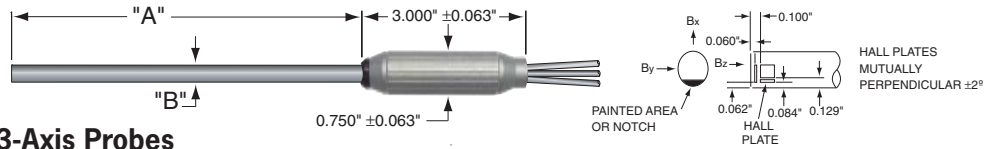
2507 Warren Street
Elkhart, IN 46516 USA

Phone: 574-295-9496

Fax: 574-295-9496

E-mail: Sales@aetechron.com
Web: www.aetechron.com

D.5 F.W. Bell Three Probe and 7030 Teslameter



Standard 3-Axis Probes

Model	A	B	C	D	E	F	G	Stem Material	Linearity % of Reading	Frequency Range	Sensitivity	Nominal Active Area	Oper. Temp. Range	Temp. Stability (Max)	
														Zero (G/°C)	Calibrate (%/°C)
ZOA73-3208-05	8.0" ±0.125"	0.312" ±0.005"	N/A	N/A	N/A	N/A	N/A	Alum.	0.25% to 10kG	DC to 400Hz	1X	0.060" Dia.	0°C to +75°C	±0.100	-0.040
ZOA73-3208-05-T															
ZOA73-3208-15															
ZOA73-3208-15-T															
ZOA73-3208-30															
ZOA73-3208-30-T															

Description

The Model 7030 three-channel GAUSS/TESLA METER from **F.W. Bell** leads the way for Advanced Hall Effect Magnetic measuring technology. The easy-to-use front panel programming feature incorporates the latest in user control operations. The 7030 is capable of simultaneously measuring and displaying *seven different parameters per channel* -- flux density, frequency, temperature, min, max, peak and valley. With the 7030's vector summation feature, that makes a total of **27** different parameters.

This high accuracy instrument is fully equipped to meet most magnetic measuring applications. Bell's exclusive dynamic probe correcting software increases the 7030 measurement capabilities to make it *the most versatile magnetic measuring tool in the world*.

Key features include high-resolution, high-accuracy and high-speed with a large graphic electroluminescent display. The 7030 features 50 kHz frequency response, temperature and frequency measurements, Auto Zero, Auto Range, Hold functions for Peak, Valley, Min and Max, corrected and uncorrected outputs for each channel and Vector Summation and angle. The Model 7030 provides the user with gauss, tesla, Oe, A/m, IEEE-488 and RS-232 communications ports and Classifier output.

The 7030 operates with Bell's fifth generation Hall Effect probes. These probes provide temperature compensation and measurement readings (0°C to +75°C) while monitoring the magnetic field. The easy-to-read 1/4 VGA display is easily viewable in most light conditions and can be customized to meet a user's specific needs. Applications range from basic magnetic measuring to sensitive complicated three-axis vector summing requirements. All instruments are fully CE compliant.

Features

- Bright 1/4-VGA Readout
- Large electroluminescent graphic display
- Over 100 standard probes available
- Automatic probe coefficient correction
- Displays in Gauss, Tesla, Amp/meter or Oe
- Relative Mode
- Fully menu-driven for easy operation
- Auto Zero and Auto Calibration
- IEEE-488 and RS-232 interface
- CE Compliant
- Manufactured to ISO 9000 standards
- Comprehensive Technical Support

SPECIFICATION	
Ranges	300mG (30μT)* 3kG(300mT) 3G (300μT)* 30kG (3T) 30G (3mT) 300kG(30T)† 300G (30mT) * Low field probe † High field probe
Resolution	1 μG (0.1nT) to 1G (0.1mT) (Depending on probe selection)
Accuracy (Displayed Reading)	
dc basic	±0.05% of reading
ac basic	±2% of reading
Frequency Range	
dc mode	dc to 250Hz
ac mode	20Hz to 50kHz
Accuracy (Corrected Analog Output)	
dc basic	±0.1% of range
ac basic	±2% of range
Frequency Range	dc to 500Hz
Frequency Range (Uncorrected Analog Output)	
dc mode	dc to 100Hz
ac mode	20Hz to 50kHz
Analog Output	
Output Voltage	±3V FS. or ±10V F.S. or adjustable from 0.1 - 9.9V
Source Impedance	<100 ohms
Connector	Standard BNC
Additional Influences	
Temperature Coefficient	±(0.02% of reading ±1 count)/ °C
Temperature Range	
Operating	0°C to +50°C
Storage	-20°C to +60°C
Front Panel Display	1/4 VGA, 320 x 240 pixels Electroluminescent graphic display with 4 shades of amber 4.7" (119 mm) W x 3.5" (89mm) H
Communication Ports	
RS-232	Standard 9-pin "D" connector
Baud Rate	300,600,1200,2400,4800,9600,19200,38400 bits/sec
IEEE-488	Standard 24-pin GPIB connector
Protocol	IEEE-1987.2 and SCPI-1999
Power	
Volts:	100/120 or 220/240
Frequency:	50-60 Hz or 50-60 Hz
Current:	1.0 A (max) or 0.5 A (max)
Size	
Width	16.3" (414 mm)
Height	5.2" (132mm)
Depth	13.5" (343mm)
Weight	
Net	19.6 lbs. (8.9 kg)
Shipping	25.8 lbs. (11.6 kg)

Hall Effect GAUSSMETERS



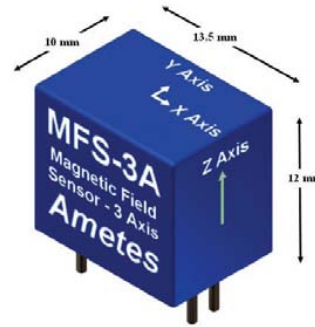
Due to continuous process improvement, specifications subject to change without notice.

D.6 GMW Three Axis Magnetic Field Sensor

Ametes

Magnetic Field Sensor - 3 Axis, MFS-3A

The high magnetic field sensitivity, accurate calibration, high stability and high signal output of the Sentron CSA-1V Hall effect IC enable it to be conveniently used to monitor the extended fields from magnetic items and electric equipment. As a demonstration of the CSA-1V capability, three CSA-1V with sensitive axes mutually perpendicular, are combined in a compact module as the MFS-3A. Three output voltages $V_x = S \cdot B_x$, $V_y = S \cdot B_y$ and $V_z = S \cdot B_z$ are generated proportional to the magnetic flux density components B_x , B_y and B_z with the sensitivity $S = 280 \text{ mV/mT}$ over the field range of $\pm 7.3 \text{ mT}$. This enables calculation of the total magnetic flux density, $B = (B_x^2 + B_y^2 + B_z^2)^{1/2} = (V_x^2 + V_y^2 + V_z^2)^{1/2} / S$.

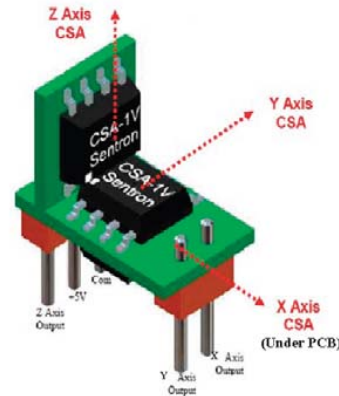


Specifications


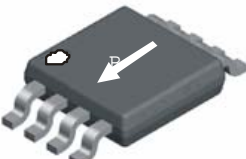
- * Measures B_x , B_y , B_z
- * Suitable for environmental magnetic fields
- * Field range: $\pm 7.3 \text{ mT}$ ($\pm 73 \text{ G}$)
- * Resolution: $\pm 10 \mu\text{T}$ ($\pm 0.1 \text{ G}$)
- * Three linear analog outputs V_x , V_y , V_z of 0.5V to 4.5V
- * Sensitivity: $S = 280 \text{ mV/mT}$
- * Accuracy: $\pm 3\%$
- * Angular alignment: $\pm 3 \text{ deg}$
- * Frequency response dc to 100kHz (-3dB)
- * Small size: 10 x 13.5 x 12mm (0.39 x 0.53 x 0.47inch)
- * Low weight: 2.5g (0.1oz)
- * Low power: 36mA max at 5V

Applications:

- * Quality assurance of magnetized materials and items such as sealing strips and permanent magnets by fast and complete characterization of the external magnetic field.
- * Detection/separation of magnetic and non-magnetic materials by monitoring the modification of the local or imposed field caused by magnetic item/items.
- * Non-contact, non-invasive and continuous "Condition Monitoring" of electrical motors, generators, transformers or inductors by comparing the amplitudes of selected external or "leakage" field spectral components with initial or reference values. Quality assurance of electrical components by leakage field measurement.
- * Independent monitoring of the ON/OFF status of large magnets with extended fringing fields. The MFS-3A output can be used to operate warning indicators and/or interlocks. Resolution of $\pm 10 \mu\text{T}$ readily allows measurement of the $500 \mu\text{T}$ (5G) safety level applicable to Magnetic Resonance Imagers (MRI).
- * Wearable, battery operated "Personal Magnetic Field Detector" to immediately generate a warning to the wearer that they have entered a region of increased magnitude magnetic field.
- * Magnetic field detection and warning or interlock to be incorporated in magnetically sensitive equipment such as time standards or patient support equipment that may be used in the fringe field of an MRI or other large magnet.



Specifications subject to change. For the latest Specification refer to the Senis or GMW websites. Revision Date: 5 Feb 2007 MFS-3A
 Europe - Senis GmbH: Technoparkstrasse 1, 8005 Zurich, Switzerland. www.senis.ch. +44 (79) 266-8756
 The Americas - GMW Associates: 955 Industrial Road, San Carlos, CA 94070, USA. www.gmw.com. +1 (650) 802-8292

<h1 style="font-size: 2em; margin: 0;">GMW</h1>	<p>Sentron CSA -1V Revised Jan 2005</p>
<p>CSA-1V</p> <p>Current Sensor</p>	
<p>Features:</p> <ul style="list-style-type: none"> • Sensitive to a magnetic field parallel to the chip surface • Very high sensitivity • Linear output voltage proportional to a magnetic field • Wide-band: DC to 100kHz • Very low offset and offset-drift • Very low noise • Isolated from current conductor • Surface mount SO IC-8 package 	<p>Applications:</p> <ul style="list-style-type: none"> • AC and/or DC current measurement • Wide-Band Magnetic Field Measurement • Battery Chargers • AC-DC Converters • Motor Control
<p>General Description</p> <p>The CSA-1V is a single-axis integrated magnetic field sensor based on the Hall effect. The circuit is fabricated using a conventional CMOS technology with an additional ferromagnetic layer. The ferromagnetic layer is used as a magnetic flux concentrator providing a high magnetic gain. Therefore, the circuit features very high magnetic sensitivity, low offset, and low noise.</p> <p>The CSA-1V is packaged in a standard SO IC-8 full plastic package. This package provides:</p> <ul style="list-style-type: none"> • highest isolation for applications with the current conductor on the PCB (up to 600V) • highest sensitivity for applications with the current lead above the chip. 	
<p>Package: SO IC-8</p>	
<p>Pin Out:</p> 	<ol style="list-style-type: none"> 1 A_OUT, analog sensor output 2 V_{DD} pos. supply voltage 3 Not connected 4 PV, programming voltage ¹⁾ 5 GND, supply common 6 PD, programming data ¹⁾ 7 PC, programming clock ¹⁾ 8 CO_OUT, common output
<p>Note 1: Used for factory programming</p>	
<p>Manufactured by: Sentron AG (A Melexis Company) • Baarerstrasse 73 • 6300 Zug • Switzerland • Tel: +41 (41) 711 2170 • Fax: +41 (41) 711 2188 • www.sentron.ch • sales@sentron.ch</p>	
<p>GMW Associates, 955 Industrial Rd, San Carlos, CA 94070 www.gmw.com • Tel: (650) 802-8292 • Fax: (650) 802-8298 • Email: sales@gmw.com</p>	

GMW

Sentron CSA -1V

Revised Jan 2005

Absolute Maximum Ratings

Symbol	Parameter	Min.	Typ.	Max.	Unit	Remarks
V _{SUP}	Supply Voltage	0		6	V	
T	Ambient Temperature	-40		+150	°C	

Recommended Operating Conditions

Symbol	Parameter	Min.	Typ.	Max.	Unit	Remarks
V _{SUP}	Supply Voltage	4.5	5	5.5	V	
I _{OUT}	Output Current	-1		1	mA	
C _L	Load Capacitance			1000	pF	

Electrical Characteristics

At T = -40°C to 150°C, V_{SUP} = 4.5V to 5.5V if not otherwise specified.

Symbol	Parameter	Min.	Typ.	Max.	Unit	Test Conditions
I _{SUP}	Supply Current		11	16	mA	
V _{Common}	Common (reference) Output Voltage ²⁾	V _{SUP} /2 -20mV	V _{SUP} /2	V _{SUP} /2 +20mV		I _{OUT} = 0mA
BW	Bandwidth: DC to		100		kHz	
t _R	Response Time			6	µs	

Note 2: Ratio metric (proportional to V_{SUP})

Characteristics of the Linear Magnetic Field Sensor^{3,4)}

With V_{SUP} = 5V and in the temperature range -40°C to 150°C, if not otherwise specified.

Symbol	Parameter	Min.	Typ.	Max.	Unit	Test Conditions
S	Magnetic Sensitivity ³⁾	270	280 ⁶⁾	290	V/T	B = B _L
ΔS/ΔT	Magn. Sensitivity Temperature Drift	-0.02		0.02	%/°C	I _{OUT} = 0mA T = -20°C to 125°C
V _{off}	Offset Voltage ³⁾	-15	0	15	mV	B = 0T, I _{OUT} = 0mA, T = 20°C
B _{off}	Equivalent Magnetic Offset ³⁾	-50	0	50	µT	B = 0T, I _{OUT} = 0mA T = -20°C to 80°C
ΔV _{off} /ΔT	Offset Temperature Drift	-0.2	0	0.2	mV/°C	B = 0T, I _{OUT} = 0mA, T = -20°C to 125°C
B _{FS}	Full Scale Magnetic Field Range ⁵⁾	-7.5		7.5	mT	
B _L	Linear Magnetic Field Range	-5		5	mT	
NL	Non Linearity		0.1 0.5	0.2 1	%	B = B _L B = B _{FS}
ΔB _{noise}	Input referred magnetic noise spectrum density (RMS)			125	nT/√Hz	f = 10Hz to 10kHz

Note 3: Ratio metric (proportional to V_{SUP})

Note 4: When the analog output pin A_{OUT} is used in differential mode (i.e. V_{out} = A_{OUT} - CO_{OUT})

Note 5: Device saturates for B > B_{FS} but is not damaged

Note 6: Specification correction: Was 300 ± 10 V/T. Now 280 ± 10 V/T. All parts manufactured to date, have been calibrated to 280 ± V/T

Manufactured by: Sentron AG (A Melexis Company) • Baarerstrasse 73 • 6300 Zug • Switzerland • Tel: +41 (41) 711 2170 • Fax: +41 (41) 711 2188 • www.sentron.ch • sales@sentron.ch

GMW Associates, 955 Industrial Rd, San Carlos, CA 94070
www.gmw.com • Tel: (650) 802-8292 • Fax: (650) 802-8298 • Email: sales@gmw.com

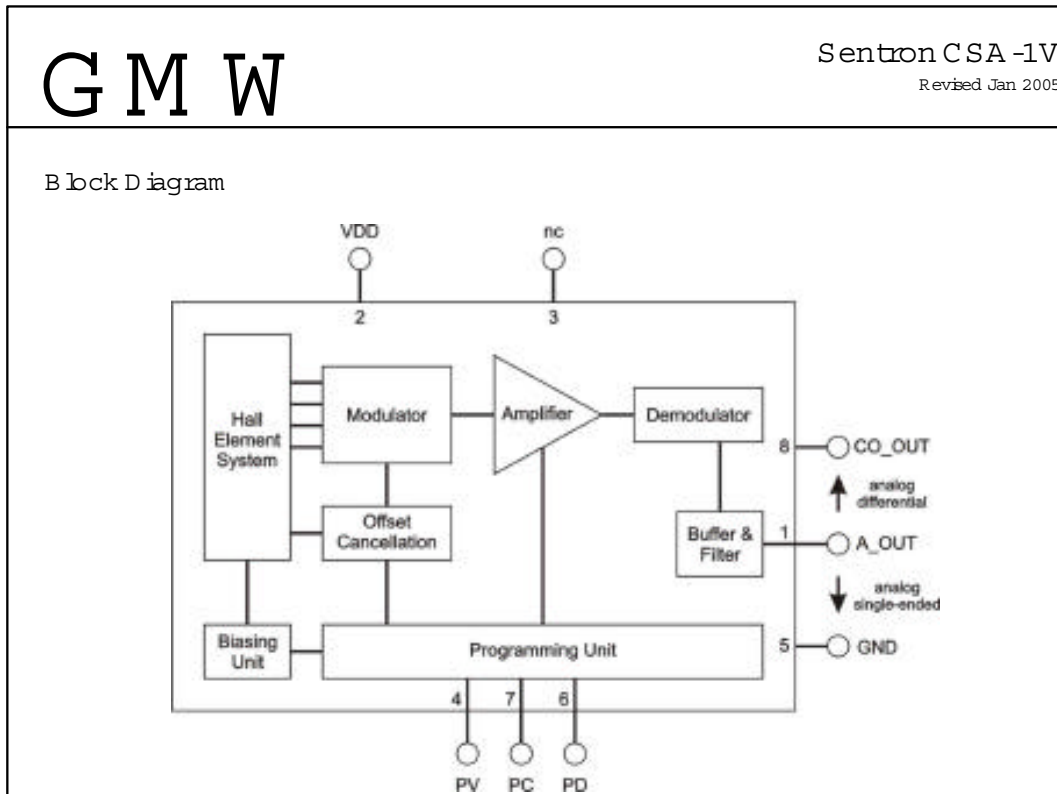
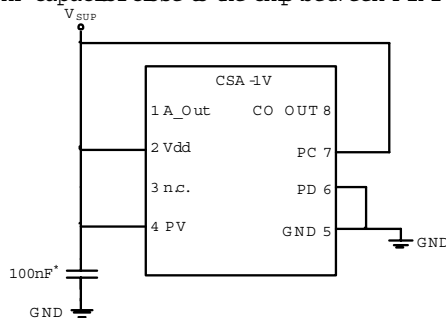


Fig. 1 Block diagram of CSA-1V

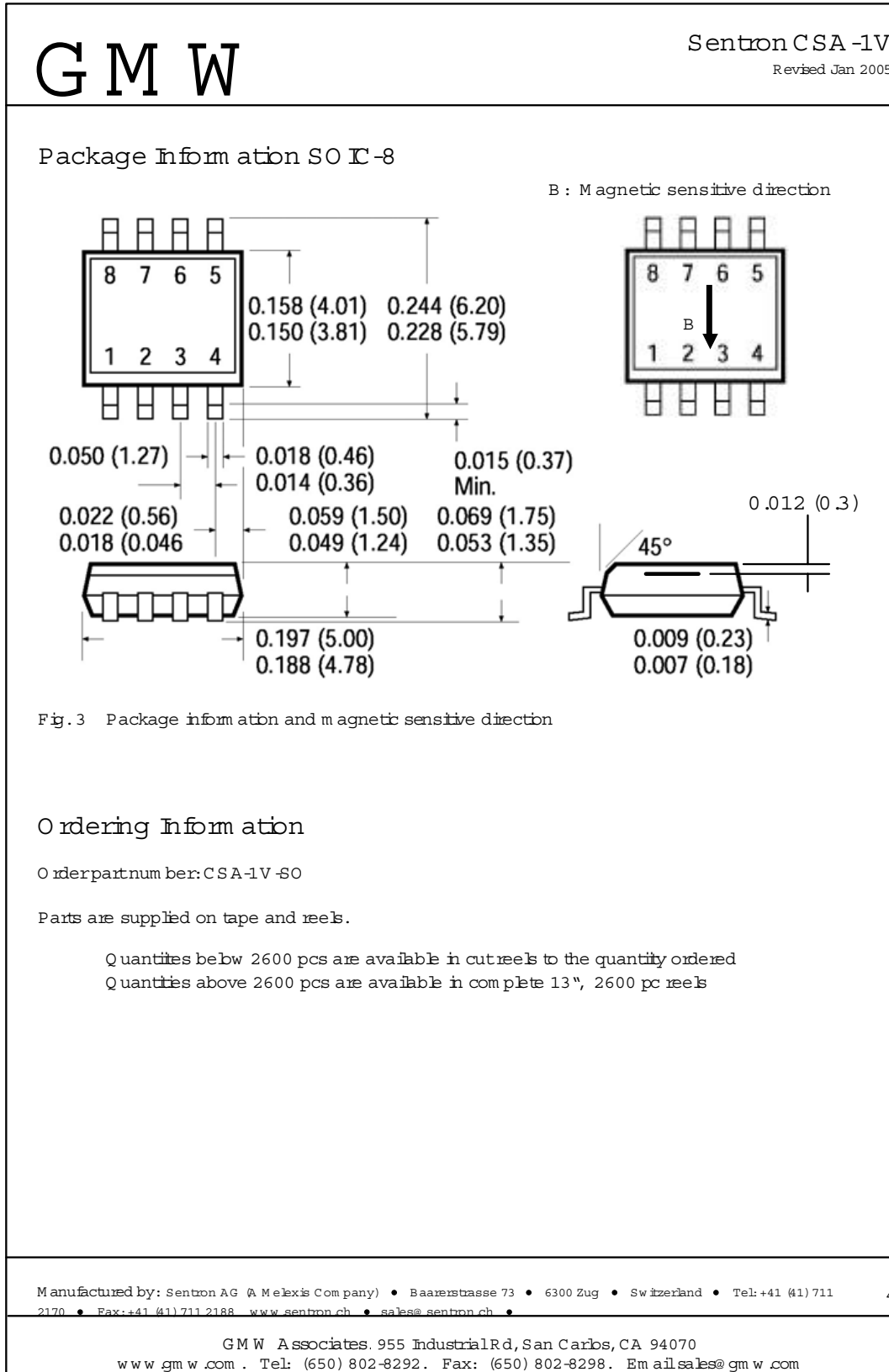
IMPORTANT For reliable operation within the specifications the sensor must be connected as follows:

- Connect Pin 6 (PD) to Pin 5 (GND)
- Connect Pin 7 (PC) to Pin 2 (Vdd)
- Connect Pin 4 (PV) to Pin 2 (Vdd)
- Put a 100nF capacitor close to the chip between Pin 2 (Vdd) and Pin 5 (GND)



* If the supply voltage is disturbed by EM I it can be useful to place a second capacitor (100pF, ceramic) parallel to the 100nF capacitor.

Fig. 2 Connection diagram of CSA-1V



Bibliography

- [1] Éleuthre Élie Nicolas Mascart, J. Joubert, and E. Atkinson, *A Treatise on Electricity and Magnetism*. London: T. De La Rue, 1888 1883, by E. Mascart and J. Joubert. Tr. by E. Atkinson.; 2 v. illus., diags., tab. 24 cm; I. General phenomena and theory.–II. Methods of measurement and applications.
- [2] H. A. Haus and J. R. Melcher, *Electromagnetic Fields and Energy*. Englewood Cliffs, N.J.: Prentice Hall, 1989.
- [3] J. W. Clark, “A New Method for Obtaining a Uniform Magnetic Field,” *Review of Scientific Instruments*, vol. 9, no. 10, pp. 320–322, October 1938. [Online]. Available: <http://link.aip.org/link/?RSI/9/320/1>
- [4] J. William F. Brown and J. H. Sweer, “The Fluxball A Test Coil for Point Measurements of Inhomogeneous Magnetic Fields,” *Review of Scientific Instruments*, vol. 16, no. 10, pp. 276–279, 1945. [Online]. Available: <http://link.aip.org/link/?RSI/16/276/1>
- [5] J. E. Everett and J. E. Osemeikhian, “Spherical Coils for Uniform Magnetic Fields,” *Journal of Scientific Instruments*, vol. 43, no. 7, pp. 470–474, 1966. [Online]. Available: <http://stacks.iop.org/0950-7671/43/470>
- [6] F. Primdahl and P. A. Jensen, “Compact Spherical Coil for Fluxgate Magnetometer Vector Feedback,” *Journal of Physics E: Scientific Instruments*, vol. 15, no. 2, pp. 221–226, 1982. [Online]. Available: <http://stacks.iop.org/0022-3735/15/221>
- [7] J. A. H. Jr., “Magnetic field generator,” Patent, December 1941.

- [8] K. N. Henrichsen, “Magnetic Field Imaging,” CERN Accelerator School Materials.
- [9] J. L. Symonds, “Methods of Measuring Strong Magnetic Fields,” *Reports on Progress in Physics*, vol. 18, no. 1, pp. 83–126, 1955. [Online]. Available: <http://stacks.iop.org/0034-4885/18/83>
- [10] R. E. Rosensweig, *Ferrohydrodynamics*. Cambridge ; New York: Cambridge University Press, 1985.
- [11] M. Zahn, “Magnetic Fluid and Nanoparticle Applications to Nano-Technology,” *Journal of Nanoparticle Research*, vol. 3, pp. 73–78, 2001.
- [12] S. M. Elborai, *Ferrofluid Surface and Volume Flows in Uniform Rotating Magnetic Fields*, 2006.
- [13] X. He, *Ferrohydrodynamic Flows in Uniform and Non-uniform Rotating Magnetic Fields*, 2006.
- [14] *Multiphysics*, COMSOL, Inc., 1 New England Executive Park, Suite 350, Burlington, MA 01803. [Online]. Available: <http://www.comsol.com>
- [15] J. Roger, J. Pons, R. Massart, A. Halbreich, and J. Bacri, “Some Biomedical Applications of Ferrofluids,” *Eur. Phys. J. AP*, vol. 5, pp. 321–325, 1999.
- [16] A. Halbreich, J. Roger, J. Pons, D. Geldwerth, M. Da Silva, M. Roudier, and J. Bacri, “Biomedical Applications of Maghemite Ferrofluid.” *Biochimie*, vol. 80, no. 5-6, pp. 379–90, 1998.
- [17] D. Montgomery, *Solenoid Magnet Design*. Wiley-Interscience, 1969.
- [18] R. Merritt, C. Purcell, and G. Stroink, “Uniform Magnetic Field Produced by Three, Four, and Five Square Coils,” *Review of Scientific Instruments*, vol. 54, no. 7, pp. 879–882, 2006.
- [19] J. C. Aldred and I. Scollar, “Square Cross Section Coils for the Production of Uniform Magnetic Fields,” *Journal of Scientific Instruments*, vol. 44, no. 9, pp. 755–760, 1967. [Online]. Available: <http://stacks.iop.org/0950-7671/44/755>

- [20] M. W. Garrett and S. Pissanetzky, "Polygonal Coil Systems for Magnetic Fields with Homogeneity of the Fourth to the Eighth Order," *Review of Scientific Instruments*, vol. 42, no. 6, pp. 840–857, 1971. [Online]. Available: <http://link.aip.org/link/?RSI/42/840/1>
- [21] D. Ginsberg and M. Melchner, "Optimum Geometry of Saddle Shaped Coils for Generating a Uniform Magnetic Field," *Review of Scientific Instruments*, vol. 41, no. 1, pp. 122–123, 2003.
- [22] M. Jensen, J.H.; Abele, "Generation of Highly Uniform Magnetic Fields with Magnetized Wedges," *Transactions on Magnetics*, vol. 34, no. 4, pp. 2316–2323, 1998.
- [23] M. Zahn, *Electromagnetic Field Theory : a Problem Solving Approach*. New York: Wiley, 1979.
- [24] H. Saint-Jalmes, J. Taquin, and Y. Barjhoux, "Optimization of Homogeneous Electromagnetic Coil Systems: Application to Whole-body NMR Imaging Magnets," *Review of Scientific Instruments*, vol. 52, no. 10, pp. 1501–1508, 1981. [Online]. Available: <http://link.aip.org/link/?RSI/52/1501/1>
- [25] M. W. Garrett, "Calculation of Fields, Forces, and Mutual Inductances of Current Systems by Elliptic Integrals," *Journal of Applied Physics*, vol. 34, no. 9, pp. 2567–2573, 1963. [Online]. Available: <http://link.aip.org/link/?JAP/34/2567/1>
- [26] ———, "Axially Symmetric Systems for Generating and Measuring Magnetic Fields. Part I," *Journal of Applied Physics*, vol. 22, no. 9, pp. 1091–1107, 1951. [Online]. Available: <http://link.aip.org/link/?JAP/22/1091/1>
- [27] W. C. Elmore and M. W. Garrett, "Measurement of Two-Dimensional Fields. Part I: Theory," *Review of Scientific Instruments*, vol. 25, no. 5, pp. 480–485, 1954. [Online]. Available: <http://link.aip.org/link/?RSI/25/480/1>
- [28] J. Maxwell, *Treatise on Electricity and Magnetism*. New York: Dover Publications, 1954.

- [29] M. W. Garrett, “Table of Solenoids with Sixth-Order Error and Near-Maximum Power Efficiency,” *Journal of Applied Physics*, vol. 40, no. 8, pp. 3171–3179, 1969. [Online]. Available: <http://link.aip.org/link/?JAP/40/3171/1>
- [30] J. R. Barker, “New Coil Systems for the Production of Uniform Magnetic Fields,” *Journal of Scientific Instruments*, vol. 26, no. 8, pp. 273–275, 1949. [Online]. Available: <http://stacks.iop.org/0950-7671/26/273>
- [31] —, “The Magnetic Field Inside a Solenoid,” *British Journal of Applied Physics*, vol. 1, no. 3, pp. 65–67, 1950. [Online]. Available: <http://stacks.iop.org/0508-3443/1/65>
- [32] W. Braunbek, “Die Erzeugung Weitgehend Homogener Magnetfelder Durch Kreisströme,” *Zeitschrift für Physik*, vol. 88, pp. 399–402, 1934.
- [33] P. R. Robinson, “Improvements to the System of Four Equiradial Coils for Producing a Uniform Magnetic Field,” *Journal of Physics E: Scientific Instruments*, vol. 16, no. 1, pp. 39–42, 1983. [Online]. Available: <http://stacks.iop.org/0022-3735/16/39>
- [34] K. Kaminishi and S. Nawata, “Practical Method of Improving the Uniformity of Magnetic Fields Generated by Single and Double Helmholtz Coils,” *Review of Scientific Instruments*, vol. 52, no. 3, pp. 447–453, 1981. [Online]. Available: <http://link.aip.org/link/?RSI/52/447/1>
- [35] R. S. Caprari, “Optimal Current Loop Systems for Producing Uniform Magnetic Fields,” *Measurement Science and Technology*, vol. 6, no. 5, pp. 593–597, 1995. [Online]. Available: <http://stacks.iop.org/0957-0233/6/593>
- [36] M. W. Garrett, “Thick Cylindrical Coil Systems for Strong Magnetic Fields with Field or Gradient Homogeneities of the 6th to 20th Order,” *Journal of Applied Physics*, vol. 38, no. 6, pp. 2563–2586, 1967. [Online]. Available: <http://link.aip.org/link/?JAP/38/2563/1>
- [37] J. Jensen, “Minimum-volume Coil Arrangements for Generation of Uniform Magnetic Fields,” *Transactions on Magnetics*, vol. 38, no. 6, pp. 3579–3588, 2002.

- [38] L. B. Lugansky, "On Optimal Synthesis of Magnetic Fields," *Measurement Science and Technology*, vol. 1, no. 1, pp. 53–58, 1990. [Online]. Available: <http://stacks.iop.org/0957-0233/1/53>
- [39] —, "Optimal Coils for Producing Uniform Magnetic Fields," *Journal of Physics E: Scientific Instruments*, vol. 20, no. 7, p. 932, 1987. [Online]. Available: <http://stacks.iop.org/0022-3735/20/932>
- [40] —, "Optimal Coils for Producing Uniform Magnetic Fields," *Journal of Physics E: Scientific Instruments*, vol. 20, no. 3, pp. 277–285, 1987. [Online]. Available: <http://stacks.iop.org/0022-3735/20/277>
- [41] *Matlab*, The MathWorks, Inc., 3 Apple Hill Drive, Natick, MA 01760-2098. [Online]. Available: <http://www.mathworks.com>
- [42] *Rhinoceros*, McNeel North America, 3670 Woodland Park Ave North, Seattle, WA 98103. [Online]. Available: <http://www.rhino3d.com>
- [43] *An Introduction to the Hall Effect*, F.W. Bell Magnetics, A Sypris Test and Measurement Company, 6120 Hanging Moss Road, Orlando, Florida 32807. [Online]. Available: <http://www.sypris.com/library/documents/hallcatalog.pdf>
- [44] *MSG W11 Ferrofluid*, Ferrotec Corporation, 33 Constitution Drive Bedford, NH 03110. [Online]. Available: <http://www.ferrotec.com>
- [45] P. E. O. Ships, *DDG 1000*, U.S. Navy, 1333 Isaac Hull Avenue S.E., Washington Navy Yard, D.C. 20376. [Online]. Available: <http://peoships.crane.navy.mil/DDG1000/>
- [46] K. R. Foster, "Review of Carpenter and Ayrapetyan (Editors), Biological Effects of Electric and Magnetic Fields. Vol. 1: Sources and Mechanisms. Vol. 2: Beneficial and Harmful Effects," *Biophys. J.*, vol. 67, no. 5, pp. 2123–2124, 1994. [Online]. Available: <http://www.biophysj.org>
- [47] F. Barnes and B. Greenebaum, *Handbook of biological effects of electromagnetic fields*. CRC Press, 2007.

- [48] P. Stavroulakis, *Biological Effects of Electromagnetic Fields: mechanisms, modeling, biological effects, therapeutic effects, international standards, exposure criteria*. Springer, 2003.
- [49] I. Nair, M. Morgan, H. Florig, O. of Technology Assessment, U. States, and Congress, *Biological Effects of Power Frequency Electric and Magnetic Fields*. Congress of the US, Office of Technology Assessment: For sale by the Supt. of Docs., USGPO, 1989.
- [50] L. A. Sagan, *Electric and Magnetic Fields: Invisible Risk?* Taylor Francis (UK), 1996.
- [51] E. B. Association, “Queen Mary 2 Podded Propulsors,” internet. [Online]. Available: <http://www.electric-boat-association.org.uk/>
- [52] *Omax Make and Omax Layout*, Omax Corporation, 21409 72nd Ave South Kent, WA 98032. [Online]. Available: <http://www.omax.com>